THESIS FOR THE DEGREE OF DOCTOR OF PHILOSOPHY

Tailoring of Transition Metal Silicides as Protective Thin Films on Austenitic Stainless Steel

PUI LAM TAM

Department of Materials and Manufacturing Technology
CHALMERS UNIVERSITY OF TECHNOLOGY
Gothenburg, Sweden 2011

Tailoring of Transition Metal Silicides as Protective Thin Films on Austenitic Stainless Steel
PUI LAM TAM

ISBN 978-91-7385-560-0

Doktorsavhandlingar vid Chalmers tekniska högskola
Ny series nr 3241

ISSN 0346-718X

Department of Materials and Manufacturing Technology
Chalmers University of Technology
SE-412 96 Gothenburg
Sweden
Tel: +46 (0)31-772 1000
Fax: +46 (0)31-772 1310
www.chalmers.se

Printed by Chalmers Reproservice
Göteborg, Sweden 2011

Abstract

Transition metal silicide is an important material used in microelectronic devices and a possible candidate for high temperature application. The objective of this study is trying to make use of this material in a new way as protective thin films on engineering materials. The brittle nature of the silicides can thus be compensated by the ductile bulk material and the surface corrosion resistance can be improved. The choices of thin film constituents are targeted at the transition metal elements including titanium (Ti, Z = 22), chromium (Cr, Z = 24), iron (Fe, Z = 26) and nickel (Ni, Z = 28) in combination with silicon (Si, Z = 14) to form the binary-component intermetallic compounds by means of ion-beam sputter deposition, which was carried out in an ultrahigh vacuum (UHV) chamber at 10^{-6} Pa. The chosen substrate material is AISI 304 stainless steel. Thin film characterisations were conducted by means of surface analysing instruments: X-ray photoelectron spectrometer (XPS) and grazing incidence X-ray diffractometer (GIXRD). Silicide properties, including the degree of crystallinity, the formed phases, the electronic structures, the chemical compositions and the chemical states of each characterised element, were analysed. For the films in crystalline form, silicides were well characterised by both techniques. In case the crystalline phase did not develop and the phase(s) could not be analysed through XRD, the possible silicide phases in short-range order or no ordering can be estimated in accordance with the core-level XPS binding energy state of the transition metal peak defined by the crystalline form. On the other hand, the phase formation sequence of the silicides during annealing processes can be predicted by a theoretical method of Pretorius' effective heat of formation (EHF) model provided that the initial chemical concentrations were determined in advance. The corrosion properties of the silicide films and the uncoated stainless steel specimens were assessed and compared by means of potentiodynamic polarisation measurements in hydrochloric acid (HCl) and sulphuric acid (H_2SO_4), respectively. The polarisation curves of all the silicide-coated specimens show lower current densities along the measured potentials than the uncoated steel and thereby the silicides have lower reactivity. In the same test, it was found that binary-component silicides with Si content above 60 at.%, independent of the choice of transition metal element, facilitate the high integrity Si-oxide layer formation at the top of the tested specimens, and thereby a better corrosion resistivity is guaranteed. Among the four tested silicides, Ti-Si and Ni-Si films are found to be better candidates. In another study, corrosion tests were performed on the coated specimens that were thermally annealed after deposition with the purpose of promoting silicide phase development and film crystallisation. However, the polarisation results do not show significant benefit from this treatment. As a result, composition of the transition metal silicide thin films is a more important design factor compared to the film structure. When considering the silicides as protective thin films, their tribological properties such as adhesiveness and wear resistance cannot be neglected. The results from the Rockwell-C adhesion test and the reciprocal dry sliding wear test proved that the silicide films are well-adhered on the substrates and their wear properties are slightly better than the stainless steel by showing a lower specific wear rate from 10^{-12} $m^3/N{\cdot}m$ to 10^{-13} $m^3/N{\cdot}m$. It is believed that transition metal silicides, besides deposited on stainless steels, can also be the protective thin films on other engineering materials, as far as well-adhesiveness is guaranteed.

Keywords: Transition metal silicides; Thin films; Stainless steels; Ion-beam sputter deposition (IBSD); X-ray photoelectron spectroscopy (XPS); X-ray diffractrometry (XRD); Pretorius' effective heat of formation (EHF) model; Corrosion; Potentiodynamic polarisation measurements; Tribology; Rockwell-C adhesion test; Reciprocating sliding wear test

Preface

This thesis is submitted for the degree of Doctor of Philosophy at Chalmers University of Technology. The research described herein was mostly conducted in the Department of Materials and Manufacturing Technology under the supervision of Professor Lars Nyborg (Principal supervisor) and Dr. Mats Norell (Assistant supervisor) from April 2007 to September 2011. Dr. Yu Cao also took part in the work and contributed to the research. Part of the research was conducted in the Advanced Coatings Applied Research Laboratory (ACARL) directed by Dr. Lawrence Kwok Yan Li in the Department of Manufacturing Engineering and Engineering Management at the City University of Hong Kong.

The work reported in this thesis is original and to the best of the author's knowledge. This thesis has not been or is being submitted to any other university or institution for any other degree, diploma, certificate or professional qualification. Part of this work has been written into manuscripts, published in or submitted to the following journals:

Paper 1 **Sputter Deposition and XPS Analysis of Nickel Silicide Thin Films**
P. L. Tam and L. Nyborg
Surface and Coatings Technology 203 (2009) 2886 – 2890

Paper 2 **XRD and XPS Characterisation of Transition Metal Silicide Thin Films**
P.L. Tam, Y. Cao and L. Nyborg
Submitted to Surface Science, August 2011

Paper 3 **Corrosion Properties of Amorphous Ni-Si Thin Films on AISI 304L Stainless Steel**
P. L. Tam, U. Jelvestam and L. Nyborg
Materials at High Temperature 26 (2009) 177 – 184

Paper 4 **Corrosion Properties of Thermally Annealed and Co-sputtered Nickel Silicide Thin Films**
P.L. Tam, Y. Cao, U. Jelvestam and L. Nyborg
Accepted for publication in Surface and Coatings Technology, August 2011

Paper 5 **Corrosion Properties of Sputter-deposited Transition Metal Silicide Thin Films on Austenitic Stainless Steels in Dilute Sulphuric and Hydrochloric Acids**
P.L. Tam and L. Nyborg
Submitted to Materials and Corrosion, August 2011

Paper 6 **Tribological Behaviour of Sputter-deposited Nickel Silicide Thin Films on AISI 304 Stainless Steel**
P.L. Tam, P.W. Shum, K.C. Kian, K.Y. Li and L. Nyborg
Submitted to Wear, June 2011

Other publications not included in this thesis

1. **Substrate Bias Effects on Mechanical and Tribological Properties of Nanoscale Multilayer CrTiAlN Coatings Prepared by Closed Field Unbalanced Magnetron Sputtering Ion Plating Method**
   P.L. Tam, P.W. Shum, Z.F. Zhou and K.Y. Li
   Key Engineering Materials 334 – 335 (2007) 885 – 888

2. **Structural, Mechanical, and Tribological Studies of Cr-Ti-Al-N Coating with Different Chemical Compositions**
   P.L. Tam, P.W. Shum, Z.F. Zhou and K.Y. Li
   Thin Solid Films 516 (2008) 5725 – 5731

3. **Oxidation Resistance of Multicomponent CrTiAlN Hard Coatings at Elevated Temperatures**
   P.L. Tam, Z.F. Zhou, P.W. Shum and K.Y. Li
   Advanced Materials Research 75 (2009) 37 – 42

4. **High Temperature Oxidation of CrTiAlN Hard Coatings prepared by Unbalanced Magnetron Sputtering**
   Z.F. Zhou, P.L. Tam, P.W. Shum and K.Y. Li
   Thin Solid Films 517 (2009) 5243 – 5247

Acknowledgements

I would like to give my highest gratitude to *Professor Lars Nyborg* for giving me this opportunity to pursue my doctoral study under his supervision in the Department of Materials and Manufacturing Technology at Chalmers University of Technology. I have a high regard for his contagious enthusiasm at work and his all-round adroit capability on problem solving. Many inspiring discussions between us contribute a lot to the development of the present work. Of course, the research freedom he has given all these years is definitely showing his open-mindedness. Frankly, this work would hardly be accomplished without his unfailing support. And importantly, the financial support granted by the *Swedish Foundation for International Cooperation in Research and Higher Education (STINT, Stiftelsen för Internationalisering av Högre Utbildning och Forskning)* for the collaboration between Chalmers and the City University of Hong Kong in the first half of the research period (April 2007 – June 2009) is gratefully acknowledged.

Besides Professor Nyborg, my deepest indebtedness goes our experienced, efficient and modest research engineer (forskningsingenjör), *Mr. Urban Jelvestam,* for his kindliness, patience, persistent guidance and competent assistance all these years. Countless sharing and co-working experience are definitely invaluable.

I owe both *Dr. Emmy Yu Cao* and *Dr. Sergio Alfonso Pérez-García* a debt of gratitude too for inspiring me to pick silicide materials as my research focus. Many predecessors in our former Department of Engineering Metals including *Prof. Ingemar Olefjord, Dr. Bengt-Olof Elfström, Prof. Bill Brox, Dr. Håkan Mattsson, Dr. Lena Wegrelius, Prof. Dan-Qing Yi* and *Dr. Fredrik Falkenberg* are deeply respected for their contribution relating to the metal silicides and the corrosion research on engineering materials in the past decades. All of your well-organised theses develop solid foundations in these two subjects and shed me a light in this work.

Here I would like to say thank you to my former colleagues, *Dr. Sam Po Wan Shum* and *Mr. Kwok Cheung Kian* in the *Advanced Coatings Applied Research Laboratory (ACARL)* for assisting me to accomplish the tribological experiments. I may also express my high esteem to many respected professors, doctors, lecturers, research staff, as well as technicians, friends and students I have met in my university life both in Sweden and Hong Kong. To name a few, *Dr. Lawrence Kwok Yan Li, Dr. Zhi Feng Zhou, Prof. Joseph Kei Luek Lai, Dr. Wilson Kam Wa Wong, Dr. Yao-Gen Shen, Dr. Zheng Kui Xu, Prof. Wing Yim Tam, Prof. Tong-Yi Zhang, Dr. Peter Sotkovszki, Mr. Göran Fritz, Prof. Vratislav Langer, Prof. Lars-Gunnar Johansson, Prof. Jan-Erik Svensson, Prof. Elisabet Ahlberg, Dr. Zareen Abbas*, *Dr. Mats Norell* and *the students in the M2 classes (2009, 2010)* thanks for evolving my interest, broadening my vision, and deepening my knowledge in the field of materials science and engineering.

Last, but far from least, my very sincere thanks go to my family for their patience, unconditional love and support all the time. My beloved girlfriend, *Emily*, thanks for bringing in the artistic elements into my writing. This thesis cannot be finished without your contribution!

Eric Pui Lam Tam (談沛霖)

July 2011

Gothenburg, Sweden.

Abbreviations, Symbols and Constants

AFM	Atomic force microscope
ARXPS	Angle-resolved X-ray photoelectron spectroscopy
BE	Binding energy
FWHM	Full-width at half maximum
GIXRD	Grazing / Glancing incidence X-ray diffraction
IBSD	Ion-beam sputter deposition
PVD	Physical vapour deposition
SEM	Scanning electron microscope / microscopy
SHE	Standard hydrogen electrode
TEM	Transmission electron microscope / microscopy
UHV	Ultrahigh vacuum
XPS	X-ray photoelectron spectrometer / spectroscopy
XRD	X-ray diffractometer / diffraction

ΔH^o	Standard heat of formation	($kJ \cdot mol^{-1} \cdot at.^{-1}$)
$\Delta H'$	Effective heat of formation	($kJ \cdot mol^{-1} \cdot at.^{-1}$)
E	Electrochemical potential	(mV)
E^o	Standard potential	(V)
E_{corr}	Corrosion potential	(mV)
E_{pass}	Passivation potential	(mV)
E_{pit}	Pitting potential	(mV)
E_{trans}	Transpassive potential	(mV)
E^*	Effective elastic modulus	(GPa)
E_{IT}	Indentation modulus	(GPa)
E_r	Reduced modulus	(GPa)
E_{sam}	Specimen modulus	(GPa)
E_{film}	Thin film modulus	(GPa)
E_{sub}	Substrate modulus	(GPa)
H	Indentation hardness	(GPa)
H_{film}	Thin film / Top layer hardness	(GPa)
H_{sub}	Substrate hardness	(GPa)
HF	Adhesion strength level	
i	Current density	($\mu A/cm^2$)
μ_f	Friction coefficient	
R_a	Arithmetic roughness	(nm)
R_q	Root means square roughness	(nm)

F	Faraday's constant	= 96485	$C \cdot mol^{-1}$
k	Boltzmann's constant	= 1.38×10^{-23}	$J \cdot K^{-1}$
N	Avogadro's number	= 6.02×10^{23}	mol^{-1}
R	Universal molar gas constant	= 8.314	$J \cdot mol^{-1} \cdot K^{-1}$

Table of Contents

Chapter 1 Research Background and Scope of Thesis

Longer servicing life of engineering systems is always desired in all engineering design. The key factor of the long lifetime largely depends on the correct usage of the engineering materials. Since the working environment in practice varies a lot and no material can perfectly fit for all conditions, research on materials reengineering and advanced materials development is, in fact, never ended. Somehow, in order to keep the usefulness of some widely-used engineering materials under some specific environment, an alternative way is to modify their surface properties through surface engineering processing such as thin film/coating development, ion/plasma implantation, heat treatment and cold working. A modified and improved surface means not only better materials functionality, but also a lower operating cost, less material waste and fewer recycling processes in long run. The importance of this work is indisputable in views of engineering, economics, energy, and environment concerns. Therefore, in this thesis, research focus on surface properties reengineering of chloride-susceptible austenitic stainless steel through thin film deposition of some transition metal silicides is proposed and conducted. The main objective is to improve the corrosion resistance of this material, especially in an acidic and chloride-containing environment, and to find out other potential benefits gain from the developed and studied surface engineering process.

The development of the research is as follow: the work was commenced with the thin film fabrication of various binary-component transition metal silicide including Ti-Si, Cr-Si, Fe-Si and Ni-Si by using sputter-deposition technique. The surface chemical and structural characterisations of the thin films were conducted by means of X-ray photoelectron spectroscopy (XPS) and X-ray diffractometry (XRD). The resulting silicide phases in the individual specimens are then further considered and predicted using a theoretical approach by means of Pretorius' effective heat of formation (EHF) model (Papers 1 and 2). In order to evaluate and compare the corrosion properties of different silicide thin films, electrochemical potentiodynamic polarisation measurements were carried out in hydrochloric acid and sulphuric acid, respectively. The results show that some of these films can slightly improve the corrosion resistance of AISI 304 stainless steel by driving the corrosion potential (E_{corr}, unit: mV) towards a nobler state and reducing the current density (i, unit: $\mu A/cm^2$) throughout the measured potential range (Papers 3 to 5). Concurrently, the results show that better corrosion resistance can be achieved by increasing silicon content in the binary-component system (Paper 3) and by choosing $TiSi_2$ as the protective thin films (Paper 5). Meanwhile, the impact of the thin film structural design (i.e. degree of crystallinity) is not significant (Paper 4). As the thin film adhesiveness is always the primarily concern in engineering practice, the tribological behaviour of one of the silicide systems, i.e. Ni-Si, was investigated. The results show that the sputter-deposited thin films, independent to the degree of crystallinity, adhere well on the stainless steel substrate. The corresponding wear test also shows that the silicide-coated stainless steel has slightly lower wear rate than the uncoated specimen (Paper 6). Overall, the depositions of binary-component transition metal silicide thin films on the stainless steel surfaces give considerable beneficial effects on corrosion and wear resistance enhancement.

In the appendices, technical background about each testing instrument and the individual characterisation method are introduced in individual subsection. Fundamental theories behind each technique are also briefly covered.

To improve the corrosion resistance of an engineering material through coating deposition, what tasks should be done to tailor and to test the usability of a novel recipe?

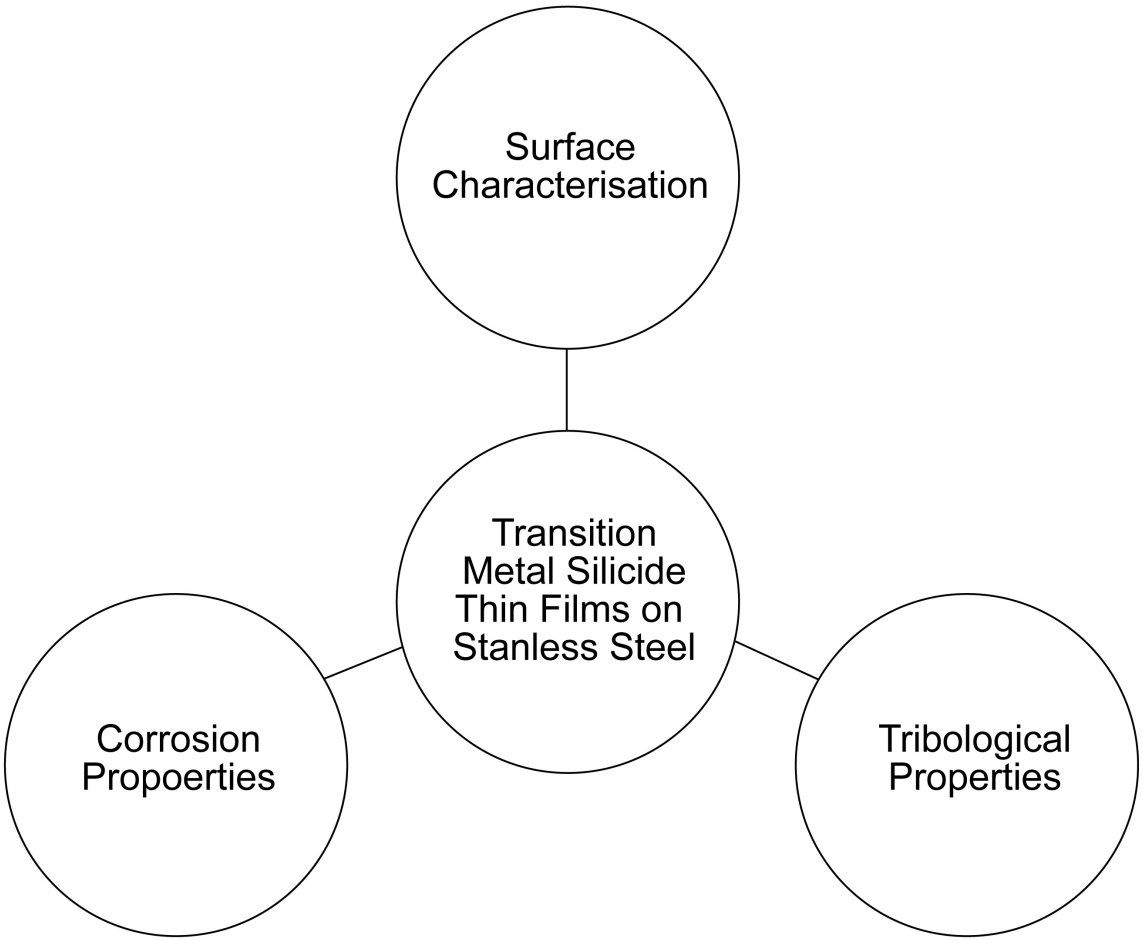

** The major research activities including thin-film fabrication (Author), surface characterisation (Cao, Nyborg and author) and corrosion properties investigation (Nyborg and author) were conducted at Chalmers University of Technology; the tribological experiments (Shum, Kian and Li) were run at the City University of Hong Kong and the data analyses were carried out by the thesis author.*

Figure 1 Scope of thesis.

Chapter 2 Surface Protection against Corrosive Environment

2.1 Corrosion Issues – Stainless Steels

Stainless steel is nowadays an omnipresent engineering material in domestic applications and industry after a century long development. The properties of stainless steel can be easily manipulated through alloying and/or different heat treatment processes. For its vast amount of different applicable areas, commercialised stainless steels are nowadays classified into six grades to fit into different purposes. They include ferritic stainless steels (α), austenitic stainless steels (γ), martensitic stainless steels (ε), duplex stainless steels (α + γ), precipitation hardening stainless steels and Mn-N substituted austenitic stainless steels [1]. Among all grades, they share one common characteristic, i.e. a chemically stable passive layer forms and adheres on their surfaces when they are exposed to the atmosphere. For this reason, this behaviour makes stainless steels "stainless" in the ambient condition as well as other kinds of environment [1-6].

The passive layer plays an important role in enhancing the corrosion resistance of stainless steel. It acts as a physical barrier to isolate the alloyed material from the chemical species (maybe corrosive) in the atmosphere. Consequently, the interaction between the corrosive species and the underlying bulk metallic species is minimised, and the steel deteriorating reactions (i.e. metallic corrosion) unlikely occur. The nature of passive layer is environmentally dependent. For instance, at room temperature, compositions of the passive layers on austenitic stainless steel depend on the relative humidity (R.H.) in the surrounding as for example addressed by Olefjord et al. [7-11] (Fig. 2). In a dry environment, the passive layer is analysed to be iron oxide; in a wet environment developed by clean water vapour, chromium oxide is preferentially formed [11]. In a high temperature environment, the different possible oxides formed on the stainless steel surfaces are summarised in Table 1 [11-16]. In fact, the composition of the oxide film is also related to the alloy composition. Basically, stainless steel is an iron-based alloy that contains at least 12 wt.% chromium. In an environment at a certain R.H. level, the most abundant constituents, like Cr and Fe, can readily react with water vapour (H_2O) and oxygen (O_2) to form the above-mentioned oxides. It is known that a chromium-rich oxide of Cr_2O_3 type is preferable for a better corrosion resistivity [3,11]. This oxide readily creates a coherent, adherent and regenerating thin protective film on the surface with a uniform thickness of around 20 Å [8]. This layer resists the chemical attacks from nitric acid (HNO_3), phosphoric acid (H_3PO_4), and/or acetic acid (CH_3COOH) and is practically impermeable to materials diffusion [6, 17]. Still, the oxide of this type does not resist the attack from concentrated hydrochloric acid (HCl), sulphuric acid (H_2SO_4), formic acid (HCOOH) and/or poor circulation conditions with the presence of halides, e.g. fluoride (F^-), chloride (Cl^-), bromide (Br^-) and iodide (I^-) [17].

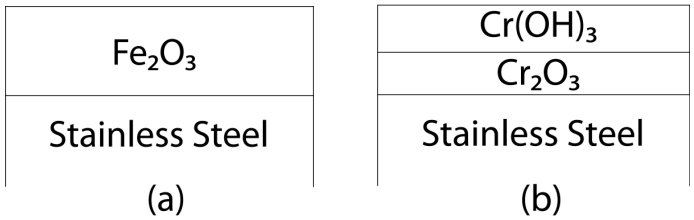

Figure 2 The possible passive layer formed on the stainless steels under (a) dry condition and (b) wet condition at room temperature (Drawing based on [11]).

Table 1 Properties of possible oxides formed in stainless steels at room and high temperature [12,14]

Nomenclature	Chemical compound	Nature
Maghemite	γ-Fe_2O_3	● Formed in low-temperature oxidation ● Spinel ferrite structure as in magnetite ● Transform to α-Fe_2O_3 at high temperature
Wüstite	$Fe_{1-x}O$	● Formed above 570 ˚C ● Non-stoichiometric rock salt structure ● Cation deficiency oxide: p-type ● Fast ion diffusion rate ● Non-protective oxide
Magnetite	Fe_3O_4 $[Fe^{3+}]_{tet}[Fe^{2+},Fe^{3+}]_{oct}O_4$	● Formed between 570 ˚C and 650 ˚C ● Inverse spinel oxide structure ● Cation deficiency oxide: p-type ● More protective than wüstite but less protective than hematite
Hematite	α-Fe_2O_3	● Corundum structure ● Hexagonally close-packed oxide structure ● 650 ˚C – 800 ˚C: Oxygen deficiency oxide: n-type ● >800 ˚C: Cation deficiency oxide: p-type ● The most protective iron oxide
Eskolaite / Chromia	Cr_2O_3	● Cation deficiency oxide: p-type ● Slow ion diffusion rate ● One of the best protective oxides
Spinal type solid solution	M_3O_4 (e.g. Cr_2MnO_4)	● Fe^{2+} can be replaced by some divalent cation like Ni^{2+} ● Fe^{3+} can be replaced by some trivalent cations like Cr^{3+}
Corundum type solid solution	$(M_A,M_B)_2O_3$ (e.g. $(Cr_xFe_{1-x})_2O_3$)	● x = 0.75 – 1.0: p-type ● x = 0: p-type ● x = 0.25 – 0.75: both n- and p-type

When a piece of stainless steel is placed in an aggressive environment as mentioned above (e.g. an acidic halide-containing solution) after a period of time, this piece of alloy will be chemically attacked and the most prominent features appeared would be pits formation. Although there are many studies and discussion about pitting corrosion, controversies still exist. Generally, the initiation of pits correlates to the type and concentration of the aggressive species as well as the non-uniformity of passive film on the stainless steel surface near the inclusions and the structural defects [1]. One model that correlates to sulphide inclusions is illustrated in Figure 3 [18]. In this model, corrosion commences in and around the inclusions where the passive layer thickness is relatively thinner than the bulk. A direct contact between alloy and the corrosive species establishes easier and leads to violent corrosive attack on the metallic materials afterwards. As the corrosion rate is halide-concentration dependent and varies among different locations, localised pitting corrosion proceeds randomly on the stainless steel surface [7-18]. More about the pitting corrosion mechanisms will be discussed in Section 3.5.

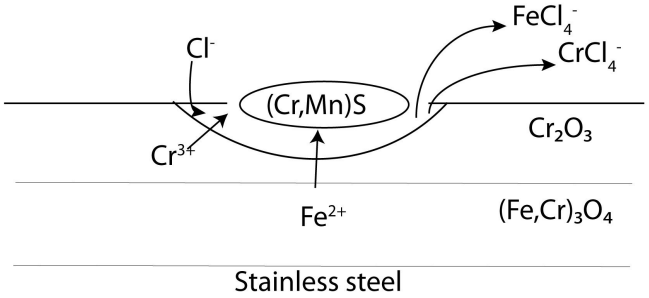

Figure 3 Illustration of the pitting corrosion mechanism on stainless steels (Drawing based on [18]).

Besides the contribution from passive layer, corrosion resistivity of stainless steels can be improved by varying the concentration of the alloying elements such as carbon (C), nitrogen (N), phosphorus (P), molybdenum (Mo), silicon (Si), titanium (Ti), and/or niobium (Nb) as well. Different classes of stainless steels with different levels of corrosion resistivity are thus developed [3]. However, metallurgists have found the formation of certain corrosion resisting phases through heat treatment will reduce the overall corrosion resistance of stainless steels by taking away the corrosion-resisting species from the bulk (Table 2) [1,19]. Therefore, to enhance the corrosion resistance of stainless steel materials by those corrosion resisting phases, other approaches in surface engineering treatments such as coating deposition and ion implantation can be attempted to achieve the same purpose.

Table 2 Common phases in stainless steels [1,19]

Phase	Suggested element/ compound	Crystallographic data	
		Space group	Lattice parameter
Matrix phases			
α	Fe-base	$Im\bar{3}m$ (229)	a = 2.8664
γ	Fe-base	$Fm\bar{3}m$ (225)	a = 3.6000
Intermetallic phases			
Fe-rich			
J	α'-Cr + α-Fe	$Im\bar{3}m$ (229)	a = 2.8600
σ*	(Fe,Cr)	$P4_2/mmm$ (136)	a = 8.7995, c = 4.5442; (c/a = 0.516)
L	(Fe,Ni)	P4/mmm (123)	a = 3.5200, c = 3.6300; (c/a = 1.03)
Laves	Fe_2X (X = Mo, Ti, Nb)	$P6_3/mmc$ (194)	a = 4.7440, c = 7.7250; (c/a = 1.628)
Ni-rich			
η	Ni_3Ti	$P6_3/mmc$ (194)	a = 5.0930, c = 8.2760; (c/a = 1.625)
Mo-rich			
χ*	$Cr_6Fe_{18}Mo_5$ $(Fe,Ni)_{36}Cr_{18}Mo_4$	$I\bar{4}3m$ (217)	a = 8.8037
μ	Fe_7Mo_6	$R\bar{3}m$ (166)	a = 4.7540, c = 25.7100; (c/a = 5.408)
R	Fe-Cr-Mo	$R\bar{3}$ (148)	a = 10.9109, c = 19.3540; (c/a = 1.774)
R'		$m\bar{3}\bar{5}$	Icosohaedral quasicrystal
Si-rich			
G*	$Cr_{12}Ni_9Fe_2Si_6$	$Fm\bar{3}m$ (225) $Fd\bar{3}m$ (227)	a = 11.1980 a = 11.1000
Fe-Si	Fe_3Si, Fe_2Si	$Fm\bar{3}m$ (225)	a = 5.6533
Cr-Si	Cr_3Si	$Pm\bar{3}n$ (223)	a = 4.5550
SiC*	SiC	$F\bar{4}3m$ (217) (β) $P6_3mc$ (186) (α, 4H)	a = 4.3589 a = 3.0810, c = 10.061; (c/a = 1.774)
Oxides			
SiO_2		Amorphous	
α-Al_2O_3	Al_2O_3	$R\bar{3}c$ (167)	a = 4.7488, c = 12.9929; (c/a = 2.736)
κ-Al_2O_3	Al_2O_3	$Pna2_1$(33)	a = 4.834, b = 8.310, c = 8.937
α-Cr_2O_3	Cr_2O_3	$R\bar{3}c$ (167)	a = 4.958766, c = 13.5942; (c/a = 2.741)
M_3O_4	$Mn_{1.5}Cr_{1.5}O_4$	$Fd\bar{3}m$ (227)	a = 8.455

* *Examples of corrosion-resisting phases which have negative effect on the passivity of stainless steel [1].*

2.2 Protective Coatings

A coating is an artificially synthesized layer covering the top of a bulk material (substrate) with thickness more than one micron. The concept of a coating to enhance the surface properties and/or improve the aesthetic appearance of a material was officially recognised in the 1950s [20-22]. Coatings can be classified in terms of their compositions and their functions. From composition point of view, they can be made of metals, organic compounds, cement mortars or enamels; from functional point of view, the aim of adding a coating can be made for decorative, protective, decorative-protective or technical purpose [4,17,20,23].

Generally, protective coatings reduce the corrosion rate of the protected materials by acting as the physical barriers to minimise the direct interaction between the corrosive species and the susceptible metallic materials. The average thickness of the protective coatings is usually several microns and thicker coating is actually preferred to minimize the invincible coating defects that are independent of which deposition technique that has been utilised [21,22]. To guarantee coating performance, good coating adhesiveness, high mechanical resistance, low internal stress, high chemical stability and low permeability for the corrosive components are the important properties needed in coatings applications [20-23]. It is recognised that coating performance also depends largely on the microstructure of the coating and this can be tailored by optimising the constituents and fabrication parameters [24-29]. In addition, to make the coating applicable to the coating-substrate couple, the chosen coating material should have similar thermal expansion coefficient (CTE) as the substrate material in order to avoid cracking or lattice mismatch at the coating-substrate interface.

The development of nanotechnology starting from the beginning of the millennium has made microstructure studies one of the hottest topics in the past decade. Remarkable achievements in nanocomposite coatings, superlattice coatings, and nanoscale multilayer coatings bring advanced coatings into industrial applications [24-29]. In the area of protective coatings, a new approach about smart self-repairing protective coatings is currently discussed. Besides acting as a physical barrier, this class of coatings also encapsulate corrosion inhibitor in amorphous solid solution, which can migrate out to a chemically reactive zone to reduce the metal corrosion rate initiated by bacteria or corrosive species [30-32]. In such case, the practicability of these coatings can be everlasting. However, this advance achievement is out of the scope of this work, but it could be kept as a proposal for future work.

Development of protective coatings for stainless steels comprises advanced, important and active research activities in the coatings, corrosion science and corrosion engineering fields: hafnia-alumina coatings [33], various conductive polymers [34-37] and high purity stainless steels thin films [38] are reported recently to be reliable candidates. Nevertheless, silicon and its compounds such as the silicides, being among the most corrosion-resistant elements and compounds at both ambient and high temperature condition [39-46], are rarely discussed in this particular context and will be highlighted this time.

2.3 Potential Use of Transition Metal Silicides as Protective Thin Films

Silicon was extracted as a pure metalloid element by the Swedish chemist, Jöns Jacob Berzelius in 1824 and the element is found to be one of the most abundant solid elements in nature [47,48]. The general properties of silicon include low density, high hardness, high brittleness, high melting temperature and chemical inertness. Because of the brittle nature of silicon, it was found difficult to seek a practical application of silicon in engineering industries after the discovery. Fortunately, due to the unique semiconducting properties achieved by doping, silicon and silicon-typed materials are now well developed and widely applied in microelectronic industry. Materials of this type can be found in transistors, photovoltaic cells, rectifiers, integrated circuits, optoelectronic devices, and many other modern electronic devices in either bulk or thin layer (i.e. in micron- or nano-scale) form [48]. However, the modern development of silicon is now reaching the physical limits and the silicon's reign might be nearing to its end in microelectronics [49,50].

In order to bring silicon into the mechanical and manufacturing industries, it is necessary to improve the ductility and toughness of the materials based on silicon. One way to achieve this objective is to develop the intermetallic compounds, the silicides; that is, mixing silicon with one or more metallic elements in the manufacturing process. The idea behind is to introduce more non-directional character ductile metallic bonds into the otherwise brittle covalent-dominating structure (i.e. Si), and thus the ductility of the compound gets improved [51-53]. Although the literature reports that the high temperature mechanical performance of silicides does improve compared to that of silicon [52-55], the room temperature brittleness and high cost for the manufacturing process still remain the major barriers to bring the silicides into wide general application. Nevertheless, the highly stable performance of silicides under high temperature and adverse environment catches the attention of aero-engineers, automotive-engineers and metallurgists, as those properties are what the engineers need for the engine components and furnace walls [45,54,55]. A classic example is the use of MoSi for heating elements [40]. Generally, the attractive properties of intermetallic silicides include superb strength at high temperature, high oxidation resistance, high corrosion resistance and relatively low density. Aqueous corrosion resistance of silicide materials is good as well, but the discussion about this is rarely mentioned until recent years [45,46]. More about this issue will be described in this section. First of all, some of the physical properties about the selected binary-component transition metal silicides related to this study are summarised in Table 3. It is found that silicidation of transition metal is the exothermic process, materials density reduces and the corresponding melting point decreases as a result.

Table 3 General properties of the selected transition metal and their corresponding silicides [48,52,56-58]

Composition	Structure (Pearson)	Space Group	Lattice Parameters	No. of atoms per unit cell	No. of metal atoms per unit cell	Density ($g \cdot cm^{-3}$)	Melting Point (ºC)
Si	A4	$Fd\bar{3}m$	a=5.431	8	8	2.33	1410
Ti	A3	$P6_3/mmc$	a=2.951; c=4.683	2	2	4.51	1660
α-$TiSi_2$	C54	Fddd	a=8.236, b=4.773, c=8.523	24	8	4.13	1500
Cr	C2	$Im\bar{3}m$	a=2.884	2	2	7.20	1857
$CrSi_2$	C40	$P6_222$	a=4.428, c=6.369	9	3	4.98	1490
Fe	A2	$Im\bar{3}m$	a=2.866	2	2	7.88	1535
β-$FeSi_2$	C49	Cmca	a=9.879, b=7.799, c=7.839	3	1	4.95	Transform to α-$FeSi_2$ at 700 and melt at 1220
Ni	A1	$Fm\bar{3}m$	a=3.524	4	4	8.91	1455
$NiSi_2$	C1	$Fm\bar{3}m$	a=5.416	12	4	4.80	993

Corrosion Resistivity of Transition Metal Silicides

Chemical inertness of silicon in the ambient environment correlates to the silica (SiO_2) formation at the uppermost surface when in contact with oxygen and/or water molecules. Naturally, owing to the high oxygen affinity of silicon, silica layer forms readily into metastable vitreous structure (i.e. non-crystalline or short-range order) well-adhered on the Si substrate. This vitreous oxide layer has low density of defects ($< 10^{16}$ cm^{-3}) and inhibits the inward transport of oxygen ions (O^{2-}) to the silicon-oxide interface; thereby, the oxidation rate and the oxide layer growth rate reduces as a function of time [59,60]. This layer can transform to crystalline form at high temperature (Table 4) and is still a well-protective layer to the underlying structure up to 1500 ºC. Beyond that temperature, gas molecules (e.g. H_2O and O_2) adsorb on the surface, diffuse through the structure, react with the silica to form gaseous silicon monoxide [$SiO_{(g)}$] and leads to vitreous network breakdown. From aqueous chemistry point of view, although this layer is reported to be chemically inert in most of the acids at room temperature, the layer, in fact, suffers corrosion attack from hydrofluoric acid (HF) and alkaline solution, e.g. NaOH [48]. Moreover, both reactions can be accelerated in the presence of halide ions, such as fluoride (F^-) and chloride (Cl^-) [61-65].

Table 4 Some physical properties of bulk silica [48]

Type of silica	Crystal Structure and Morphology	Density ($g \cdot cm^{-3}$)	Temperature (ºC)
α-SiO_2 (α-Quartz)	Hexagonal crystal, colourless	2.648	Room temp. to 573
β-SiO_2 (β-Quartz)		2.533	573 to 867
SiO_2 (tridynite)		2.265	867 to 1470
SiO_2 (cristobalite)		2.334	1470 to 1722 (m.p.)
SiO_2 (vitreous)	Vitreous solid, colourless	2.196	1722 to 2950 (b.p.)

In transition metal silicides, besides silicon, the transition metal can also get oxidised in contact with water and oxygen. Therefore, it is possible for these binary-component systems to develop oxide layers consist of two or more constituents. The possible oxides formed from different transition metals

are listed in Table 5. It is noted that, metal oxides are classified into 3 classes: network-formers, intermediate ones and network modifiers. Metal oxides fall into the network-forming or intermediate classes and tend to grow as protective oxides that support anion or mixed anion-cation movement. The network formers are non-crystalline and the intermediates tend to be microcrystalline at low temperatures. For the network modifiers, they are polycrystalline structure and the developed layers are thicker and less protective. The bonding in a network forming oxide is covalent and that in a modifying oxide is ionic. The grain boundaries that exist between the crystallites facilitate the ion mobility across the layer and thus promote the chance of metal-corrosive species reactions. As a result, a single phase of network former is actually preferred for better protectiveness [59,66].

Table 5 Type of possible oxide films [58,65-68]

M in MO_x	Valence	Formed Oxide	Bond strength ($kJ \cdot mol^{-1}$)	Coordination number (C.N.)	Nature of the formed oxide*	Protectiveness
Si	4	SiO_2	444	4	Network Former	Protective
Ti	4	TiO_2	306	6	Intermediate	Protective
Cr	3	Cr_2O_3	197	6	Network Modifier	Protective
Fe	2	FeO	134	6	Network Modifier	Non-Protective
Fe	3	Fe_2O_3	407	6	Network Former	Protective
Ni	2	NiO	117	6	Network Modifier	Non-Protective

**Network former if the bond strength is stronger than 315 $kJ \cdot mol^{-1}$; oxide becomes network modifier if the bond strength is weaker than 210 $kJ \cdot mol^{-1}$; intermediate oxides have the bond strength between 210 and 315 $kJ \cdot mol^{-1}$ [59].*

Effectiveness of Oxide in the Chosen Chemical Environment

The oxidation state of individual element in a specific chemical environment can be predicted according to the thermodynamic potential-pH diagram (Pourbaix diagram), see Figure 4 and 5 [69,70]. In our tested environments of 0.50 M sulphuric acid (H_2SO_4) (pH = 0) and 0.05 M hydrochloric acid (HCl) (pH = 1.3), it can be predicted that SiO_2 is formed and keeps stable even at a high potential. The transition metal counterparts, except Ti, dissolve gradually into their ionic states in a wide potential range and cannot form any protective oxide. Therefore, it is predicted that Ti-silicides could be a potential candidate to withstand the testing conditions.

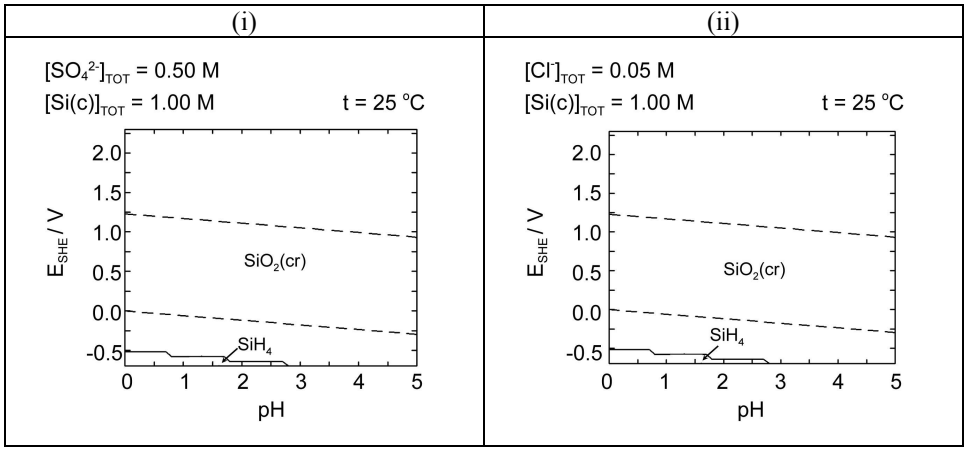

Figure 4 The Pourbaix diagram of Si in (i) 0.50 M H_2SO_4 and (ii) 0.05 M HCl and the silicon concentration is assumed to be 1.00 M (Simulation in [70]).

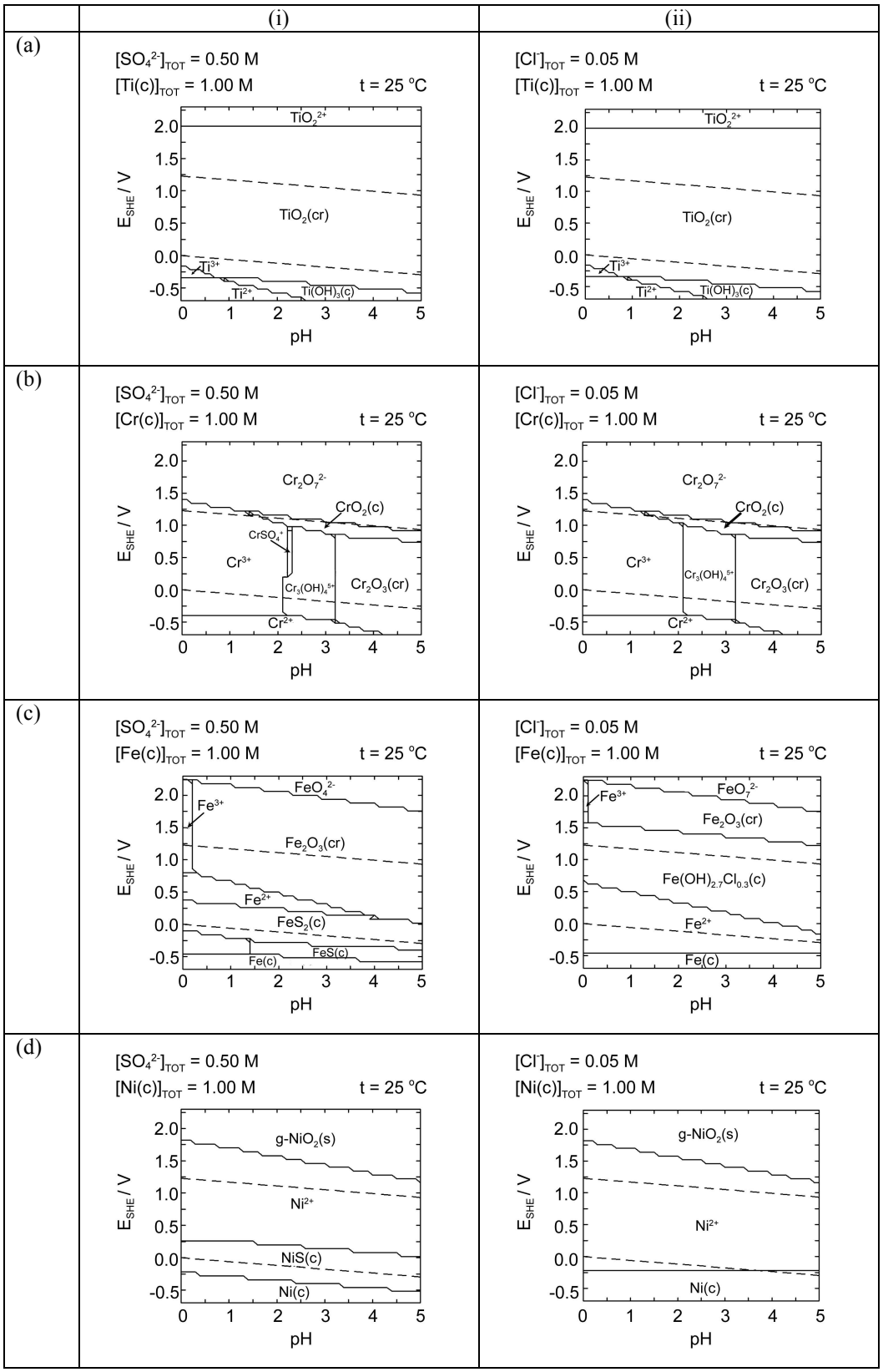

Figure 5 The Pourbaix diagrams of (a) Ti, (b) Cr, (c) Fe and (d) Ni in (i) 0.50 M H_2SO_4 and (ii) 0.05 M HCl and all transition metals concentration are assumed to be 1.00 M (Simulation in [70]).

Corrosion of Transition Metal Silicides

Comprehensive studies of the anodic behaviour of powder compacted transition metal silicide electrode materials of Mn-Si, Fe-Si, Co-Si and Ni-Si have been conducted by Shein et al. in acid, alkaline and halide-containing solutions [61-65, 71-77]. The results from their acid tests are summarised in Table 6. By checking the electrochemical parameters in the polarisation curves, it was found that silicides materials have superior corrosion resistivity in comparison to their transition metal counterpart by showing lower current density (i.e. lower reaction rate) at corrosion potential (E_{corr}), passivation potential (E_{pass}) and wider passivating range (E_{range}). The general conclusion for the acid tests of H_2SO_4 for all transition metal silicides was that, "the selective dissolution of transition metal takes place concurrently with the oxidation of Si to SiO_2 [71-73]." The dissolution rate is determined by i_{active}. This process was supposed to be connected to the diffusion of transition metal in the intermetallic compound and the transport of the oxidised transition metal in the superficial layer of the hydrated SiO_2 [71-73]. Therefore, it is expected that structure with stronger intermetallic bonds (e.g. covalent bond implies lower dissolution rate and lower diffusion rate) and higher Si content is preferable to enhance corrosion resistance [71,72]. Nevertheless, in the presence of halides such as fluoride (F^-) or chloride (Cl^-), the anodic process as such was found to accelerate, in addition with the dissolution of a surface layer of SiO_2 and Si [61-65-73]. These results from the bulk materials are important references for the thin film silicides study.

Table 6 Anodic potentiodynamic polarisation measurements of some powder-compacted electrodes [71-73]

Type of silicide materials	Si	Mn	Fe	Co	Ni	MnSi	FeSi	CoSi	NiSi
Testing condition	0.50 M H_2SO_4, Scan rate = 1 mV/s, Reference electrode is Standard hydrogen electrode (SHE)								
Electrochemical parameters									
E_{corr} (mV)	-80	-680	-160	75	75	-70	0	155	-173
i_{corr} ($\mu A/cm^2$)	5.5	3500	200	10^3	200	0.15	0.20	0.10	10
E_{pass} (mV)	200	-500	580	1460	460	100	155	405	0
i_{crit} ($\mu A/cm^2$)	10^3	10^5	10^5	10^5	10^5	1	0.1	0.5	10^3
i_{pass} ($\mu A/cm^2$)	10^3	10^5	10^2	10^3	10	1	0.1	0.3	4.5
E_{trans} (mV)			1590	1650	1330	1260	1560	1420	1190
E_{range} (mV)*			1010	190	870	1160	1405	1015	1190

*$E_{range} = E_{trans} - E_{pass}$

Other currently active silicide corrosion researches are found in the groups in China, Norway and Russia [78-82]. Wang et al [80-82] developed some multi-phases transition metal silicides specimens by means of laser cladding techniques. Their electrochemical corrosion tests in H_2SO_4, NaOH and NaCl solutions were carried out in a similar approach as Shein did for the Ni-Ti-Si and Cr-Ni-Si systems. These silicides showed good corrosion resistance in all the tested conditions and the discussion about corrosion mechanisms are basically the same as by Shein and co-workers.

Clearly, bulk silicide materials can be claimed to have good corrosion resistance, but brittle in nature, and the idea of using silicide as protective coatings was proposed already in 1991 by Knyazheva et al. [46]. However, since then not many papers are found related to in this specific subject [83-90]. Even so, the reliability of silicide coatings is substrate dependent and no systematic study has been conducted so far. With this basis, the studies of the corrosion properties of transition metal silicide materials, applied as submicron protective thin films on one of the most widely-used engineering materials – austenitic stainless steel, comprise the major objectives of the present thesis work.

Chapter 3 Electrochemical Approach to Assess Corrosion Properties of Materials

Corrosion is one of the most common and costly material failure mechanisms. The latest published survey in 2007 [91] shows that the direct cost of corrosion – essentially materials, equipment, and services involved in repair, maintenance, and replacement, is between € 1.3 and 1.4 trillion in the world, or 3.1 to 3.5 % of a nation's annual gross domestic product (GDP). Unfortunately, corrosion is unavoidable and atmospheric corrosion happens every instant once an object is exposed to the air. Although the corrosion rate can be slowed down through proper material designs and surface engineering processes, it does not mean that the corrosion process can be completely prohibited. On the other hand, every corrosion case is unique and there is no single solution or advanced material that can solve all the problems. Corrosion can be affected by many chemical species. They can be in gaseous form such as nitrogen oxides (NO_x), sulphur dioxide (SO_2), hydrogen chloride (HCl), solid form such as particulates/suspension like dust, aqueous form involving compounds such as sodium chloride (NaCl) and fluoride (F^-) [92], or even microbiological form such as bacteria [93]. Clearly, the different corrosion reactions that occur as a result of the corrosive species cause detrimental effects to engineering materials. Fortunately, engineering materials are not just suffering from the chemical reactions induced by the environment. With the appropriate alloy design, materials can, in response to the environment, react and heal themselves by developing a protective layer. This layer helps to reduce the surface reactivity, reduce the ion species mobility, and/or develops as a physical barrier between the material and external environment. By this means, the risk of corrosion attack can be minimised.

To assess the corrosion properties, more than hundreds of testing methods are found in the corrosion testing handbook [94]. Meanwhile, in this work, only an electrochemical test of potentiodynamic polarisation measurement is implemented. Although this is a laboratory scale testing method, information provided from the assessed results including the corrosion rate, passivation and corrosion behaviour in a chosen environment are sufficient for the primary understanding of the materials properties of interest at present stage.

3.1 The Polarisation Diagram

The results of potentiodynamic polarisation measurements are graphically presented in a plot of potential-current density diagram, which is also called the polarisation diagram (Figure 6). The logarithmic scale is used for the current density (unit: $\mu A \cdot cm^{-2}$) to cover the broad range of interest, while the linear scale is used for the voltage (unit: mV). The axes in the plot are interchangeable according to different studies [7-11,61-65,71-90]. In the diagram, some electrochemical characteristics including corrosion potential (E_{corr}), passivation potential (E_{pass}), and pitting (also called breakdown) potential (E_{pit} or E_{break}), transpassive potential (E_{trans}), as well as their corresponding current densities (i, $\mu A/cm^2$) can be determined, and thereby the active, passive and transpassive regions can be defined. Other measured parameters and corrosion properties like the anodic and cathodic Tafel's constants (β_a and β_c), and polarisation resistance (R_p, $\Omega \cdot cm^{-2}$) can be derived graphically and mathematically (read Appendix A) [95]. In general, low current density at the free corrosion potential, low passive current density (i_{pass}), wide passive region (or working potential) (E_{range}) and high pitting or transpassive potential indicate better corrosion properties of the materials. Higher free corrosion potential also reflects more "noble" character of the material in the specific test environment. Note that Figure 6

provides simplified general characteristics of the polarisation curves and that various side reactions or overlapping processes can complicate the appearance in the real measurements. More about the polarisation testing instrument, the potentiostat, and the electrochemistry correlated to polarisation curve will be introduced and discussed in Appendix A.

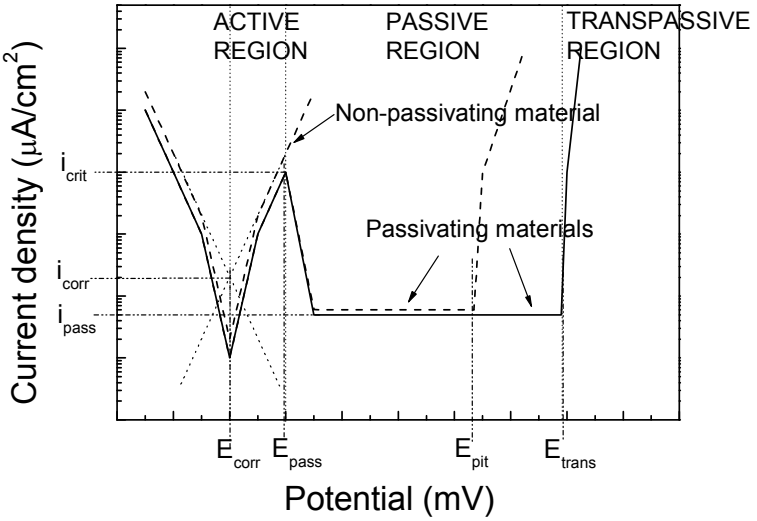

Figure 6 Schematic diagram showing the potentiodynamic polarisation diagram (Author's illustration).

3.2 Anodic Dissolution

The theoretical basis for an electrochemical corrosion is derived from the mixed potential theory [17]. In essence, this theory states that the total rate of all the oxidation reactions equal the total rate of all the reduction reactions on a corroding surface. The anode usually corrodes by loss of electrons from metal atoms to form cations. These cations may remain in solution or react to form insoluble/soluble corrosion products. If the former case occurs, using the symbol for a metal atom contained within its solid structure, the ionisation (anodic reaction) can be represented by the following reaction:

$$M_{(s)} \rightarrow M^{z+}_{(aq)} + ze^- \qquad \ldots \text{(i)}$$

This is the generalised corrosion reaction that removes the metal atom by oxidising it to an ionic state. In this reaction, the number of electrons produced equals the valence of the metal ion produced. The mixed potential theory proposes that all the electrons generated by the anodic reactions are consumed by corresponding reduction reactions. The more common cathodic reactions encountered in aqueous corrosion are as follows [96].

The hydrogen evolution reaction, which is the dominant cathodic process in acidic solution:

$$2H^+_{(aq)} + 2e^- \rightarrow H_{2(g)} \qquad E^o_{SHE} = 0.0V \qquad \ldots \text{(ii)}$$

The oxygen reduction in acidic solution (pH = 0):

$$\tfrac{1}{2}O_{2(g)} + 2H^+_{(aq)} + 2e^- \rightarrow H_2O_{(l)} \qquad E^o_{SHE} = +1.23\ V \qquad \ldots \text{(iii)}$$

And the oxygen reduction in neutral (pH = 7) or basic (pH = 14) solution:

$$\tfrac{1}{2}O_{2(g)} + H_2O_{(l)} + 2e^- \rightarrow 2OH^-_{(aq)} \qquad E^o_{SHE} = +0.82\ V\ (pH = 7)\ \text{or}\ +0.399\ V\ (pH = 14) \ldots \text{(iv)}$$

(Other possible chemical reactions for the transition metals and silicon in acidic solution are attached in Appendix A [96].)

3.3 Anodic Oxidation (Passivation)

As mentioned in the previous section, when metal corrodes and metal ions are generated, the metal can be dissolved into the solution and the ions formed can also react with other species to form insoluble corrosion products. If the latter case happens and the reaction product is well-adhered on the surface with a coherent structure, this most likely means that a passive layer is built-up between the metallic material and the external environment. If this layer is electrically insulating or semiconducting, this implies that the mobility through the layer is significantly reduced. By this means, the corresponding measured current density during the polarisation measurements reduces, an "active-passive" transition "nose" is noted in the polarisation curve and the passive-state is, therefore, defined. This concept, passivity, was first introduced by Schönbein in 1836 [8].

Thin Oxide Film Development on Metallic Objects

The oxide layer growth of metal at ambient temperature can be explained by the quantum mechanical charge transfer Cabrera-Mott model (Figure 7) [59]. It defines the oxide growth mechanism as an electron tunnelling process and assumes that the mobility of ions is relatively negligible at low temperature. The mathematical oxide growth law is defined as a *direct logarithmic law*:

$$\frac{dx}{dt} = N \cdot \Omega \cdot \nu \cdot \exp\left(-\left(W - \frac{q \cdot a \cdot E}{k \cdot T}\right)\right) \quad \cdots \text{(v)}$$

in which x is the oxide thickness, t the time, N the number of mobile ions, Ω the oxide volume per mobile ion, υ the atomic vibration frequency, W the energy barrier, q the ionic charge, a half the ion jump, E the electric field V/x, k the Boltzmann's constant, and T the temperature.

or an *inverse logarithmic law*:

$$\frac{x_1}{x} = -\ln\left(\frac{(t+\tau)}{x^2}\right) - \ln(x_1 \cdot u) \quad \cdots \text{(vi)}$$

where $u = N \cdot \Omega \cdot \nu \cdot \exp\left(-\frac{W}{k \cdot T}\right)$, $x_1 = \left|\frac{q \cdot a \cdot V}{k \cdot T}\right|$ and τ is a constant which can be neglected if it is small compared with t.

The growth rate of an oxide depends on the protectiveness which is determined by the metal-oxide bonds in the individual structure. As discussed in Section 2.3, metal oxides are divided into network formers, intermediates and network modifiers. The growth rate of those network-forming or intermediate classes is governed by inverse logarithmic expression [59,60]. Conversely, the growth of modifying oxides is governed by the direct logarithmic expression [59,60].

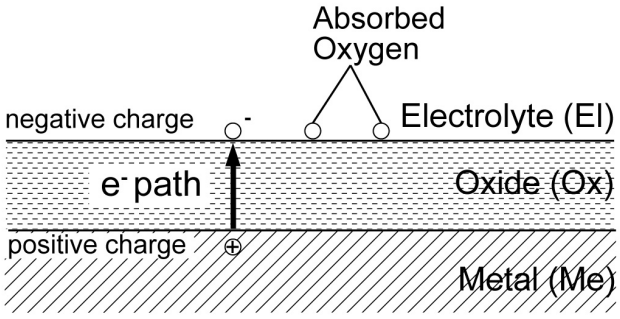

Figure 7 Cabrera-Mott's charge transfer model (Drawing based on [59]).

There are two commonly viewpoints regarding the nature of the passive film formation. They are the adsorption theory and the thin oxide films theory [8,97]. The adsorption theory suggests that metal such as chromium, aluminium, titanium, etc, are covered by a monolayer of chemisorbed ions, e.g. O^{2-}. This layer of anions displaces the adsorbed water molecules and slows down the rate of metal dissolution involving hydration of metal ions. The thin oxide film theory stipulates that a three-dimensional solid insulating film forms and it acts as a diffusion barrier layer of reaction products, which separates the metal from the aqueous environment, thereby the reaction rate is decreased.

3.4 Transpassivation

During polarisation measurement, when the applied potential is driven far beyond the passivation potential, the current density increases dramatically once again as can be seen for metallic dissolution in the active region. It is possible to say that the dissolution process of passive layer initiates. Without the presence of aggressive species (e.g. chloride) in the corrosive environment, it is considered that the dissolution process is electrochemically driven and the region in the polarisation diagram is defined as transpassive region. An example of transpassivation for stainless steel can be demonstrated in the sulphuric acid measurement at a potential beyond 1.2 V. The corresponding reaction can be read as:

$$Cr(OH)_{3(s)} + H_2O_{(l)} \rightarrow CrO_4^{2-}{}_{(aq)} + 5H^+_{(aq)} + 3e^- \quad \ldots \text{(vii)}$$

This chemical reaction tells that the oxidised chromium in the solid state form in passive layer gets oxidised from Cr(III) to Cr(VI). The Cr(VI) complex is soluble in the testing solution and thereby detaches from the stainless steel. In this condition, stainless steel is losing its self-healing capability and starts to corrode actively once the passive layer is totally consumed.

3.5 Pitting Corrosion

In the polarisation diagram, a current density increment at a potential beyond the passive region can also be reflected by the pitting corrosion process. The corresponding pitting potential (E_{pit}) is lower than that of transpassivation potential (E_{trans}) for the same tested material. The occurrence of pitting corrosion, besides the electrochemical driving force, also depends on the presence of aggressive ions in the environment. Basically, in order for pitting corrosion to occur, there should be an initial passive film and the material should experience sufficiently high anodic polarisation potential in an environment with aggressive anions such as Cl^- and F^-. Above the pitting potential, local anodic attack takes place. Of particular importance are the surface imperfections such as the presence of inclusions and grain boundaries, which provide sites for pitting corrosion attack. Non-metallic inclusions could preferentially dissolve in the corrosion process and create micro-crevice that will lead to pit development later on [17]. The pitting process can thus be viewed as process in which the passive film is locally broken in places depending on surface characteristics and local chemistry (e.g. chloride concentration) within the framework of the dynamic processes of continuous passivation, activation and re-passivation occurring on the surface. For the matrix element, Fe, in stainless steel, the pitting corrosion reactions under the action of Cl^- can be depicted as [17]:

$$FeOOH_{(s)} + Cl^-_{(aq)} \rightarrow FeOCl_{(aq)} + OH^-_{(aq)} \quad \ldots \text{(viii)}$$
$$FeOCl_{(aq)} + H_2O_{(l)} \rightarrow Fe^{3+}_{(aq)} + Cl^-_{(aq)} + 2OH^-_{(aq)} \quad \ldots \text{(ix)}$$

Clearly, with presence of Cl^-, destabilisation of the surface oxide is a possible result. On the other hand, considering the other major element, Cr, the dissolution of Cr-hydroxide can be expressed as:

$$Cr(OH)_{3(s)} + xCl^-_{(aq)} \rightarrow [CrCl_x]^{3-x}{}_{(aq)} + H^+_{(aq)} + H_2O_{(l)} + (x-3)e^- \ldots \text{(x)}$$

Upon formation of the passive film, preferential dissolution of Fe takes place facilitating the formation

of Cr-rich oxide/hydroxide on stainless steel [8]. With the presence of aggressive ions as Cl^- and the localised corrosion effects induced by the structural defects such as inclusions, the performance of the passive is deteriorated. Three major passivity breakdown theories developed in literature to explain the pit initiation including the ion migration mechanism, the adsorption mechanism and the film breakdown mechanism [98] are briefly described below.

Ion Migration Mechanism

This idea involves the transport of the aggressive anions through the passive film to the metal/oxide (or alloy/oxide) interface. Getting deeper into the content, it is proposed that the initiation of pits during ion penetration and migration is a result of the interchanging mechanism of oxides with aggressive anions (Figure 8). The more soluble metal chlorides are then dissolved into the corrosive solution, leading to the oxide network breakdown and pit formation later on [8,99].

Adsorption Mechanism

Placing the metallic specimen in an aqueous solution containing aggressive species, there is the accumulation of negative charges including the anions O^{2-} and OH^- on the specimen surface and thereby a "competitive adsorption" environment is established. The adsorption of aggressive anions would be an exchange of OH^- or O^{2-} from the oxide film. The corresponding halide or oxyhalide product has greater solubility than the oxide and results in partial or complete removal of the passive layer at these locations. If the passive layer becomes thinner, the corresponding underlying metal dissolution rate increases and pit initiates more readily (Figure 9) [8,99].

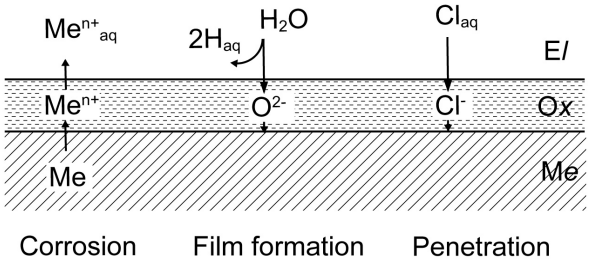

Figure 8 Ion migration mechanism (Drawing based on [97]).

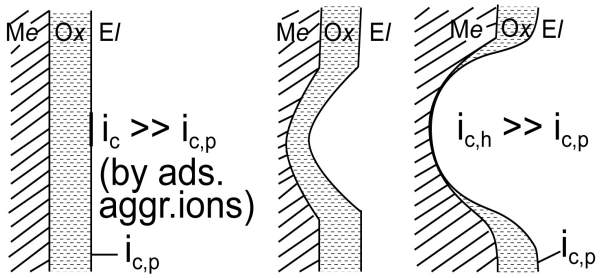

Figure 9 Adsorption mechanism (Drawing based on [8]).

Film Breakdown Mechanism

This theory considers that the passive film is in a continual state of breakdown and repair. Mechanical stresses arise at the weak sites and these become the critical areas of passivity breakdown as a consequence of electrostriction and surface tension effects owing to the surface chemistry changes on the thin film [99].

Pitting Propagation

Pitting is associated with a local discontinuity of the passive film in the form of mechanical imperfection. Pitting corrosion is an autocatalytic propagation process. When a local electrochemical cell is able to form on the metal surface, pitting can initiate. At the central anodic site, dissolution of the metal occurs. The increased concentration of metal ions within the growing pit results in the migration of chloride ions to maintain neutrality. The dissolved cations formed are hydrolysed by water to hydroxide and free acid and substantial acidification occurs in the pit. As soon as a pit has been formed, it will continue to grow autocatalytically. In a vicious circle, the pit creates the condition which promotes its further growth.

Chapter 4 Thin Film Fabrication and Materials Characterisation

4.1 Ion-Beam Sputter Deposition (IBSD)

Sputter deposition is a physical vapour deposition (PVD) technique that involves a high energetic beam of elementary particles like electrons or ions to bombard the target material, sputter out the atoms, and then deposit them on the substrate surface. Thin films deposited by means of this technique are found to be of high adhesiveness, high density, uniformity, and often amorphous in nature [101-103]. In this study, the Kaufman-type ion source, a technique invented at the National Aeronautics and Space Administration (NASA) in the United State during 1960s for spacecraft engine [104], is being used as ion-beam generator. In the Kaufman-type ion source, plasma is generated when a flow of inert gas is introduced into a high vacuum closed cylindrical volume and ignited by a discharge voltage (V_d) at the cathode. The generated plasma will be isolated and sustained in the closed volume. On one end side of this close volume, there are two molybdenum (Mo) grids that are well aligned together and an external negative "accelerator voltage" (V_a) passes through these grids. When the positively charged ions impinge on the open grids, these ions will be accelerated and can then leave the source in the form of a broad beam that impinges onto the target materials. To avoid developing a bias on the ground target materials, an electron-emitted tungsten filament (W) called 'neutraliser' is used for limiting the charge build-up on the target by compensation the electrons to the positively charged inert gas ions. Figure 10 and 11 show the schematic diagram of the Kaufman-type ion source and the mechanism of ion-beam sputter deposition (IBSD) [105-107]. In order to generate the binary-component thin films of different compositions, two fabrication approaches have been implemented in this work. One way was to conduct co-sputter deposition by using two ion sources and two targets. By varying the ion beam voltage of the individual ion source, thin film with controlled silicon to transition metal ratio and smooth surfaces could then be achieved. Other advantages with the co-sputtering method include the generation of a sharp coating-substrate interface and the reduction of silicide formation temperature during the deposition [101]. Another approach to achieve the binary-component thin film was to perform single target deposition on Si wafer and followed by vacuum annealing treatment. Heat treatments at different temperature for different transition metal silicides help the development of different silicide phases with higher crystallinity compared to the co-depositing technique [101-103].

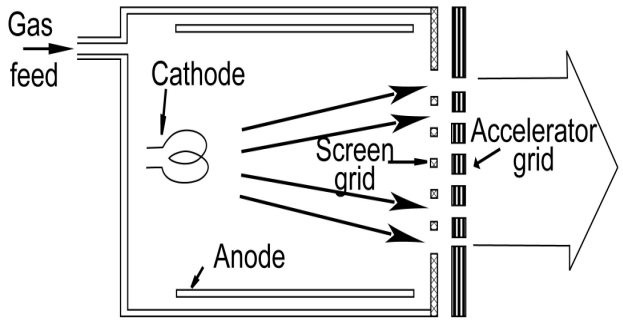

Figure 10 Cross-section of a Kaufman-type ion source (Drawing based on [105]).

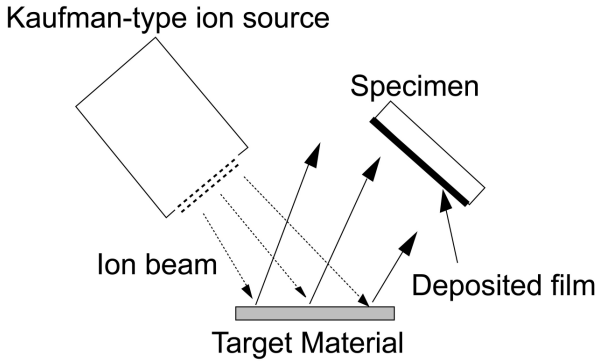

Figure 11 Schematic diagram showing the sputter deposition process (Drawing based on [104,107]).

Structure of the Sputtered Films

The idea of developing silicide films into two structural forms for properties comparison originate from a concept in materials science that better mechanical and chemical properties can be found in the amorphous form [108,109]. In fact, literature related to corrosion studies show that amorphous materials always show better corrosion resistance than their crystalline counterparts owing to the higher chemical homogeneity, the lower defect density and the capability of forming uniform and protective passive layers [110-116]. Therefore, it is interesting to check if the same proof is valid or not in the transition metal silicide thin films. Structural investigation of a pair of Ni-Si films with the same compositions but in different degree of crystallinity have been conducted by means of TEM and the cross-section images are shown in Figure 12. Crystallite features can be observed in the annealed specimen but not in the co-sputtered one, together with the diffraction pattern acquired from the GIXRD measurements (Figure. 13), the results show that long-range order or crystalline structure can be achieved through vacuum annealing process, while short-range order (vitreous) or no ordering (amorphous) thin film appears for the co-sputtered state.

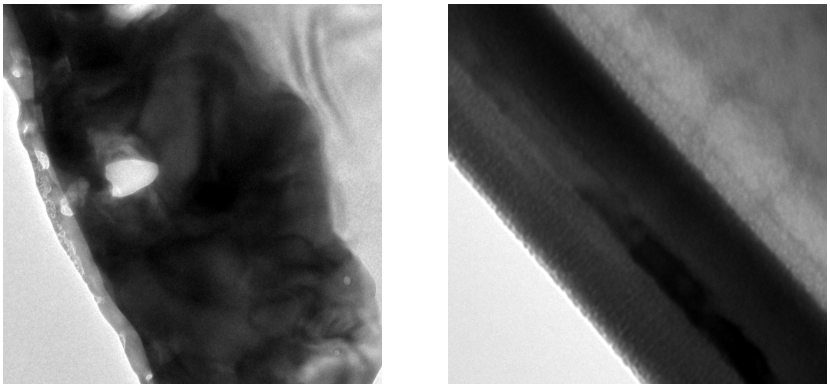

Figure 12 Cross-sectional TEM images showing (a) a thermally annealed Ni-Si thin film; and (b) a co-sputtered Ni-Si thin film (Results not included in the appended papers and are developed by Dr. Yiming Yao together with Prof. Uta Klement and the thesis author).

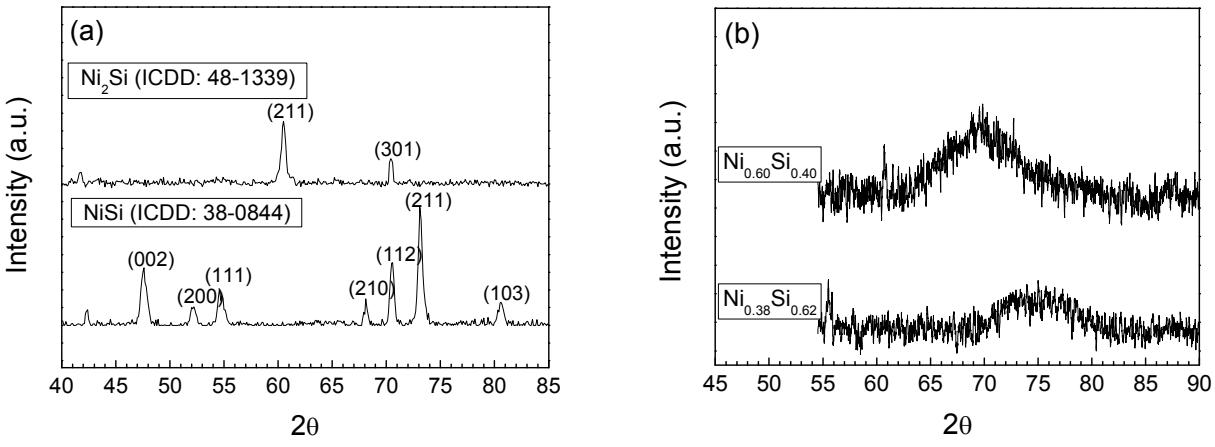

Figure 13 GIXRD of two pairs of Ni-Si thin films with the similar chemical compositions but different degree of crystallinity: (a) thermally annealed pair; (b) co-sputtered pair (Results in Paper 4).

4.2 Silicide Characterisation

Structure, phase formation and chemical composition of the silicide thin films were characterised by means of X-ray diffraction (XRD) and X-ray photoelectron spectroscopy (XPS) techniques. Also, a theoretical approach of the effective heat of formation (EHF) model [57,58] was used to predict the possible phases formed in the annealed specimens. The background about individual characterisation technique and the EHF model is found in Appendices B and C.

Structural characterisation of thin films needs to be done at the uppermost part of the characterised specimen (in micron scale) and therefore grazing incidence setup in the X-ray diffractometer is a must to acquire the maximum amount of diffracted X-ray signal from the top layer. The diffraction patterns in Figure 14 show different Ni-Si phases that originate from a Ni/Si system after thermal annealing processes at different temperatures. The sharpness of the characteristic peaks is related to the crystallinity of the characterised thin films. For amorphous or vitreous structure, a broad halo peak would be shown instead as illustrated in Figure 13(b). In Figure 14, the number of peaks and intensity of the peaks determine the symmetry and the degree of crystallinity, respectively, of the crystal structure. In principle, crystal structures with higher symmetry yield fewer peaks in the diffraction pattern. By this means, Ni and $NiSi_2$ have higher symmetric compared to Ni_2Si and NiSi. Nevertheless, the formation of each phase is temperature and time dependent [57,58]. For higher crystallinity, higher intensity of peaks would be acquired. Silicide mixture is not uncommon to be synthesized if the inappropriate annealing temperature has been chosen in accordance with the experimental studies in the research.

The chemical information about each silicide thin films is mainly obtained by means of XPS. Basically, the result is simply presented as the photoelectron emission spectrum as shown in Figure 15 and this spectrum presents the binding energy peaks for emitted photoelectrons from both the inner core levels and the valence electron levels of the characterised specimen. With the characteristic binding energy positions of the core electrons from all the elements, the approximate surface composition of the specimen can be evaluated through measuring the intensity ratio of individual peaks with the consideration of sensitivity factors [117-119].

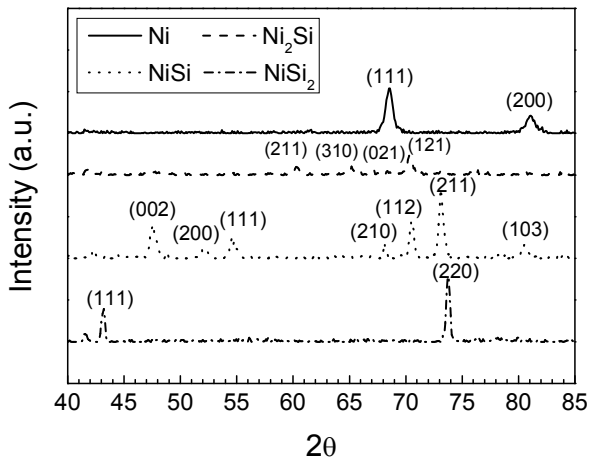

Figure 14 Diffraction patterns of the Ni-Si system after annealing processes at different temperatures (Author's results).

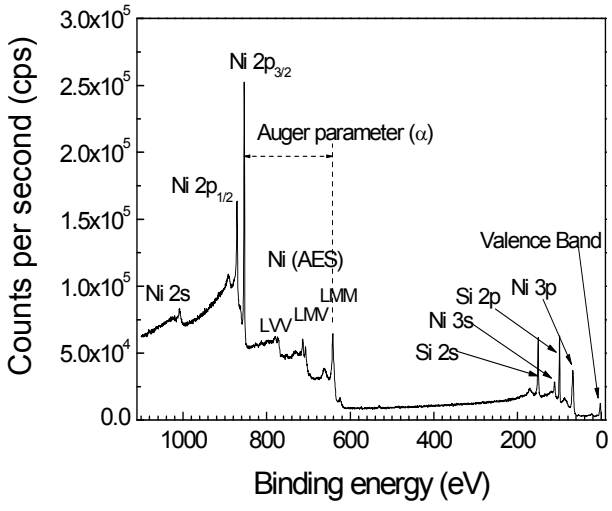

Figure 15 XPS survey spectrum of a $NiSi_2$ thin film (Author's results).

While the peak intensity ratio tells the chemical composition, the binding energy position of the photoelectron for a particular XPS signal for an element tells the possible chemical state of that element. Figure 16 illustrates the binding energy shift of Ni from metallic state to intermetallic state of $NiSi_2$. Besides the binding energy position, the change of peak symmetry, peak width and the disappearance of satellite peak are also the characteristic features. In Paper 2, binding energy shifts of the transition metal in the transition metal disilicides of Ti-Si, Cr-Si, Fe-Si and Ni-Si compared to their metallic states were investigated and the results show that the silicidation process leads to transition metal core-level XPS peaks that start from a negative binding energy shift to a prominent positive binding energy shift when passing from left to right across the transition metal series. Further explanation of this phenomenon can be developed by considering the initial-state and final-state Auger parameters as illustrated in a Wagner plot (Figure 17). For example, the silicidation process of Ni to $NiSi_2$ means that the binding energy shift (ΔE_b) of the Ni $2p_{3/2}$ signal is mainly governed by the initial-state Auger parameter ($\Delta\beta$). This is related to the fact that the screening effect for Ni atom by the surrounding Ni atoms is greatly reduced and thus an isolated/atomisitic Ni structure is actually established in the disilicide. As a result, the interaction between the nucleus and core-level electron increases significantly and leads to the increment of binding energy value. Meanwhile, the change of the initial-state effect is relatively insignificant in comparison with the other silicide systems. Thereby, higher contribution from the final-state effects ($\Delta\alpha$) or the extra-atomic relaxation energies (ΔR) will be the results and smaller binding energy shifts can be observed from the other silicides (see Table 7).

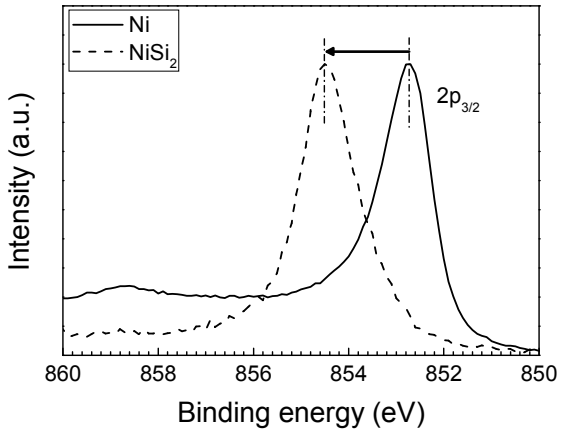

Figure 16 Binding energy shift of Ni $2p_{3/2}$ from Ni state to $NiSi_2$ state (Results in Paper 2).

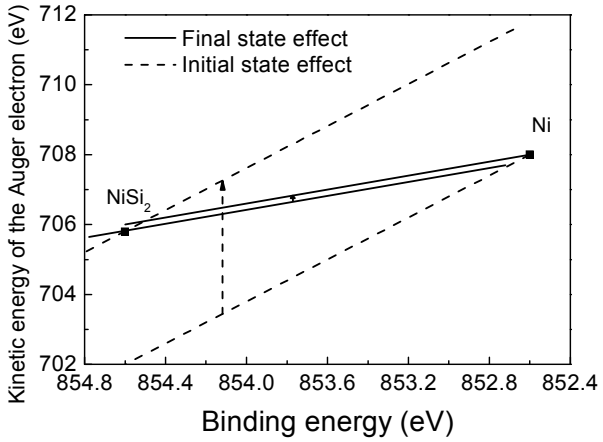

Figure 17 Wagner plot illustrating the initial-state and final-state effects of Ni in Ni state and $NiSi_2$ state (Results in Paper 2).

Table 7 Binding energy lines in the XPS measurements for different characterised thin films (Results in Paper 2)

Thin film	Transition metal $2p_{3/2}$	ΔE_b ($2p_{3/2}$)	KE of Auger electron (eV)	Δ Auger	Auger parameters				ΔE_b	ΔR
					α (Final-state effects)	Δα	β (Initial-state effects)	Δβ		
Ti	454.2	-0.3	388.6	0	842.8	-0.3	1751.2	-0.9	-0.30	-0.15
$TiSi_2$	453.9		388.6		842.5		1750.3			
Cr	574.3	-0.1	489.2	-0.9	1063.5	-1.0	2212.1	-1.2	-0.10	-0.50
CrSi + $CrSi_2$	574.2		488.3		1062.5		2210.9			
Fe	706.7	+0.3	598.5	-0.7	1305.2	-1.4	2718.6	-0.8	+0.3	-0.70
$FeSi_2$	707.0		596.8		1303.8		2717.8			
Ni	852.6	+2.0	708.0	-3.2	1560.6	-0.2	3265.8	+3.8	+2.0	-0.10
$NiSi_2$	854.6		705.8		1560.4		3269.6			

The atomic interaction or the bonding nature of the elements on the surface can be studied through the valence band spectrum in the XPS measurements. Figure 18 presents the valence band spectra of Ni-Si system extracted from Paper 1. In this figure, the main peak appearing on the Ni spectrum belongs to the electron in $3d_{5/2}$ state and the shoulder is the satellite peak. On the other hand, two peaks are found in the Si spectrum that represent 3p and 3s states, respectively. After the silicide formation, the valence band levels for the individual elements interact and the hybridisation of the 3d orbital of the transition metal and the 3p orbital of the silicon results. The result of hybridisation shifts the binding energies of both 3d and 3p states and the previous dominant 3d peak diminishes. By this means, electrons in the 3d state and 3p state are shared. The disappearance of the shoulder peak for Ni results with the consumption of free moving electrons. By increasing the Si concentration, there is clearly the positive shift of binding energy position of the main peak and this implies that more silicon-type or covalent-character bonds have been developed in the thin film systems. Similar results and discussion can also be developed for the other silicides and the details are found in Paper 2.

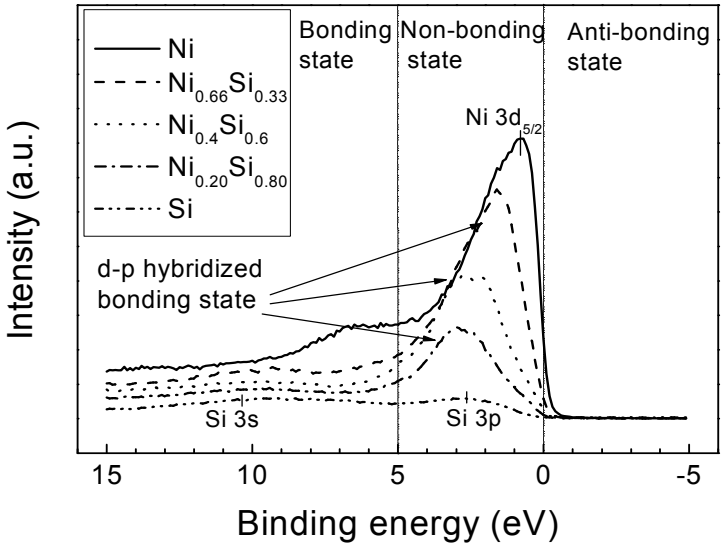

Figure 18 Valence band spectra in the Ni-Si film series samples (Results in Paper 1).

Clearly, the core-level binding energy shifts of the transition metal in the XPS measurements can show the possible chemical states of transition metal silicides. Still without the aid of phase identification via XRD, the XPS binding energy characterisation of thin film with short-range order or amorphous structure would be questionable. Therefore, a correlation study applying both XRD and XPS for each silicide phase is necessary at the beginning of work for specific silicide identification. After that, it is possible to investigate the silicides with lower crystallinity through the existing database.

As mentioned at the beginning of this chapter, higher crystallinity of silicide thin films can be achieved through thermal annealing process. Meanwhile, silicide mixtures cannot be avoided if inappropriate annealing temperature has been chosen. With the known concentration at the beginning before the annealing process, it is possible to predict the initial silicide phase formation as well as the subsequent silicide form in a particular silicide system through the Pretorius's effective heat of formation (EHF) model [57,58]. Table 8 shows some transition metal silicide thin films prepared by co-sputtering deposition and heat treated at a desired temperature to promote the formation of crystalline disilicides. Although most of the silicide systems work out, the expected single phase formation of $CrSi_2$ was not possible to achieve. The cause of silicide mixture formation for the Cr-Si system is supposed to be a result of the partial decomposition of the first formed $CrSi_2$ phase into CrSi and Si, which is out of the scope of the EHF model predictions. Nevertheless, with the confirmation of silicide phases from the XRD analyses, the XPS binding energy of specific silicides are then defined and can also be used to interpret the possible transition metal silicide with low crystallinity from the positions of the XPS peak positions recorded. Table 9 shows the results for the Ni-Si film series in deposited form in X-rays amorphous condition, fabricated by means of the co-sputter deposition.

Table 8 Composition of different transition metal silicide thin films by means of XPS quantitative analysis and the possible phase formation upon annealing predicted by effective heat of formation (EHF) model (Results in Paper 2)

Specimens	Possible phases	Congruency	Compound composition (at.%)	ΔH^o ($kJ \cdot mol^{-1} \cdot at^{-1}$)	Limiting element	Effective concentration (at.%)	$\Delta H'$ ($kJ \cdot mol^{-1} \cdot at^{-1}$)	Phase formed
$Ti_{0.40}Si_{0.60}$	Ti_3Si		$Ti_{0.75}Si_{0.25}$	-53.0	Ti	40	-28.3	
	Ti_5Si_3	C	$Ti_{0.62}Si_{0.38}$	-72.4	Ti	40	-46.3	
	Ti_5Si_4		$Ti_{0.56}Si_{0.44}$	-81.0	Ti	40	-57.9	
	TiSi		$Ti_{0.50}Si_{0.50}$	-78.6	Ti	40	-62.9	
	$TiSi_2$	C	$Ti_{0.33}Si_{0.67}$	-57.0	Si	60	-51.0	$TiSi_2$
$Cr_{0.20}Si_{0.80}$	Cr_3Si	C	$Cr_{0.75}Si_{0.25}$	-34.4	Cr	20	-9.2	
	Cr_5Si_3	C	$Cr_{0.62}Si_{0.38}$	-35.0	Cr	20	-11.2	
	CrSi		$Cr_{0.50}Si_{0.50}$	-30.2	Cr	20	-12.2	
	$CrSi_2$	C	$Cr_{0.33}Si_{0.67}$	-25.8	Cr	20	-15.6	$CrSi_2$
$Fe_{0.40}Si_{0.60}$	Fe_3Si		$Fe_{0.75}Si_{0.25}$	-25.8	Fe	40	-13.8	
	FeSi	C	$Fe_{0.50}Si_{0.50}$	-39.3	Fe	40	-31.4	FeSi
	$FeSi_2$		$Fe_{0.33}Si_{0.67}$	-30.6	Si	60	-27.4	
$Ni_{0.25}Si_{0.75}$	Ni_3Si		$Ni_{0.75}Si_{0.25}$	-37.2	Ni	25	-12.4	
	Ni_5Si_2	C	$Ni_{0.71}Si_{0.29}$	-42.3	Ni	25	-14.9	
	Ni_2Si	C	$Ni_{0.67}Si_{0.33}$	-46.9	Ni	25	-17.5	
	Ni_3Si_2		$Ni_{0.60}Si_{0.40}$	-45.2	Ni	25	-18.8	
	NiSi	C	$Ni_{0.50}Si_{0.50}$	-42.4	Ni	25	-21.2	NiSi
	$NiSi_2$		$Ni_{0.33}Si_{0.67}$	-29.3	Ni	25	-22.2	

Table 9 The prediction of phase formation in the Ni-Si film series utilising Pretorius' EHF model (Results in Paper 1)

Thin film specimens	Composition	ΔH° (kJ·mol^{-1}·at^{-1})	Limiting element	Effective concentration (at.%)	Compound concentration (at.%)	ΔH′ (kJ·mol^{-1}·at^{-1})	Phase formation
$Ni_{0.66}Si_{0.33}$	*$Ni_{0.67}Si_{0.33}$*	*-46.9*	*Ni*	*66*	*67*	*-46.2*	*Ni_2Si*
	$Ni_{0.50}Si_{0.50}$	-42.4	Si	33	50	-28.0	
	$Ni_{0.33}Si_{0.67}$	-29.3	Si	33	67	-14.4	
$Ni_{0.40}Si_{0.60}$	$Ni_{0.67}Si_{0.33}$	-46.9	Ni	40	67	-27.6	
	$Ni_{0.50}Si_{0.50}$	*-42.4*	*Ni*	*40*	*50*	*-33.9*	*NiSi*
	$Ni_{0.33}Si_{0.67}$	-29.3	Si	60	67	-26.2	
$Ni_{0.20}Si_{0.80}$	$Ni_{0.67}Si_{0.33}$	-46.9	Ni	20	67	-14.0	
	$Ni_{0.50}Si_{0.50}$	*-42.4*	*Ni*	*20*	*50*	*-17.0*	*NiSi*
	$Ni_{0.33}Si_{0.67}$	*-29.3*	*Ni*	*20*	*33*	*-17.6*	*$NiSi_2$*

Other than the silicide state characterisation, the core-level Si 2p spectrum plays an important on silicide oxidation characterisation. Since silicon has much higher oxygen affinity compared to the transition metal, silicon oxidation is much more efficient and thus becoming a crucial factor of the corrosion resistivity of the transition metal silicide thin films. It is supposed that the silica (SiO_2) is an effective passive layer that can withstand many aggressive corrosion environments [48]. Note that the binding energy of the Si 2p of silicon state is 99.4 eV, silicide state 99.3 – 99.7 eV, and oxide state at 103.0 – 104.0 eV (Figure 19). The binding energy level of the Si-peak for the silica state depends on the integrity of the silica layer and the layer thickness, i.e. a thicker layer gives an apparent higher binding energy value. The effect is partly related to the insulating nature of the layer, i.e. charging effects [120].

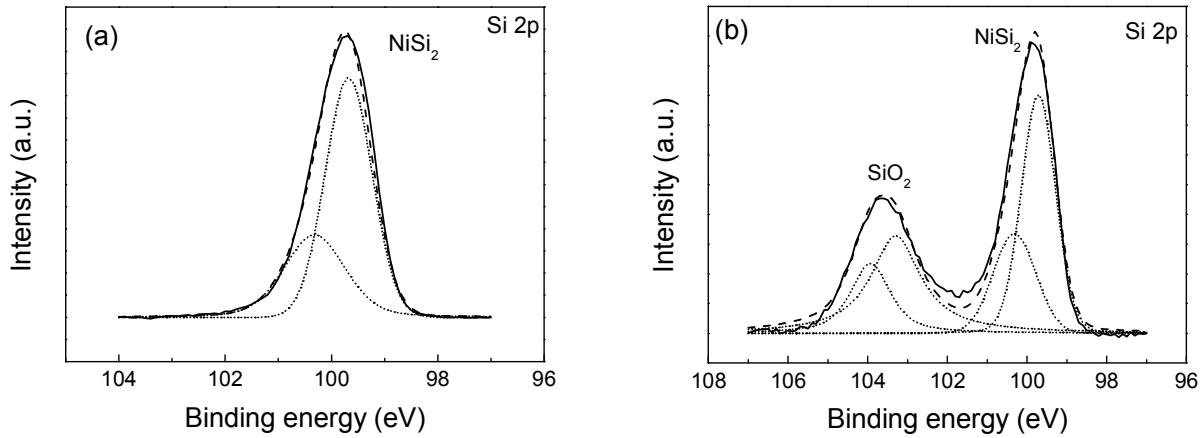

Figure 19 Binding energy spectra of a pair of Si 2p (a) before and (b) after oxidation in the $NiSi_2$ thin film (Results in Paper 3).

Chapter 5 Thin Film Properties

5.1 Corrosion Properties

Corrosion properties of the transition metal silicide thin films have been studied in three stages and reported in separate articles (Papers 3 to 5). This part of work was started with the Ni-Si system of different compositions (Paper 3). Based on the findings from this preliminary work, the optimum composition with high corrosion resistance was chosen and the investigation was then extended to the other transition metal silicide systems, i.e. Ti-Si, Cr-Si and Fe-Si (Paper 5). Furthermore, it was also considered that the short-range order or no ordering structure might have beneficial effect to the corrosion resistance. Therefore, a comparative study of two pairs of Ni-Si with the similar compositions but different degree of crystallinity (Paper 4) was conducted in order to find out the potential impact induced by the structural design of thin film.

To start with, the polarisation diagrams of the Ni-Si films series after the 0.05 M hydrochloric acid (HCl) tests (pH = 1.3) are shown in Figure 20 and the electrochemical characteristics are summarised in Table 10. The results of these curves show that the corrosion resistance of the coated specimens are better than the uncoated 304L steel since all the polarisation curves have relatively lower current densities. The lower corrosion current density (i_{corr}) at the corrosion potentials (E_{corr}) and higher polarisation resistances (R_p), thereby, implies the higher self-corrosion resistance of the coated samples than the uncoated steel. When considering the silicide composition, it is found that Ni-Si films with high Si contents (i.e. $Ni_{0.40}Si_{0.60}$ and $Ni_{0.20}Si_{0.80}$) give higher polarisation resistances than that with low Si content (i.e. $Ni_{0.66}Si_{0.33}$) and the pure Ni film. This means that high Si content is an important factor to improve the corrosion resistance in the Ni-Si system. Furthermore, the small E_{corr} differences between the 304 substrate and all Ni-Si films imply that only small galvanic effect at these silicide-304L interfaces will be induced when either side is damaged. By this means, it is expected that Ni-Si thin film can give good corrosion protection to or improve the corrosion resistance of 304L stainless steels.

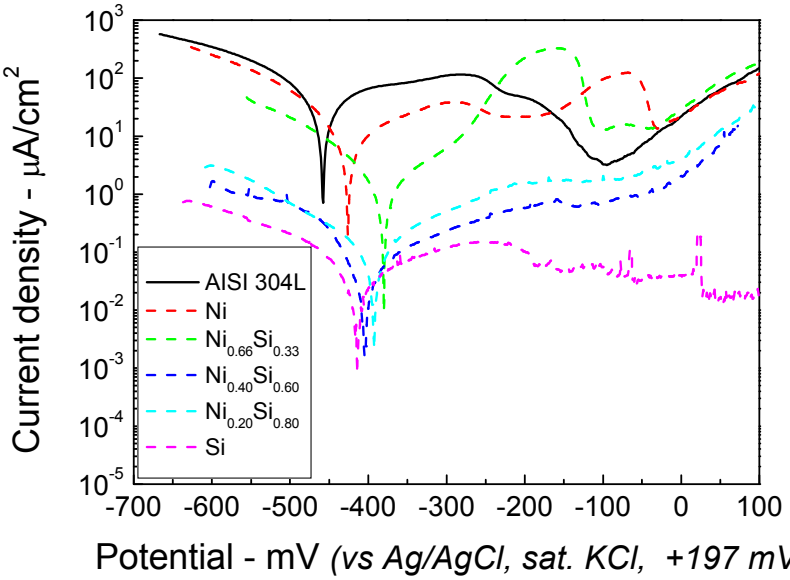

Figure 20 The polarisation curves in the Ni-Si films series, the elemental Ni and Si films and the 304L stainless steel tested in 0.05 M HCl solution (Results in Paper 3).

Table 10 Highlighted electrochemical characteristics in the polarisation curves (Results in Paper 3)

	304L	Ni	$Ni_{0.66}Si_{0.33}$	$Ni_{0.40}Si_{0.60}$	$Ni_{0.20}Si_{0.80}$	Si
Corrosion current density (i_{corr} – μA/cm^2)	240	54	3.4	0.23	0.62	0.25
Corrosion potential (E_{corr} vs Ag/AgCl – mV)	-460	-430	-380	-400	-390	-410
Corrosion potential (E_{corr} vs SHE – mV)	-263	-233	-183	-203	-193	-213
Polarisation resistance (R_p – Ω/cm^2)	310	1065	6630	2.0×10^5	1.0×10^5	3.0×10^5

Based on this finding, transition metal silicide thin films of other systems were deposited with silicon content at or above 65 %. Under the same polarisation environment but faster scanning rate, the polarisation diagrams were measured and are plotted in Figure 21. Basically, besides Ti-Si specimen, there is no significant difference among different silicide thin films and the 304 steel. They are all showing the similar polarisation behaviour for their close corrosion potential (E_{corr}), corrosion current density (i_{corr}), passivation potential (E_{pass}), passive current density (i_{pass}) and common pitting potential (E_{pit}). The polarisation measurements imply that the different transition metal silicides, except Ti-Si, share the similar polarisation behaviour as stainless steel. For Ti-Si, the polarisation curve is exceptionally lower in current density thus indicating its chemical inertness. The electrochemical characteristics during the polarisation measurements are summarised in Table 11. In all, the results show that the transition metal silicide thin films together with the uncoated stainless steel substrate are susceptible to the hydrochloric acid and therefore all silicide thin films cannot significantly improve the corrosion resistivity of 304 steel, except Ti-Si.

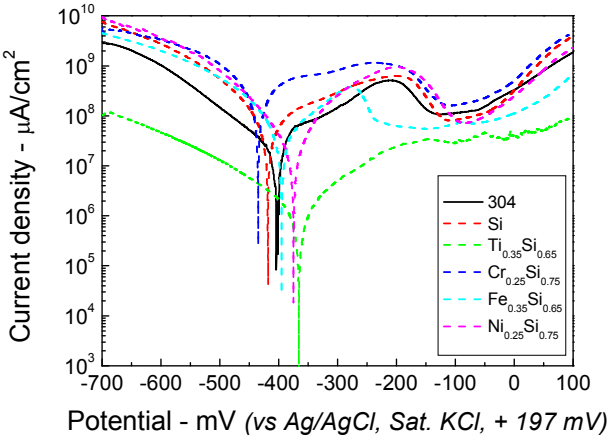

Figure 21 The polarisation diagram of (a) AISI type 304 stainless steel; (b) Si thin film; (c) Ti-Si thin film; (d) Cr-Si thin film; (e) Fe-Si thin film; and (f) Ni-Si thin film obtained from the potentiodynamic polarisation measurements in the 0.05 M HCl solution (Results in Paper 5).

Table 11 Data extracted from the polarisation experiments done in 0.05 M HCl (Results in Paper 5)

Thin film composition	$Ti_{0.33}Si_{0.67}$	$Cr_{0.25}Si_{0.75}$	$Fe_{0.30}Si_{0.70}$	$Ni_{0.25}Si_{0.75}$	Si	Bulk
Substrate	304	304	304	304	304	304
E_{corr} vs Ag/AgCl – mV	-345	-430	-400	-370	-420	-400
E_{corr} vs SHE – mV	-148	-233	-203	-173	-223	-203
i_{corr} - μA/cm^2	2	180	35	30	130	14
i_{crit} - μA/cm^2	2	570	190	940	620	510
i_{pass} - μA/cm^2	9	80	25	70	80	110
E_{pit} vs Ag/Cl – mV	100	-50	-55	-80	-40	-55
Working potential (mV)	230	170	230	120	150	150

While all specimens have failed to passivate under HCl attack, another silicide set with the same composition as above were prepared for sulphuric acid runs. The polarisation curves and the corresponding electrochemical characteristics are presented in Figure 22 and Table 12. Unlike the tests run in HCl, all specimens get passivated in this condition and clear passive regions are defined. However, only Ti-Si and Ni-Si sustained on the substrate surface at the end of the polarisation test according to the microscopic observation and thus Cr-Si and Fe-Si are not suitable for protective thin films application (read Paper 5).

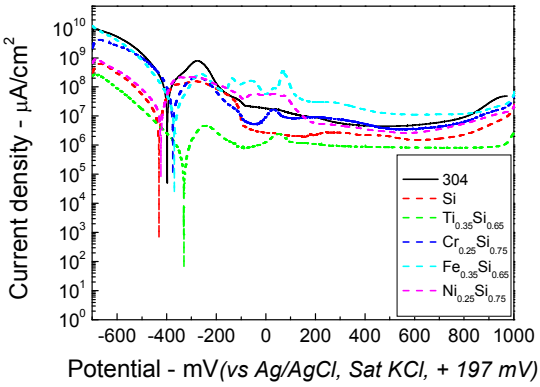

Figure 22 The polarization diagram of (a) AISI type 304 stainless steel; (b) Si thin film; (c) Ti-Si thin film; (d) Cr-Si thin film; (e) Fe-Si thin film; and (f) Ni-Si thin film obtained from the potentiodynamic polarisation measurements in the 0.50 M H_2SO_4 solution (Results in Paper 5).

Table 12 Data extracted from the polarisation experiments done in 0.5 M H_2SO_4 (Results in Paper 5)

Thin film composition	$Ti_{0.35}Si_{0.65}$	$Cr_{0.25}Si_{0.75}$	$Fe_{0.35}Si_{0.65}$	$Ni_{0.25}Si_{0.75}$	Si	Bulk
Substrate	304	304	304	304	304	304
E_{corr} vs Ag/AgCl – mV	-329	-370	-357	-421	-382	-397
E_{corr} vs SHE – mV	-132	-173	-160	-223	-185	-200
i_{corr} - µA/cm²	0.72	55.6	14.4	16.9	7.7	252
i_{crit} - µA/cm²	4.8	208	343	17.6	97.9	785
i_{pass} - µA/cm²	0.77	5.3	11.2	0.18	7.72	4.5
E_{trans} vs Ag/AgCl – mV	980	960	975	975	965	805
Working potential (mV)	1215	1230	900	1180	1155	1084

One interesting phenomenon is that the polarisation behaviours of Ni-Si thin films with different crystallinity do not show significant difference as can be seen in Figure 23. The results therefore imply that this factor does not have significant impact to improve the corrosion resistivity of silicide materials.

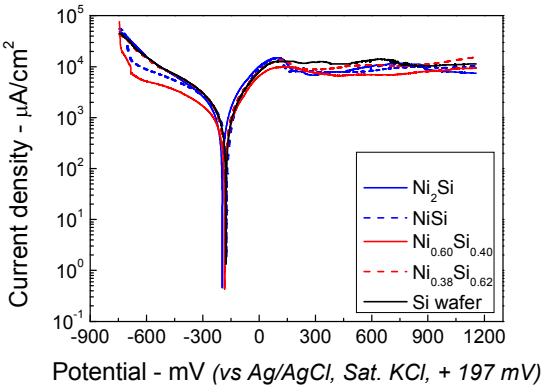

Figure 23 The polarisation curves of a Si wafer and two Ni-Si thin film pairs with similar compositions but different degree of crystallinity (Results in Paper 4).

5.2 Tribological Properties

Thin Film Adhesiveness

Thin film adhesiveness is characterised by means of the Rockwell-C adhesion test. A pair of indented marks for a pair of Ni-Si thin films with different crystallinity is shown in Figure 24. Since the micrographs show no lateral or radial microcracks, no flakes and no thin film delamination surrounding the indented mark, the nickel silicide thin films prepared by means of the ion-beam sputter deposition (IBSD) provided an excellent adhesiveness on 304 stainless steel substrate. Their practical reliability to static mechanical impact is thus guaranteed. The specification of this characterisation technique is further discussed in Appendix E [121-123].

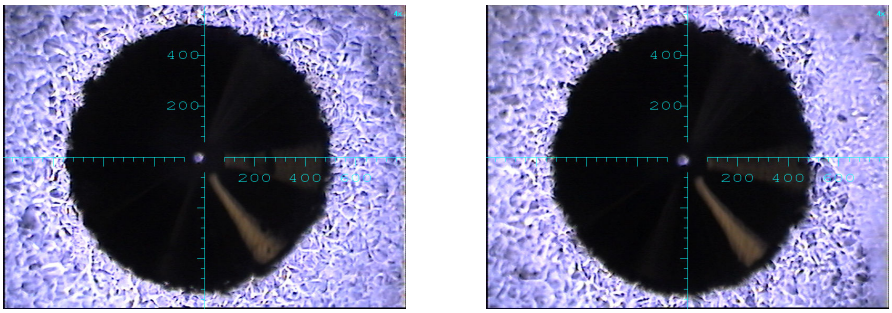

(a) (b)

Figure 24 Rockwell-C adhesion test on (a) the co-sputtered and (b) the heat-treated Ni-Si thin films (Results in Paper 6).

Hardness and Elastic Modulus

Static mechanical properties of the uppermost thin films such as hardness and modulus can be determined by means of nanoindentation measurements. Indentation tests for the above Ni-Si pair were conducted and their load-displacement curves are shown in Figure 25. The curves illustrate that both specimens behave in a similar way by showing a similar maximum penetration depth and smooth loading-unloading curves. The measured hardness and elastic modulus data on individual specimen (Table 13) indicate that structural design does not have much influence on the film mechanical properties. The small data scattering in the measurements show that both coated specimens have uniform mechanical properties in their surfaces. Further information about nanoindentation technique is discussed in Appendix F [124-129].

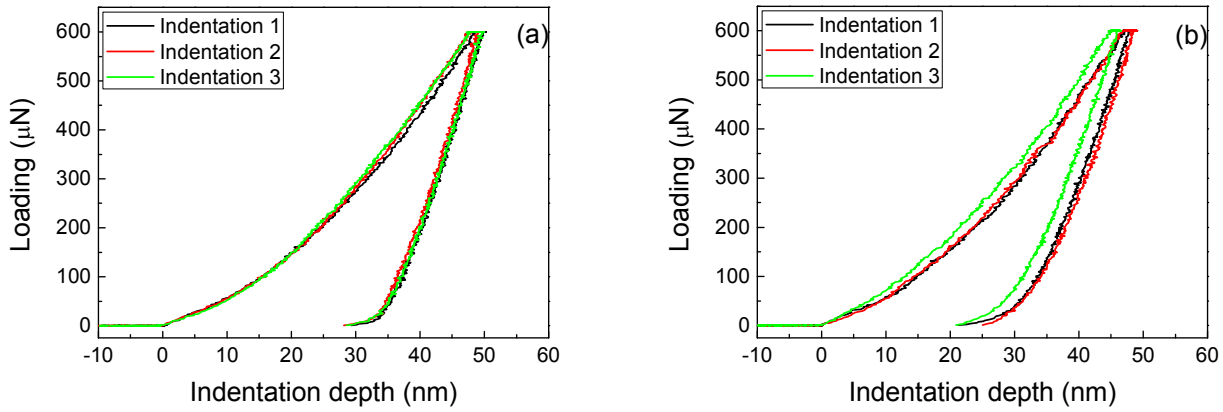

Figure 25 Load-displacement curves of (a) co-sputtered and (b) heat-treated Ni-Si thin film (Author's results).

Table 13 Mechanical properties of the nickel silicide thin films with different degree of crystallinity characterised by means of nanoindentation measurements and Rockwell-C adhesion tests (Results in Paper 6)

Specimen	H_{film} (GPa)	E^*(GPa)	Adhesiveness	R_q (nm)
Co-sputtered film	9.0 ± 0.2	144.0 ± 2.5	HF 1	14
Heat-treated thin film	10.0 ± 0.9	142.0 ± 11	HF 1	17

Surface Topography

Surface topography directly determines tribological properties and thus becomes an important consideration in practice. Surfaces of the above mentioned Ni-Si pair were mapped by means of atomic force microscopy (AFM) after nanoindentation measurements, see Figure 26 a(i) and b(i). Apparently, the linear profiles extracted from individual maps show that the surface roughness of co-sputtered thin film is less than that of the heat-treated one and the 'bumps' appearing on the latter specimen is a kind of crystallised feature. The roughness value (R_a) determined for co-sputtered specimen is 1.0 nm and that for annealed specimen is 2.0 nm. However, for the small scanning region in submicron-scale, it is doubtful to report this measured value. Therefore, R_a and/or R_q are also measured and reported by means of engineering-scale profilometry techniques instead (see Table 13). The values in Table 13 are approximately one order of magnitude larger than the R_a values derived by means of AFM. Technical information about AFM [130,131] and the profilometers are presented in Appendix G [132-134].

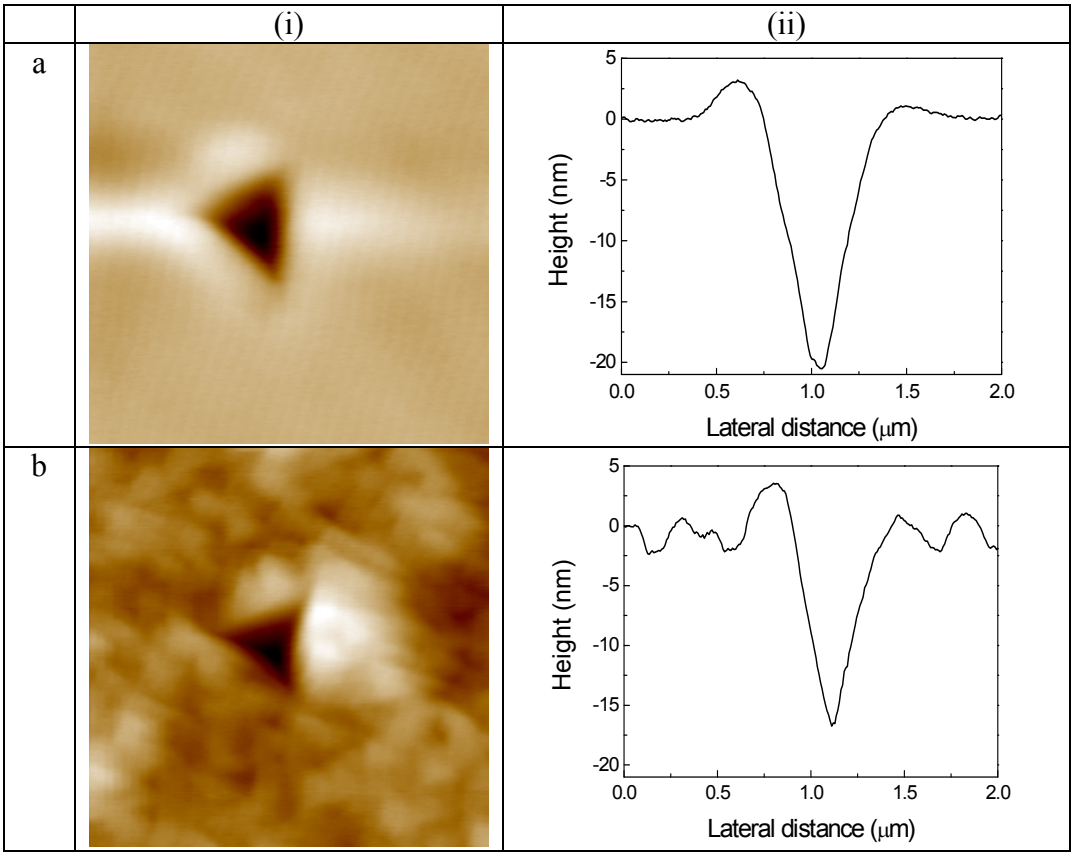

Figure 26 A pair of (i) AFM imaging surrounding the indented mark on (a) co-sputtered Ni-Si, and (b) heat-treated Ni-Si and (ii) the linear profile extract from the map (Author's results).

Wear Properties

The wear properties of the same Ni-Si thin film pair were evaluated through the dry sliding test in a reciprocating sliding wear instrument. The chosen mating counterbodies were a Cr-rich bearing steel (Cr-steel) ball and a tungsten carbide (WC) ball. Results are presented in friction coefficient curves and shown in Figure 27 and 28. It can be seen that friction coefficients of the two specimens under 5 N load are the same under both conditions, while lower friction coefficient was observed for the 2 N tests. Specific wear rate of individual test can be evaluated through measuring the volume of worn regions by means of profilometry and results are summarised in Table 5.5. It is concluded that there is less materials loss in the Cr-steel ball tests compared to the WC ball tests according to the measured wear volume.

Tungsten carbide ball tests

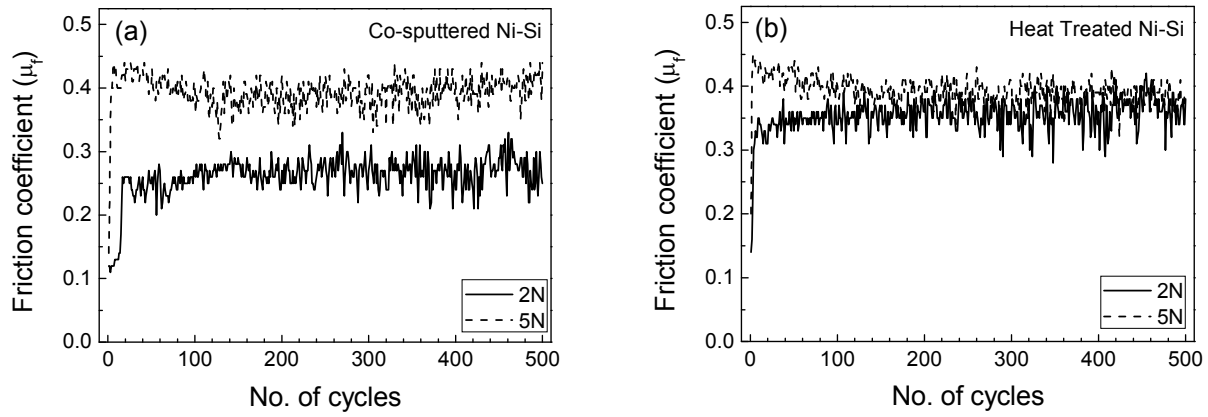

Figure 27 Friction coefficients (μ_f) as a function of the reciprocating sliding cycles in the tungsten carbide (WC) ball wear tests on (a) co-sputtered; and (b) heat-treated Ni-Si thin film coated on 304 stainless steel specimens (Results in Paper 6).

Cr-steel ball tests

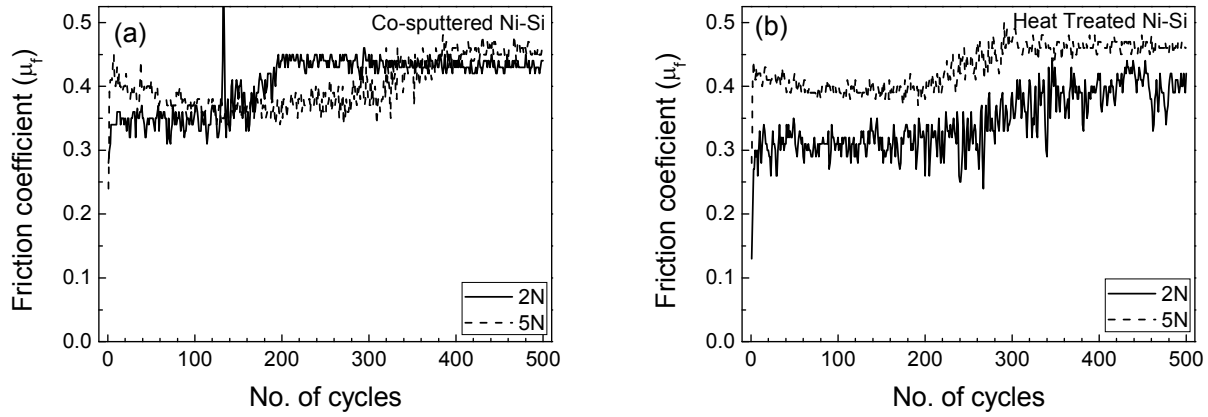

Figure 28 Friction coefficients (μ_f) as a function of the reciprocating sliding cycles in the Cr-steel ball wear tests on (a) co-sputtered; and (b) heat-treated Ni-Si coated 304 stainless steel specimens (Results in Paper 6).

Table 14 Tribological parameters from wear testing of Ni-silicide coated 304 stainless steels (Results in Paper 6)

Tested specimen	Counter-body	Sliding load (N)	Friction coefficient (μ_f)	Wear volume (m^3)	Specific wear rate ($m^3/N{\cdot}m$)
Co-sputtered Ni-Si coated steel plate	WC ball	2	0.25	1.52×10^{-12}	1.9×10^{-13}
	WC ball	5	0.40	4.25×10^{-12}	2.1×10^{-13}
	Cr-steel ball	2	0.35	7.20×10^{-12}	9.0×10^{-14}
	Cr-steel ball	5	0.35	2.85×10^{-12}	1.4×10^{-13}
Heat-treated Ni-Si coated steel plate	WC ball	2	0.35	1.53×10^{-12}	1.9×10^{-13}
	WC ball	5	0.40	4.23×10^{-12}	2.1×10^{-13}
	Cr-steel ball	2	0.30	1.10×10^{-12}	1.4×10^{-13}
	Cr-steel ball	5	0.40	3.68×10^{-12}	1.8×10^{-13}

In the surface profilometry measurements, it is observed that the cross-sectional profile of the worn region after the WC-ball test is smoother than the region after the Cr-steel ball test (Figure 29). A top view of the optical microscopy on the individual wear track shows there are some debris left over the surface after the Cr-steel ball wear test while it does not appear after the WC test (Figure 30). Therefore, it is believed that there is materials transfer from the Cr-steel ball to the silicide coated surface but not in the other case. Compositional analysis by means of EDX shows the debris on the co-sputtered silicide contains of Cr, Fe, and O and that on the heat-treated silicide contains of Fe and O only (reported in Paper 6). Together with the specific wear rate values, it is thereby concluded that the formation of Cr-containing oxide plays an important role in wear resistance improvement. A sliding wear test for the uncoated substrate was performed at the end of this work. For the higher friction coefficients against both counterbodies (Figure 31) and the larger measured wear volume, the specific wear rate of the 304 stainless steel is an order higher than those reported for the silicide specimens, i.e. 10^{-12} $m^3/N{\cdot}m$, and thus the silicide thin films somehow have a positive contribution to wear resistance improvement on stainless steel. It is believed that the higher wear resistance contribution of silicide is related to their harder nature as compared to stainless steel (i.e. 1 – 2 GPa) [129].

Co-sputtered Ni-Si thin film	**2N**	**5N**
WC ball	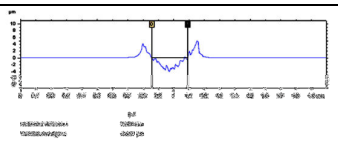	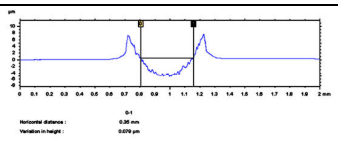
Cr-steel ball	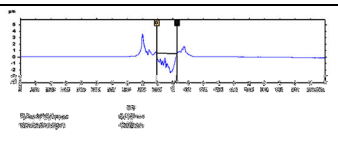	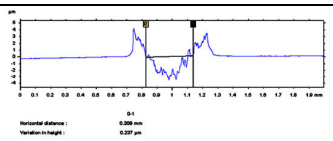
Heat-treated Ni-Si thin film	**2N**	**5N**
WC ball	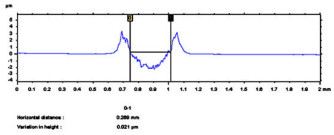	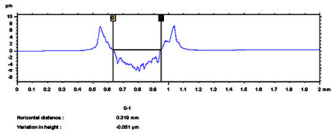
Cr-steel ball	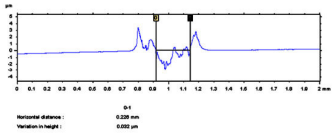	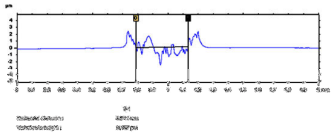

Figure 29 Cross-sectional profiles of the wear tracks developed on the two coated specimens after reciprocating sliding wear test against a WC-ball and a Cr-steel ball under 2 N and 5 N (Author's results).

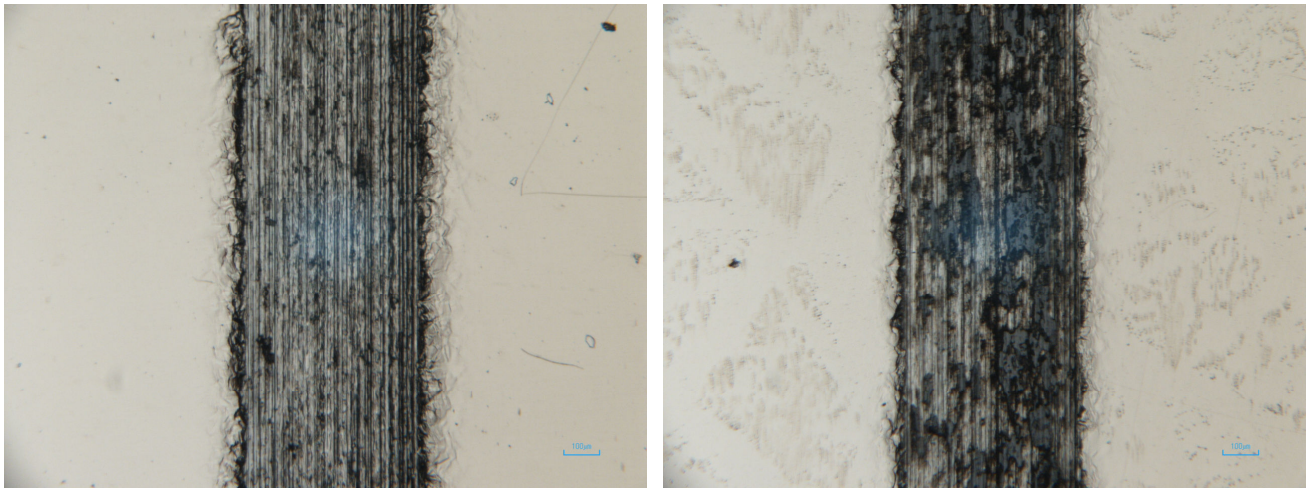

(a) **(b)**

Figure 30 Wear surface of the heat-treated Ni-Si specimen after the reciprocating sliding wear test against (a) a WC-ball; and (b) a Cr-steel ball at a load of 5 N (Author's results).

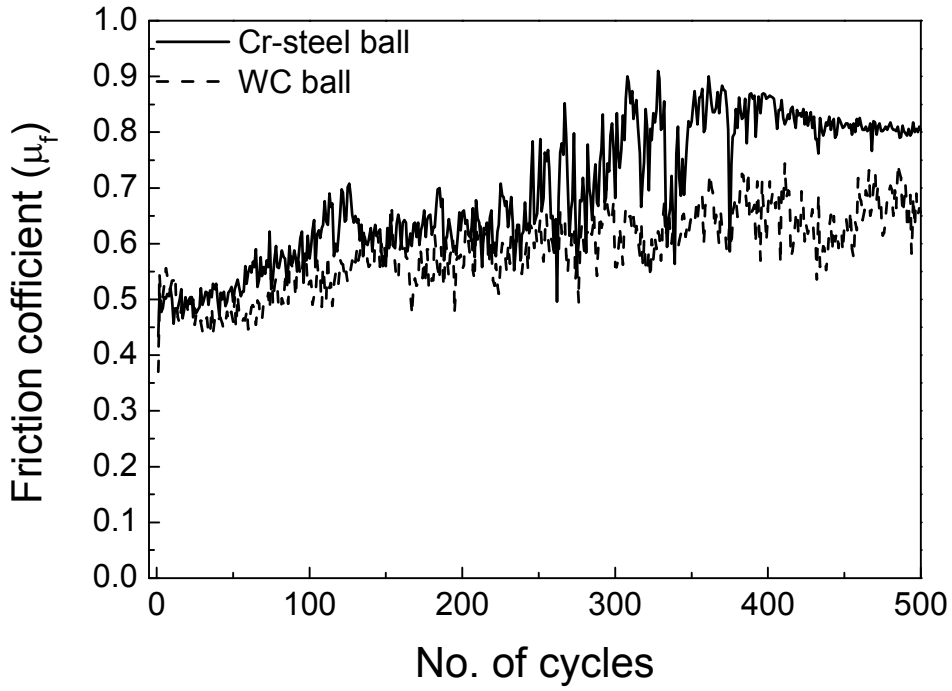

Figure 31 Friction coefficient (μ_f) as a function of the reciprocating sliding cycles in the Cr-steel ball wear tests on an uncoated 304 stainless steel specimen at a load of 5 N (Author's results).

Chapter 6 Conclusions

Transition metal silicides of Ti-Si, Cr-Si, Fe-Si and Ni-Si have been fabricated as thin films by means of ion-beam sputter deposition (IBSD) on AISI type 304 stainless steel substrate in order to enhance the corrosion resistance. Potentiodynamic polarisation measurements in hydrochloric acid (HCl) and sulphuric acid (H_2SO_4) of different silicides show that all thin films have higher corrosion resistance than the uncoated stainless steel by showing lower current density throughout the whole polarisation diagrams even though no significant difference have been found in the curve shape. However, only Ti-Si and Ni-Si films sustained on the stainless steel after the tests and thereby only these films have the potential to be protective thin films. Further investigations about varying the thin film composition and thin film structure were conducted on the Ni-Si system and the results show that the variation of composition has a more significant influence than that of structure to the corrosion resistance enhancement. It is found that transition metal silicide with Si content of at least 60 %, independent of the thin film crystallinity, would have better corrosion resistance to the tested environment than those with lower Si content. This is due to the formation of uniform passive layer of Si-oxide on the surface of the silicides and its chemical inertness plays a significant role in the corrosion resistance enhancement. Besides the corrosion properties, study of the tribological properties and some fundamental understanding about the thin films were also involved in this research. For the tribological tests, good adhesiveness was shown for a pair of Ni-Si thin film with different crystallinity on austenitic stainless steel. The reciprocating dry sliding wear test carried out on the same pair of specimens showed that thin films, independent on the structural crystallinity, improve the wear resistance slightly in comparison to the stainless steel substrate. By this means, silicide thin films not only enhance the corrosion resistance, but also strengthen the wear resistivity. With the proof of properties improvement, the nature of transition metal silicide thin films were further investigated by means of surface sensitivity characterisation techniques including GIXRD and XPS. With the aid of GIXRD, crystallinity of thin films as well as the possible phases appearing was depicted and it was shown that post-annealing treatment after IBSD promotes the thin film crystallisation and the development of a particular phase. Chemical information including the composition, chemical state of individual element in a silicide and the electronic structure can be determined from XPS analyses by simply evaluating the core level binding energy position of the transition metal component , the intensity ratio of the core-level peaks and the valence band spectra near to the Fermi energy level. More information about top layer thickness evaluation and binding energy shift can be investigated through ARXPS and the Auger parameter. The covalent character of the transition metal-silicon bonding explains the strong bonding between these in the intermetallic compound and thus the potential higher corrosion resistance compared to that of uncoated stainless steel substrates.

Chapter 7 Future Works

The current study about transition metal silicides as protective thin films on engineering materials is at fundamental level and many ideas can be put forward to develop this work in the future. The suggestions listed here are based on the scope of this thesis:

1. Thin Film Synthesis

Research progress is largely hindered by the thin film fabrication process. IBSD is a slow deposition technique and the lifetime of the filaments is short. Frequent replacements of the filaments interrupt the deposition process from time to time and the UHV chamber is inevitably contaminated in the atmosphere. As a result, the consistency about the thin film quality can always be improved. These obstacles make it hard to move the research forward from the current status. The author suggests the thin film fabrication process can be taken over by other advanced PVD technique, like magnetron sputtering. A more reliable deposition system can thus guarantee higher quality films and coatings fabrication.

2. Corrosion Properties

In the present study, it is found that the corrosion properties of the various silicides do not show significant difference compared to the substrate materials even though silica has formed. It is believed the sweep rate in the potentiodynamic polarisation tests suggested by the ASTM standard may still be too fast for the protective silica layers to build up, or the chemical environment is too aggressive. Therefore, it is proposed to keep the polarisation scanning rate only at or below their suggested level. For the same matter, it is proposed that the coated specimens could be exposed to an oxidising environment for a period of time or treated them in a more moderate environment to stimulate the passive film development prior to the aggressive corrosion test. The well-developed silica layer at the silicide top surface should have beneficial effect to the corrosion resistance improvement and the transition metal might have carried a role as a catalysis or inhibitor during the silica formation process.

The corrosion mechanism of individual silicides in each of the tested solution is always an interesting topic from electrochemistry point of view. Therefore, electrochemical impedance spectroscopy (EIS) measurement is proposed to carry out. Cyclic voltammetry is also proposed for the anodic dissolution study. Some attempts to apply cyclic voltammetry were done, but the preliminary restuls were not conclusive. Results from these silicide thin films can be compared with those published by Shein [60-64,70-75] acquired from bulk silicide materials, and a comparative study about the corrosion behaviour of the silicide materials in bulk and thin film form can be worked out.

3. Wet Tribological Properties

In the practical environment, materials usually suffer both corrosive attack and wear. Therefore, wet tribological sliding test is meaningful to be conducted and verify the practicability of the silicide thin films in a designed environment.

4. Advanced Coatings Investigation

In Section 2.2, the author has mentioned that the latest research activity in this area is about “smart self-repairing protective coatings”. If the silicide films are proved to work out, one way to upgrade their function could be achieved by introducing chemical inhibitors as a further means of “defence line”! Alternatively, multicomponent design could be another approach to reach the same goal.

References

[1] K.H. Lo, C.H. Shek, J.K.L. Lai, *Recent Developments in Stainless Steels*, Mater. Sci. Eng., R 65 (2009) 39 – 104.

[2] K.W. Wong, *Ageing Characteristics and Microstructural Studies of Duplex Stainless Steels*, Ph.D. Thesis, City University of Hong Kong, Hong Kong, 1997.

[3] P.L. Tam, *Fabrication and Corrosion Properties of Nickel Silicide Thin Films*, Licentiate Thesis, Chalmers University of Technology, Gothenburg, Sweden, 2009.

[4] U.R. Evans, *An Introduction to Metallic Corrosion* (3rd edition), Edward Arnold, 1981.

[5] R.W.K. Honeycombe, H.K.D.H. Bhadeshia, *Steels – Microstructure and Properties* (2nd edition), Butterworth-Heinemann, 1995.

[6] L.L. Shreir, R.A. Jarman, G.T. Burstein, *Corrosion* (3rd edition), Oxford, Butterworth-Heinemann, 1994.

[7] F. Falkenberg, *Initiation and Repassivation of Pits on Austenite Stainless Steels*, Ph.D. Thesis, Chalmers University of Technology, Gothenburg, Sweden, 2000.

[8] L. Wegrelius, *Passivation of Austenitic Stainless Steel*, Ph.D. Thesis, Chalmers University of Technology, Gothenburg, Sweden, 1995.

[9] B. Brox, *Anodic Dissolution and Passivation of Stainless Steels*, Ph.D. Thesis, Chalmers University of Technology, Gothenburg, Sweden, 1987.

[10] B.-O. Elfström, *The Passive State of Stainless Steels*, Ph.D. Thesis, Chalmers University of Technology, Gothenburg, Sweden, 1981.

[11] I. Olefjord, *Applications of ESCA in Materials Technology: Corrosion, Weld Embrittlement, and Battery Electrodes*, Ph.D. Thesis, Chalmers University of Technology, Gothenburg, Sweden, 1974.

[12] H. Asteman, *Water Vapour Induced Active Oxidation of Stainless Steel*, Ph.D. Thesis, Gothenburg University, Gothenburg, Sweden, 2002.

[13] J. Nockert, *Corrosion of Stainless Steel in Diesel Exhaust Gas After-Treatment Systems with Urea Injection*, Licentiate Thesis, Chalmers University of Technology, Gothenburg, Sweden, 2010.

[14] C. Pettersson, *High Temperature Corrosion of some Stainless Steels – The Influence of Water Vapour and Potassium-containing Salts*, Ph.D. Thesis, Chalmers University of Technology, Gothenburg, Sweden, 2009.

[15] J. Pettersson, *Alkali Induced High Temperature Corrosion of Stainless Steel – Experiences from Laboratory and Field*, Ph.D. Thesis, Chalmers University of Technology, Gothenburg, Sweden, 2008.

[16] F. Tholence, *High Temperature Corrosion of Cast Irons and Steels*, Ph.D. Thesis, Chalmers University of Technology, Gothenburg, Sweden, 2004.

[17] D.A. Jones, *Principles and Prevention of Corrosion* (2nd edition), Prentice Hall, 1996.

[18] M.P. Ryan, D.E. Williams, R.J. Chater, B.N. Hutton & D.S. McPhail, *Why Stainless Steel Corrodes*, Nature 415 (2002) 770 – 774.

[19] P. Liu, *Phase Analysis in Steel using Analytical Transmission Electron Microscopy*, Sandvik Materials Technology, Sweden, 2004.

[20] T. Burakowski, *Chapter 6 Coatings* in: *Surface Engineering of Metals: Principles, Equipments and Technology*, CRC Press LLC, Boca Raton, Florida, 1999.

[21] J.R. Davis (Editor), *Surface Engineering for Corrosions and Wear Resistance*, Maney Publishing, ASM International, Institute of Materials, Materials Park, Ohio, 2001.

[22] R. Asthana, A. Kumar, N.B. Dahotre, *Chapter 5 Coatings and Surface Engineering*, in: *Materials Processing and Manufacturing Science*, Elsevier Academic Press, Amsterdam, Boston, 2006, pp. 313 – 394.

[23] G. Heim, W. Schwenk, *Chapter 5 Coatings for Corrosion Protection*, in: W. Schwenk, W. Prinz (Editors), *Handbook of Cathodic Corrosion Protection* (3rd edition)*: Theory and Practices of Electrochemical Protection Processes*, Houston, Tex. Gulf Pub. Co. 1997.

[24] M. Stueber, H. Holleck, H. Leiste, K. Seemann, S. Ulrich, C. Ziebert, *Concepts for the Design of Advanced Nanoscale PVD Multilayer Protective Thin Films*, J. Alloy Compd. 483 (2009) 321 – 333.

[25] P.Eh. Hovsepian, W.-D. Münz, *Chapter 14 Synthesis, Structure, and Applications of Nanoscale Multilayer / Superlattice Structured PVD coatings*, in: A. Cavalieiro, J.Th.M. De Hosson (Editors), *Nanostructured Coatings*, Springer, New York, 2006.

[26] P.H. Mayrhofer, C. Mitterer, L. Hultman, H. Clemens, *Microstructural Design of Hard Coatings*, Prog. Mater. Sci. 51 (2006) 1032 – 1114.

[27] S.C. Tjong, H. Chen, *Nanocrystalline Materials and Coatings*, Mater. Sci. Eng., R 45 (2004) 1 – 88.

[28] O. Knotek, F. Löffler, G. Krämer, *Process and Advantage of Multicomponent and Multilayer PVD Coatings*, Surf. Coat. Technol. 59 (1993) 14 – 20.

[29] S. Vepřek, *The Search for Novel, Superhard Materials*, J. Vac. Sci. Technol. A 17 (1999) 2401 – 2420.

[30] T. Markley, S. Dligatch, A. Trinchi, T.H. Muster, A. Bendavid, P. Martin, D. Lau, A. Bradbury, S. Furman, I.S. Cole,

Multilayered Coatings: Tuneable Protection for Metals, Corros. Sci. 52 (2010) 3847 – 3850.
[31] F. Presuel-Moreno, M.A. Jakab, N. Tailleart, M. Goldman, J.R. Scully, *Corrosion-resistant Metallic Coatings*, Mater. Today 11 (2008) 14 – 23.
[32] D.V. Andreeva, D.G. Shchukin, *Smart Self-repairing Protective Coatings*, Mater. Today 11 (2008) 24- 30.
[33] M.A. Almomani, C.R. Aita, *Pitting Corrosion Protection of Stainless Steel by Sputter Deposited Hafnia, Alumina, and Hafnia-alumina Nanolaminate Films*, J. Vac. Sci. Technol. A 27 (2009) 449 – 455.
[34] A.A. Hermas, *Protection of Type 430 Stainless Steel against Pitting Corrosion by Ladder Conductive Polymer*, Prog. Org. Coat. 61 (2008) 95 – 102.
[35] A. Yağan, N. Özçiçek Pekmexz, A. Yıldız, *Poly(N-ethylaniline) Coatings on 304 Stainless Steel for Corrosion Protection in Aqueous HCl and NaCl Solutions*, Electrochim. Acta 53 (2008) 2474 – 2482.
[36] E. Hür, G. Bereket, Y. Şahin, *Corrosion Inhibition of Stainless Steel by Polyaniline, Poly(2-chloroaniline), and Poly(aniline-co-2-chloroaniline) in HCl*, Prog. Org. Coat. 57 (2006) 149 – 158.
[37] T. Tüken, *Polypyrrole Films on Stainless Steel*, Surf. Coat. Technol. 200 (2006) 4713 – 4719.
[38] S. Fujimoto, H. Hayashida, T. Shibata, *Extremely High Corrosion Resistance of Thin Film Stainless Steels Deposited by Ion Beam Sputtering*, Mater. Sci. Eng. A 267 (1999) 314 – 318.
[39] S. Bose, *High Temperature Coatings*, Elsevier Butterworth-Heinemann, Amsterdam, Boston, 2007.
[40] E. Fitzer, D. Kehr, *Carbon, Carbide and Silicide Coatings*, Thin Solid Films 39 (1976) 55 – 67.
[41] E. Fitzer, H.-J. Mäurer, W. Nowak, J. Schlichting, *Aluminium and Silicon Base Coatings for High Temperature Alloys – Process, Development and Comparison of Properties*, Thin Solid Films 64 (1979) 305 – 319.
[42] R. Mévrel, *State of the Art on High-temperature Corrosion-resistant Coatings*, Mater. Sci. Eng. A120 (1989) 13 – 24.
[43] H.W. Grünling, R Bauer, *The Role of Silicon in Corrosion-resistant High Temperature Coatings*, Thin Solid Films 95 (1982) 3 – 20.
[44] M. Bartur, M.-A. Nicolet, *Thermal Oxidation of Transition Metal Silicide on Si: Summary*, J. Electrochem. Soc. 131 (1982) 371 – 375.
[45] A.D. Chirkin, V.O. Lavrenko, V.M. Talash, *High-temperature and Electrochemical Oxidation of Transition Metal Silicides*, Powder Metall. Met. Ceram. 48 (2009) 330 – 345.
[46] V.M. Knyazheva, S.G. Babich, V.I. Kolotyrkin, V.B. Kozhevnikov, *Metal-like Compounds of Transition-metals – A New Class of Corrosion-resistant Materials and Protective Coatings*, Prot. Met. 27 (1991) 470 – 480.
[47] J. Emsley, *The Elements*, Oxford University Press, 1998.
[48] W.M. Hayes (Editor), *Handbook of Chemistry and Physics*, CRC Press, 91st edition, 2011.
[49] Solid State Technology® Online Magazine.
[50] R.F. Service, *Is Silicon's Reign Nearing its End?*, Science 323 (2009) 1000 – 1002.
[51] C.-H. Li, R. Warren, I. Olefjord, L. L'Estrade, *Silicides as Potential Structural Materials for High Temperature Application*, Internrapport, Chalmers University of Technology, Gothenburg, Sweden, 1992.
[52] D.-Q. Yi, *Structural Silicides – Processing, Microstructure and Toughening*, Ph.D. Thesis, Chalmers University of Technology, Gothenburg, Sweden, 1997.
[53] A.A. Sharif, A. Misra, J. Petrovic, T.E. Mitchell, *Alloying for $MoSi_2$ for Improved Mechanical Properties*, Intermetallics 9 (2001) 869 – 873.
[54] J.J. Petrovic, A.K. Vasudevan, *Key Developments in High Temperature Structural Silicides*, Mater. Sci. Eng. A 261 (1999) 1 – 5.
[55] K.S. Kumar, *Chapter 10 Silicides: Science, Technology and Applications*, in: J.H. Westbrook, R.L. Fleischer (Editors), *Structural Applications of Intermetallic Compounds*, John Wiley & Sons Inc., 2000.
[56] J. P. Gambino, E.G. Colgan, *Silicides*, Encyclopaedia of Applied Physics, 2004, pp. 201 – 248.
[57] R. Pretorius, *Prediction of Silicide Formation and Stability using Heats of Formation*, Thin Solid Films 290 – 291 (1996) 477 – 484.
[58] R. Pretorius, T.K. Marais, C.C. Theron, *Thin Film Compound Phase Formation Sequence: An Effective Heat of Formation Model*, Mater. Sci. Rep. 10 (1993) 1 – 83.
[59] F.P. Fehlner, M.J. Graham, *Chapter 6 Thin Oxide Film Formation on Metals*, in: P. Marcus (Editor), *Corrosion Mechanisms in Theory and Practice* (2nd edition, revised and expanded), Marcel Dekker Inc., New York, 2002, pp. 171 – 187.
[60] F.P. Fehlner, *Low-temperature Oxidation – The Role of Vitreous Oxides*, John Wiley & Sons, Inc., 1986.
[61] A.B. Shein, O.V. Kanaeva, *Anodic Dissolution of the (100) and (110) Faces of Iron Monosilicide in a Sulphuric Acid Electrolyte*, Russ. J. Electrochem. 36 (2000) 913 – 915.
[62] A.B. Shein, *Electrochemical Behaviour of Co_2Si in Acids*, Prot. Met. 36 (2000) 165 – 169.
[63] A.B. Shein, O.V. Kanaeva, *Anodic Dissolution of Cobalt Silicides in Sulphuric Acid Solutions*, Russ. J. Electrochem. 36 (2000) 1021 – 1025.
[64] A.B. Shein, O.V. Kanaeva, *Peculiarities of the Anodic Dissolution of a Powder NiSi Electrode*, Prot. Met. 37 (2001) 385 – 388.
[65] A.B. Shein, O.S. Ivanova, R.N. Minkh, *The Effect of Anions on the Anodic Dissolution of Nickel Silicide in Sulphate Electrolytes*, Prot. Met. 44 (2008) 32 – 38.

[66] S. Base, *Chapter 4 Oxidation*, in: *High Temperature Coatings*, Elsevier, Butterworth-Heinemann, 2007.
[67] M.A. Wells, R.J. Gilkes, R.W. Fitzpatrick, *Properties and Acid Dissolution of Metal-substituted Hematites*, Clay Clay Miner. 49 (2001) 60 – 72.
[68] W.D. Callister, Jr., *Materials Science and Engineering: An Introduction* (5th edition), John Wiley & Son. Inc. 2000.
[69] M. Pourbaix, *Thermodynamics and Corrosion*, Corros. Sci. 30 (1990) 963 – 988.
[70] I. Puigdomenech, *Make Equilibrium Diagrams Using Sophisticated Algorithms (MEDUSA)*, Royal Institute of Technology, Stockholm, Sweden, 2009 Version.
[71] A.B. Shein, E.N. Zubova, *Electrochemical Behaviour of Manganese Silicides in Sulphuric Acid Solution*, Prot. Met. 41 (2005) 234 – 242.
[72] A.B. Shein, E.N. Zubova, *Electrochemical Behaviour of Mn_5Si_3 and Mn_5Ge_3 in Sulphuric Acid Solutions*, Russ. J. Electrochem. 40 (2004) 222 – 227.
[73] A.B. Shein, *Effect of the Metal Component on Anodic Dissolvability of Iron, Cobalt, and Nickel Silicides*, Prot. Met. 37 (2001) 315 – 318.
[74] A.B. Shein, I.L. Rakityanskaya, S.F. Lomaeva, *Anodic Dissolution of Iron Silicides in Alkaline Electrolyte*, Prot. Met. 43 (2007) 54 – 58.
[75] A.B. Shein, I.L. Sergeeva, *Anodic Dissolution of Cobalt Silicides in Alkaline Electrolytes*, Prot. Met. 40 (2004) 562 – 565.
[76] A.B. Shein, I.L. Sergeeva, *Corrosion-electrochemical Behaviour of Nickel Monosilicide in Alkaline Electrolyte*, Prot. Met. 40 (2004) 556 – 561.
[77] I.L. Rakityanskaya, A.B. Shein, *Anodic Behaviour of Iron, Cobalt, and Nickel Silicides in Alkaline Electrolytes*, Russ. J. Electrochem. 42 (2006) 1208 – 1212.
[78] Z. Jiang, X. Dai, H. Middleton, *Effect of Silicon on Corrosion resistance of Ti-Si alloys*, Mater. Sci. Eng. B 176 (2011) 79 – 86.
[79] Y. Omurtag, M. Doruk, *Some Investigations of the Corrosion Characteristics of Fe-Si alloys*, Corros. Sci. 10 (1970) 225 – 231.
[80] L.X. Dong, H.M. Wang, *Microstructure and Corrosion Properties of Laser-melted Deposited Ti_2Ni_3Si/NiTi Intermetallic Alloy*, J. Alloys Compd. 465 (2008) 83 – 89.
[81] L. Yuan, H.M. Wang, *Corrosion Properties of a $Cr_{13}Ni_5Si_2$-based Metal Silicide Alloy*, Intermetallics 16 (2008) 1149 – 1155.
[82] L. Yuan, H.M. Wang, *Corrosion Behaviours of a γ-toughened $Cr_{13}Ni_5Si_2/Cr_3Ni_5Si_2$ Multi-phase Ternary Metal Silicide Alloy in NaCl Solution*, Electrochim. Acta 24 (2008) 421 – 429.
[83] L.X. Cai, H.M. Wang, C.M. Wang, *Corrosion Resistance of Laser Clad Cr-alloyed Ni_2Si/NiSi Intermetallic Coatings*, Surf. Coat. Technol. 182 (2004) 294 – 299.
[84] C.M. Wang, L.X. Cai, H.M. Wang, *Microstructure and Corrosion Resistance of Laser Clad Coating of Ni_2Si/Ni_3Si_2 Silicide Alloy*, Rare Metal. Mater. & Eng. 32 (2003) 197 – 200.
[85] H.M. Wang, C.M. Wang, L.X. Cai, *Wear and Corrosion Resistance of Laser Clad Ni_2Si/NiSi Composite Coatings*, Surf. Coat. Technol. 168 (2003) 202 – 208.
[86] H.W. Wang, G. Duan, *Wear and Corrosion Behaviour of Laser Clad Cr_3Si Reinforced Intermetallic Composite Coatings*, Intermetallics 11 (2003) 755 – 762.
[87] M. Popczyk, J. Kubisztal, A. Budniok, *Structure and Electrochemical Characterisation of Electrolytic Ni + Mo + Si Composite Coatings in an Alkaline Solution*, Electrochim. Acta 51 (2006) 6140 – 6144.
[88] M. Herranen, A. Delblanc Bauer, J.-O. Carlsson, R.F. Bunshah, *Corrosion Properties of Thin Molybdenum Silicide Films*, Surf. Coat. Technol. 96 (1997) 245 – 254.
[89] P.I. Igenatenko, A.A. Goncharov, S.S. Primin, *Structure and Properties of Thin Coatings Si_3N_4 and Ni_3Si*, Met. Phys. Adv. Tech. 18 (1999) 705 – 710.
[90] L.L. Stetsovskii, E.T. Shapovalov, L.A. Shvartsman, *Deposition of Nickel Silicide Coatings and their Electrochemical and Corrosion Properties*, Russ. Metall. 2 (1991) 183 – 186.
[91] G.F. Hays, PE, *Now is the Time*, World Corrosion Organisation, 2007: http://www.corrosion.org/
[92] C. Leygraf, *Chapter 15 Atmospheric Corrosion*, in: P. Marcus (Editor), *Corrosion Mechanism in Theory and Practice* (2nd edition), Marcel Dekker Inc., New York, 2002, pp. 529 – 562.
[93] D. Thierry, W. Sand, *Chapter16 Microbially Influenced Corrosion*, in: P. Marcus (Editor), *Corrosion Mechanism in Theory and Practice* (2nd edition), Marcel Dekker Inc., New York, 2002, pp. 563 – 604.
[94] R. Baboian (Editor), *Corrosion Tests and Standards – Application and Interpretation*, ASTM, USA, 1996.
[95] *CorrWare for Windows – Electrochemistry/Corrosion Software – Operating Manual Version 2.9*, Scribner Associates, Inc., 2002.
[96] A.J. Bard, R. Parsons, J. Jordan (Editors), *Standard Potentials in Aqueous Solution*, IUPAC, Dekker, 1985.
[97] C.R. Clayton, I. Olefjord, *Chapter 7 Passivity of Austenitic Stainless Steels*, in: P. Marcus (Editor), *Corrosion Mechanism in Theory and Practice* (2nd edition), Marcel Dekker Inc., New York, 2002, pp. 217 – 242.
[98] G.S. Frankel, N. Sridhar, *Understanding Localised Corrosion*, Mater. Today 11 (2008) 38 – 44.
[99] G.S. Frankel, *Pitting Corrosion of Metals – A Review of the Critical Factors*, J. Electrochem. Soc. 145 (1998) 2186 – 2198.
[100] H.-H. Stehblow, *Chapter 8 Mechanisms of Pitting Corrosion*, in: P. Marcus (Editor), *Corrosion Mechanism in Theory and*

Practice (2nd edition), Marcel Dekker Inc., New York, 2002, pp. 243 – 286.
[101] S.P. Murarka, *Codeposited Silicides in Very-large-scale Integration*, Thin Solid Films, 140 (1986) 35 – 50.
[102] C.J. Chen, J.C. Huang, H.S. Chou, Y.H. Lai, L.W. Chang, X.H. Du, J.P. Chu, T.J. Nieh, *On the Amorphous and Nanocrystalline Zr-Cu and Zr-Ti Co-sputtered Thin Films*, J. Alloys Compd. 483 (2009) 337 – 340.
[103] H. Inui, A. Fujii, T. Hashimoto, K. Tanaka, M. Yamaguchi, K. Ishizuka, *Defects Structures in $TaSi_2$ Thin Films Produced by Co-sputtering*, Acta Mater. 51 (2003) 2285 – 2296.
[104] S.M. Rossnagel, *Thin Film Deposition with Physical Vapor Deposition and Related Technologies*, J. Vac. Sci. Technol. A 21 (2003) S74 – S 87.
[105] H.R. Kaufman, J.J. Cuomo, M.E. Harper, *Critical Review: Technology and Applications of Broad-beam Ion Sources Used in Sputtering. Part I Ion Source Technology*, J. Vac. Sci. Technol. 21 (1982) 725 – 736.
[106] J.M.E. Harper, J.J. Cuomo, H.R. Kaufman, *Critical review: Technology and Applications of Broad-beam Ion Sources Used in Sputtering. Part II Applications*, J. Vac. Sci. Technol. 21 (1982) 737 – 756.
[107] J.A. Thornton, J.E. Greene, *Chapter 5 Sputter Deposition Processes*, in: R.F. Bunshah (Editor), *Handbook of Deposition Technologies for Films and Coatings – Science, Technology and Applications* (2nd edition), Noyes Publications, New Jersey, 1994, pp 275 – 345.
[108] C.J. Byrne, M. Eldrup, *Bulk Metallic Glasses*, Nature 321 (2008) 502 – 503.
[109] T.L. Cheung, *Mechanical and Surface Properties of Copper-based Bulk Metallic Glasses*, M.Phil. Thesis, City University of Hong Kong, Hong Kong, 2006.
[110] P.F. Gostin, A. Gebert, L. Schultz, *Comparison of the Corrosion of Bulk Amorphous Steel with Conventional Steel*, Corros. Sci. 52 (2010) 273 – 281.
[111] Y.-W. Wu, W.-C. Chiang, J. Chu, T.-G. Nieh, Y. Y. Kawamura, J.-K. Wu, *Corrosion resistance of Amorphous and Crystalline $Pd_{40}Ni_{40}P_{20}$ Alloys in Aqueous Solutions*, Mater. Lett. 60 (2006) 2416 – 2418.
[112] H. Ashassi-Sorkhabi, S.H. Rafizadeh , *Effect of Coating Time and Heat Treatment on Structures and Corrosion Characteristics of Electroless Ni-P Alloy Deposits*, Surf. Coat. Technol. 176 (2004) 318 -326.
[113] S.J. Pang, T. Zhang, K. Asami, A. Inoue, *Synthesis of Fe-Cr-Mo-C-B-P Bulk Metallic Glasses with High Corrosion Resistance*, Acta Mater. 50 (2002) 489 – 497.
[114] A.P. Wang, X.C. Chang, W.L. Wou, J.Q. Wang, *Corrosion Behavior of Ni-based Amorphous Alloys and their Crystalline Counterparts*, Corros. Sci. 49 (2007) 2628 – 2635.
[115] A.P. Wang, T. Zhang, J.Q. Wang, *Ni-based Fully Amorphous Metallic Coating with High Corrosion Resistance*, Phil. Mag. Lett. 86 (2006) 5 – 11.
[116] D. Zander, U. Köster, *Corrosion of Amorphous and Nanocrystalline Zr-based Alloys*, Mater. Sci. Eng. A 375 – 377 (2004) 53 – 59.
[117] J.F. Watts, J. Wolstenholme, *An Introduction to Surface Analysis by XPS and AES*, John Wiley & Sons Inc., 2003.
[118] I. Olefjord, *XPS – Quantitative and Quantitative aspects*, Proceedings in the Symposium of the Application of Surface Analysis Methods to Environmental/Material Interactions, The Electrochemical Society, Seattle, 1990.
[119] D. Briggs, M.P. Seah, *Practical Surface Analysis by Auger and X-ray Photoelectron Spectroscopy*, John Wiley & Sons. Inc., 1983.
[120] J. Finster, D. Schulze, F. Bechstedt, A. Meisel, *Interpretation of XPS Core Level Shifts and Structure of Thin Silicon Oxide Layers*, Surf. Sci. 152/153 (1985) 1063 – 1070.
[121] W. Heinke, A. Leyland, A. Matthews, G. Berg, C. Friedrich, E. Broszeit, *Evaluation of PVD Nitride Coatings Using Impact, Scratch and Rockwell-C Adhesion Tests*, Thin Solid Films 270 (1995) 431 – 438.
[122] N. Vidakis, A. Antoniadis, N. Bilalis, *The VDI 3198 Indentation Test Evaluation of a Reliable Quantitative Control for Layered Compounds*, J. Mater. Process. Technol. 143 – 144 (2003) 481 – 485.
[123] DD CEN/TS 1071-8:2004 standard: Advanced Technical Ceramic – Methods of Test for Ceramic Coatings: *Part 8 Rockwell Indentation Test for Evaluation of Adhesion*.
[124] M.L. Oyen, R.F. Cook, *A Practical Guide for Analysis of Nanoindentation Data*, J. Mech. Biomed. Mater. 2 (2009) 396 – 407.
[125] E. Le Bourhis, *Indentation Mechanics and its Application to Thin Film Characterization*, Vacuum 82 (2008) 1353 – 1359.
[126] A.C. Fischer-Cripps, *Review: Critical Review of Analysis and Interpretation of Nanoindentation Test Data*, Surf. Coat. Technol. 200 (2006) 4153 – 4165.
[127] J.L. Hay, G.M. Pharr, *Instrumented Indentation Testing*, in: ASM Handbook Vol. 08: Mechanical Testing and Evaluation, ASM International, 2000.
[128] J. Menčik, D. Munz, E. Qunadt, E.R. Wepelmann, *Determination of Elastic Modulus of Thin Layers using Nanoindentation*, J. Mater. Res. 12 (1997) 2475 – 2484.
[129] J. Musil, F. Kunc, H. Zeman, H. Polaková, *Relationships between Hardness, Young's Modulus and Elastic Recovery in Hard Nanocomposite Coatings*, Surf. Coat. Technol. 154 (2002) 304 – 313.
[130] W.D. France, Jr., *A Specimen Holder for Precise Electrochemical Polarisation Measurements on Metal Sheets and Foils*, J. Electrochem. Soc. 114 (1967) 818 - 819.
[131] ASTM International: G5 – 94 Standard, *Standard Reference Test Method for Making Potentiostatic and Potentiodynamic*

Anodic Polarisation Measurements, 2004.
[132] B. Cottis, *Corrosion Measurement Techniques* (PowerPoint), EChem for Corrosion Processes, 1997.
[133] D.G. Enos, L.L. Scribner, *The Potentiodynamic Polarisation Scan – Technical Report 33*, Solartron Instruments, 1997.
[134] D. Landolt, *Chapter 1 Introduction to Surface Reactions: Electrochemical Basis of Corrosion*, in: P. Marcus (Editor), *Corrosion Mechanism in Theory and Practice* (2nd edition), Marcel Dekker Inc., New York, 2002, pp. 1 – 18.
[135] A.J. Bard, L.R. Faulkner, *Electrochemical Methods – Fundamentals and Applications* (2nd edition), John Wiley & Sons. Inc, 2001.
[136] B.Y. Tsaur, S.S. Lau, J.W. Mayer, M.A. Nicolet, *Sequence of Phase Formation in Planar Metal-Si reaction couples*, Appl. Phys. Lett. 38 (1981) 922 – 924.
[137] U. Gösele, K.N. Tu, *Growth Kinetics of Planar Binary Diffusion Couples: "Thin-film case" versus "Bulk cases"*, J. Appl. Phys. 53 (1982) 3252 – 3261.
[138] License Agreement issued by Copyright Clearance Center between the thesis author and Elsevier for reusing the figures in the article in Thin Solid Films 290-291 (1996) 477 – 484 for author's thesis – Lic. No.: 27724160007210.
[139] T.B. Massalski (Editor), *Binary Alloy Phase Diagrams* (2nd edition), ASM International, Materials Park, Ohio, 1990.
[140] C.S. Fadley, *X-ray Photoelectron Spectroscopy: Progress and Perspective*, J. Electron. Spectrosc. 178-179 (2010) 2 – 32.
[141] K.M. Siegbahn, *Electron Spectroscopy for Atoms, Molecules and Condensed Matter*, Nobel Lecture in Physics, Stockholm, Sweden, 1981.
[142] *Technical Manual, 5500/5600 MultiTechnique – Installation, Calibration, Maintenance*, Perkin-Elmer, Physical Electronic Corporation, 1992.
[143] C.D. Wagner, *X-ray Photoelectron Spectroscopy*, Perkin Elmer, Physical Electronic Corp., 1979.
[144] G. Moretti, *Auger Parameter and Wagner Plot in the Characterization of Chemical States: Initial and Final State Effects*, J. Electron. Spectrosc. 76 (1995) 365 – 370.
[145] C.D. Wagner, *The Auger Parameter, its Utility and Advantages: A Review*, J. Electron Spectrosc. 47 (1988) 283 – 313.
[146] P. Dutta, *Grazing Incidence X-ray Diffraction*, Curr. Sci. India 78 (2000) 1478 – 1483.
[147] R.D. Tarey, R.S. Rastogi, K.L. Chopra, *Characterization of Thin Films by Glancing Incidence X-ray Diffraction*, The Rigaku Journal 4 (1987) 11 – 15.
[148] Powder Diffraction Files (PDF-2), International Crystallography Diffraction Database (ICDD), 2000.
[149] A.L. Patterson, *The Scherrer Formula for X-ray Particle Size Determination*, Phys. Rev. 56 (1939) 978 – 982.
[150] *LEO 1550 Scanning Electron Microscope*, Microfabrication Laboratory, University of California at Berkeley: http://microlab.berkeley.edu/labmanual/chap8/leo.pdf
[151] *Welcome to the World of Scanning Electron Microscope*, Materials Science and Engineering Department, Iowa State University: http://mse.iastate.edu/microscopy/home.html
[152] P.W. Shum, *Structural Characterisation and Mechanical Properties of Industrial PVD-TiAlN Coatings*, Ph.D. Thesis, City University of Hong Kong, Hong Kong, 2005.
[153] ASTM G133-05 Standard: *Standard Test Method for Linearly Reciprocating Ball-on-flat Sliding Wear*, 2010.
[154] *UBi 1® Users Manual,* Hysitron Inc., 2004.
[155] BS EN ISO 14577 Standard: *Metallic Materials – Instrumented Indentation Test for Hardness and Materials Parameters*, Part 1 – 3, 2002.
[156] BS 1134-1: 1988: *Assessment of Surface Texture – Part 1: Methods and instrumentation*.
[157] *RST Plus system – Operator's Guide and Technical Reference Manual*, WYKO™ Corporation, 1995.
[158] Taylor-Hobson Inc. Company homepage: www.taylor-hobson.com
[159] G. Binnig, C.F. Quate, Ch. Gerber, *Atomic Force Microscope*, Phys. Rev. Lett. 56 (1986) 930 – 933.
[160] Y. Gan, *Atomic and Subnanometer Resolution in Ambient Conditions by Atomic Force Microscopy,* Surf. Sci. Rep. 64 (2009) 99 – 121.

Appendix A

Electrochemical Interface: Potentiostat

Potentiodynamic polarisation measurement is conducted by using a potentiostat together with a three-electrode electrochemical cell as shown in Figure A.1. To sum up briefly, the three electrode setup is working in two pairs to measure the current passing through and potential change in the working electrode (WE) during polarisation process. To achieve that, the working and the counter (or auxiliary) electrodes are working in pair (WE-CE) for current measurement while the other pair of WE and reference electrode (RE) is measuring the change of potential. For the top layer thin film corrosion properties evaluation, a special specimen holder based on Stern-Makrides [130] design is made to ensure only the uppermost area is exposed to the solution. Since the chloride-containing solution is chosen to be the testing environment, Ag/AgCl reference electrode is selected. For the choice of corrosive environment, we have thought about hydrochloric acid is the aggressive environment for stainless steel materials. Later on, we have also considered that the passivity of stainless steels in pure acidic environment is also important in this study. Therefore, sulphuric acid is chosen in the later part of the research. In practice, before all polarisation experiments, deaeration of the solution was carried out by purging dry inert gas (e.g. N_2) into the solution to reduce the dissolved oxygen content. The whole electrochemical setup was then introduced into the solution. After immersing the cell into the solution for more than an hour, the open circuit potential (E_{OCP}) was acquired at the equilibrium condition. Polarisation scanning was then started from a potential more negative to the E_{OCP} and sweeping to the positive potential at a rate of + 0.1667 mV/s, according to the ASTM standard [131], or below 1.0 mV/s as recommended by Cottis [132].

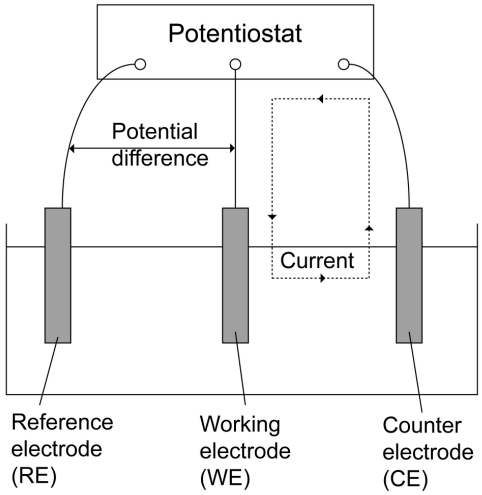

Figure A.1 The three-electrode electrochemical cell set up (Drawing based on [133]).

Electrochemistry about the Polarisation Diagram

The results of polarisation scan are presented in a polarisation diagram as introduced in Section 3.1. Though this diagram can present the electrochemical properties of a material in a chosen environment in a simple illustration, fundamental knowledge about electrochemistry is required to get a better understanding about the curves. Therefore, the thermodynamics and kinetics about the chemical reactions in an electrochemical process are briefly introduced here.

Electrochemical Thermodynamics [17,134]

In material science point of view, every material in a given state will have a characteristic value of *Gibb's free energy* (G) (unit: Joule, J). Change of a material state means the change of G, i.e. ΔG. In an electrochemical reaction, a material changes from one chemical state to another can be mathematically expressed as:

$$\Delta G = -n \cdot F \cdot E \quad \ldots \text{(A1)}$$

where n is the number of electron transfer in a chemical reaction, F is the Faraday's constant (96485 $C \cdot mol^{-1}$) and E is the electrochemical potential (unit: V). In principle, this energy change provides a driving force for a chemical reaction. Provided that ΔG is less than 0, the chemical reaction will be spontaneous. While the occurrence of a reaction can be predicted by this idea, the actual E is changing when the reaction proceeds. This is because the concentrations of the reactants and products are changing continuously. Therefore, by taking concentration into account, *Nernst equation* [Equation (A3)] is applied to monitor the change of electrode potential in the reacting environment of a specific reaction. For example, for a chemical reaction of J:

$$xJ^{n+} + ne^- \rightarrow xJ \quad \ldots \text{(A2)}$$

$$E = E^0 - \frac{R \cdot T}{n \cdot F} \ln \frac{[J]^x}{[J^{n+}]^x} \quad \ldots \text{(A3)}$$

where E^0 is the standard potential of a half-cell reaction of M, R is the universal molar gas constant (8.314 $J \cdot mol^{-1} \cdot K^{-1}$), T is the temperature in Kelvin (unit: K), [J] and $[J^{n+}]$ are the concentrations of J in metallic state and ionic state respectively (unit: molar, M), the superscripts x is the corresponding number of the reductants and oxidants that take part in a half-cell reaction. Meanwhile, the reaction in an electrochemical measurement is never a single event but involves at least an oxidation-reduction pair, or commonly called as "redox" pair, for electron-charge transfer interactions among 2 or more elements, compounds or molecules. Thereby, the measured potentials of the electrochemical characteristics in the experiments are never at the exact potential as they are expected in the standard potential. The experimental results are consequently explained by *the mixed potential theory*. An example given here in Figure A.2 is the E_{corr} determination in a polarisation measurement.

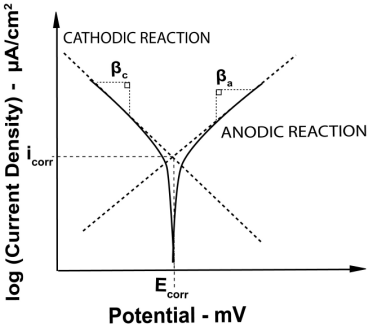

Figure A.2 Tafel slope calculation (Drawing based on [133]).

Assuming that the measurement was run from a low potential to a high potential just beyond the corrosion potential (E_{corr}), we can define the curve located at the lower potential than E_{corr} to be a sign of the cathodic-dominant path and the curve at higher potential as the anodic-dominant path. Thereby, E_{corr} is defined as the potential at which both anodic and cathodic reactions proceed at the same rate, but in opposite direction (i.e. one is donating electrons and the other is receiving electrons), resulting in basically the measured is being zero. From the diagram as in Figure A.2, the corrosion current density (i_{corr}) can be extracted.

Electrochemical Kinetics [135]

Note that thermodynamics is incapable to estimate the reaction rates. Therefore, potential alone is insufficient to tell the chemical kinetics. In the polarisation diagram, the current density (i, $\mu A \cdot cm^{-2}$) does. A higher current density indicates a faster reaction rate and vice versa. The measured current density, again, is contributed by a redox pair, and therefore, interpreted as follows:

At stationary conditions at corrosion current density (i_{corr}), current densities of anodic ($i_{anod.}$) and cathodic ($i_{anod.}$) reactions are of equal magnitude and the reaction directions are opposing to each other. Each reaction has the same kinetic as expressed in Equation (A5-a) and (A5-b):

$$i_{corr.} = |i_{cath.}| = |i_{anod.}| \quad \ldots \text{(A4)}$$

$$i_{cath.} = k_{cath.} \cdot \exp\left(-\frac{\Delta G_{cath.}}{RT}\right) \quad \ldots \text{(A5-a)} \quad \text{and} \quad i_{anod.} = k_{anod.} \cdot \exp\left(-\frac{\Delta G_{anod.}}{RT}\right) \quad \ldots \text{(A5-b)}$$

in which k is the reaction rate ($mol \cdot cm^{-2} \cdot s^{-1}$).

When an overpotential (η) is applied, the balance is disrupted and this external driving force is governing the final reaction rate by speeding up the reaction rate is given direction through:

$$\eta = E - E_{corr.} \quad \ldots \text{(A6)}$$

$$\eta = \beta \cdot \log\frac{i}{i_0} \quad \ldots \text{(A7) in which} \quad \beta = \frac{R \cdot T \cdot \ln(10)}{\alpha \cdot n \cdot F} \quad \ldots \text{(A8)}$$

where i_0 is the exchange current density of a specific material at a standard condition and α is the fraction of η taken by the anodic (during anodic overpotential) or cathodic (during cathodic overpotential) reaction during the polarisation process.

At cathodic overpotential (η_c, i.e. $E < E_{corr}$), with the supplying electrons from the external circuit, the energy barrier of the cathodic process reduces. Therefore, the reduction (or discharge) process becomes easier while the oxidation (or ionisation) process becomes harder. Mathematically:

$$i_{cath.} > i_{anod.} \quad \ldots \text{(A9)}$$

$$i_{cath.} = k'_{cath.} \cdot \exp\left(-\frac{\Delta G_{cath.} - \alpha \cdot n \cdot F \cdot \eta_c}{R \cdot T}\right) \quad \ldots \text{(A10-a)} \qquad \text{and} \quad i_{anod.} = k'_{anod.} \cdot \exp\left(-\frac{\Delta G_{anod.} - (1-\alpha) \cdot n \cdot F \cdot \eta_c}{R \cdot T}\right) \ldots \text{(A10-b)}$$

The resulting current density will be cathodically driven and expressed as follow:

$$i_{app.,c} = i_{cath.} - i_{anod.} \quad \ldots \text{(A11)}$$

$$i_{app.,c} = i_0 \cdot \left\{\exp\left[-\frac{\alpha \cdot n \cdot F \cdot \eta_c}{R \cdot T}\right] - \exp\left[-\frac{(1-\alpha) \cdot n \cdot F \cdot \eta_c}{R \cdot T}\right]\right\} \quad \ldots \text{(A12)}$$

On the other hand, at anodic overpotential (η_a, i.e. $E > E_{corr}$), electrons are extracted out by the external circuit, the energy barrier of the anodic process reduces and thus the oxidation process becomes easier while the reduction process becomes harder. Mathematically, the situation becomes:

$$i_{anod.} > i_{cath.} \quad \ldots \text{(A13)}$$

$$i_{anod.} = k'_{anod.} \cdot \exp\left(-\frac{\Delta G_{anod.} - \alpha \cdot n \cdot F \cdot \eta_a}{R \cdot T}\right) \quad \ldots \text{(A14-a)} \qquad \text{and} \quad i_{cath.} = k'_{cath.} \cdot \exp\left(-\frac{\Delta G_{cath.} - (1-\alpha) \cdot n \cdot F \cdot \eta_a}{R \cdot T}\right) \quad \ldots \text{(A14-b)}$$

The resulting current density will become anodically driven and expressed as:

$$i_{appl.,a} = i_{anod.} - i_{cath.} \quad \ldots \text{(A15)}$$

$$i_{appl.,a} = i_0 \cdot \left\{\exp\left[-\frac{\alpha \cdot n \cdot F \cdot \eta_a}{R \cdot T}\right] - \exp\left[-\frac{(1-\alpha) \cdot n \cdot F \cdot \eta_a}{R \cdot T}\right]\right\} \quad \ldots \text{(A16)}$$

Corrosion Rate Assessment

Corrosion rate ($r_{corr.}$) can be extracted from the polarisation curve by making use of the corrosion current density (i_{corr}) and Faraday's law. For engineering purpose, the corrosion rate can be defined as shown:

$$r_{corr.} = \frac{i_{corr} \cdot M}{n \cdot F} = \frac{m}{t \cdot A}$$ (mass per unit area per unit time, e.g. $g \cdot cm^{-2} \cdot s^{-1}$) … (A17), or

$$d_{corr.} = \frac{i_{corr} \cdot M}{n \cdot F \cdot \rho} = \frac{m}{t}$$ (penetrating depth per unit time, e.g. $nm \cdot s^{-1}$) … (A18)

where M is the molar mass ($g \cdot mol^{-1}$) of the tested specimen. In alloy measurements, M can be replaced by equivalent weight ($W_{eq.}$) as defined in the following expression:

$$W_{eq.} = \left(\sum_i \frac{f_i \cdot n_i}{M_i} \right)^{-1}$$ … (A19)

where f is the atomic fraction and n is the valence of each component. By this means, the experimental results can correlate with the engineering units [17,133].

Table A.1 The summary of the standard potentials of the electrochemical reactions of the transition metals and silicon in acid solution [96]

Element	Change of the oxidation state and the corresponding potential (in V)
Si	SiO_2 – *(-0.90)* – Si
Ti	TiO_2 – *(-0.56)* – Ti_2O_3 – *(-1.23)* – TiO – *(-1.31)* – Ti
Cr	Cr(VI) – *(+0.55)* – Cr(V) – *(+1.34)* – Cr(IV) – *(+2.10)* – Cr^{3+} – *(+0.42)* – Cr^{2+} – *(-0.90)* – Cr
Fe	Fe^{3+} – *(+0.771)* – Fe^{2+} – *(-0.44)* – Fe
Ni	NiO_4^{2-} – *(+1.8)* – NiO_2 – *(+1.593)* – Ni^{2+} – *(+0.257)* – Ni

Appendix B

Effective Heat of Formation (EHF) Model for Phase Prediction

In metal-silicide thin film preparation for microelectronic devices, the knowledge about the initial formation of silicide phase and the phase formation sequence in each system is important from both practical and research point of view. Probably, the first rule for predicting phase formation stated: "the first compound nucleated in planar binary reaction couples is the most stable congruently melting compound adjacent to the lowest temperature eutectic on the bulk equilibrium phase diagram [136]." Later on, this concept was extended by adding: "The second phase formed is the compound with the smallest ΔT that exists in the phase diagram between the composition of the first phase and the unreacted elements [136]." In addition, it has been predicted that after the first compound phase has formed, this phase must exceed a critical thickness before a second compound phase may form and growth simultaneously with the first one [137]. Based on those above concepts, Pretorius' et al [57,58] proposed a novel way of phase prediction by simply making use of thermodynamic data and the model is called the effective heat of formation (EHF) model. While considering the thermodynamic approach, the driving force for a process to take place is given by the change in the Gibbs free energy (ΔG^o) and expressed as:

$$\Delta G^o = \Delta H^o - T \cdot \Delta S^o \quad \ldots \text{(B1)}$$

where ΔH^o is the change in enthalpy during the reaction at temperature T and ΔS^o the change in entropy. However, the change in enthalpy is much more significant than the change in entropy during solid state formation of ordered compounds. Therefore, the contribution from the entropy is usually negligible and ΔH^o alone is a good measure of the change in free energy ΔG^o. This model by Pretorius is then defined to assess an effective heat of formation ΔH´ which depends on the available concentration of the reacting atomic species at the growth interface, given by:

$$\Delta H' = \Delta H^\circ \times \frac{\text{Effect Concentration of Limiting Element}}{\text{Compound Concentration of Limiting Element}} \qquad \ldots \text{(B2)}$$

According to Pretorius, the first formed phase should fulfil the following criteria:

1. it must be a congruent phase,
2. the phase should have the lowest effect heat of formation(ΔH´) level.
3. the phase formation sequence can be evaluated by comparing the ΔH´ level among different phases, non-congruent phase can form after the first phase is developed provided that the temperature difference between the liquidus curve and the peritectic/peritectoid point is very small.

Figure B.1 and B.2 demonstrates the application of EHF model to predict the silicide formation in our transition metal silicide analyses performed in Paper 2 (Table 8). Please note that the silicide synthesized from co-sputtering here is different from the metal-silicon interface reaction in Pretorius' model. The effective concentration of the limiting element can be the exact composition of the as-deposited mixture/compound instead of the liquidus minimum as proposed in the original model. The model, still, correctly predict the formation of congruent $TiSi_2$ phase from $Ti_{0.40}Si_{0.60}$, the non-congruent β-$FeSi_2$ and $NiSi_2$ phases from $Fe_{0.40}Si_{0.60}$ and $Ni_{0.20}Si_{0.75}$. The formation of the latter two phases is owing to their small difference of ΔH´ from the congruent FeSi and NiSi (i.e. slightly negative at that specific composition), respectively. For the mixture of CrSi2 and CrSi in the Cr-Si system, the model, however, has failed to explain this outcome. It is assumed that such result is the consequence of CrSi2 decomposition during the high temperature treatment.

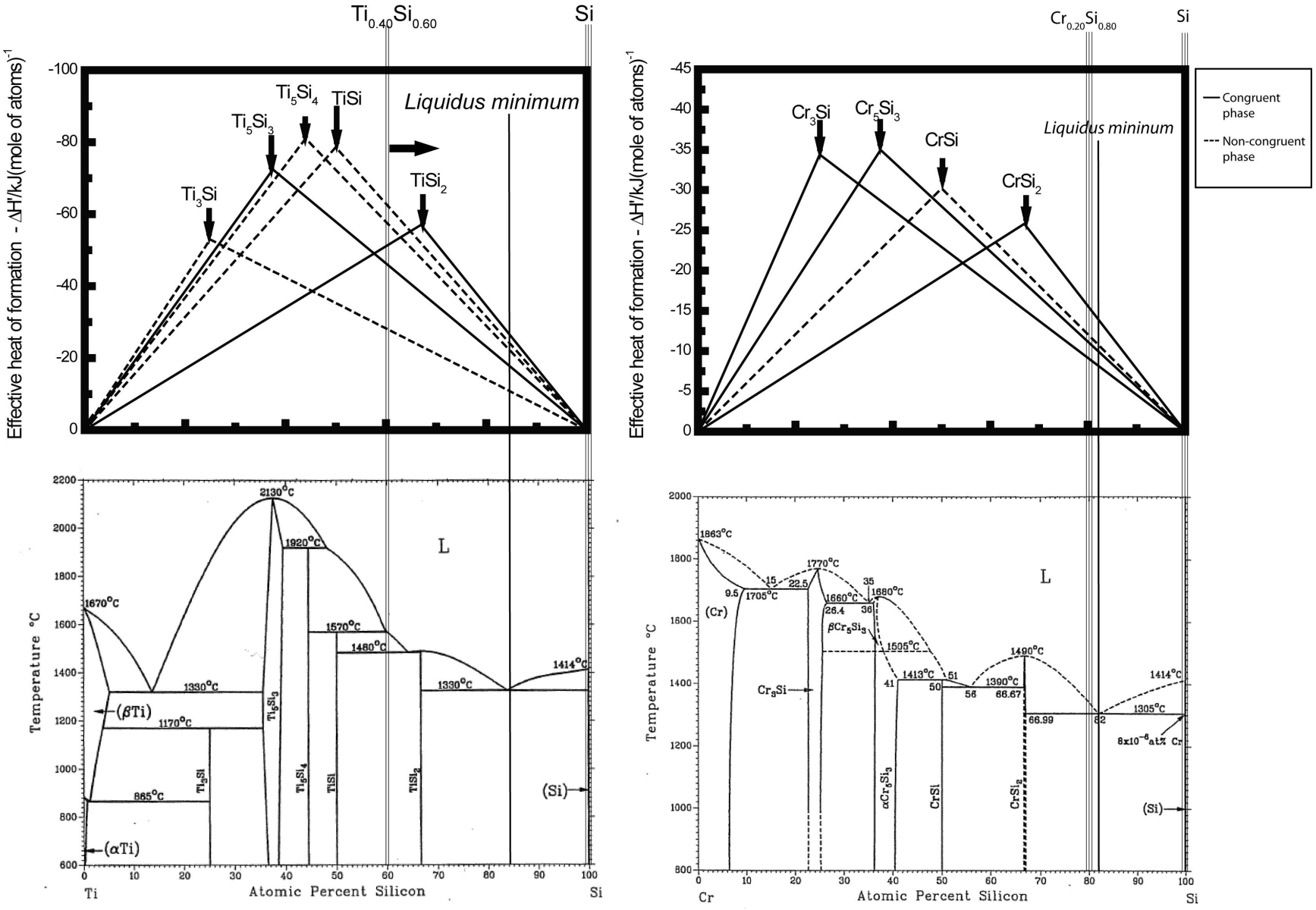

Figure B.1 The EHF diagram (top) and phase diagram (bottom) for the (a) Ti-Si and (b) Cr-Si systems [57,58,138,139].

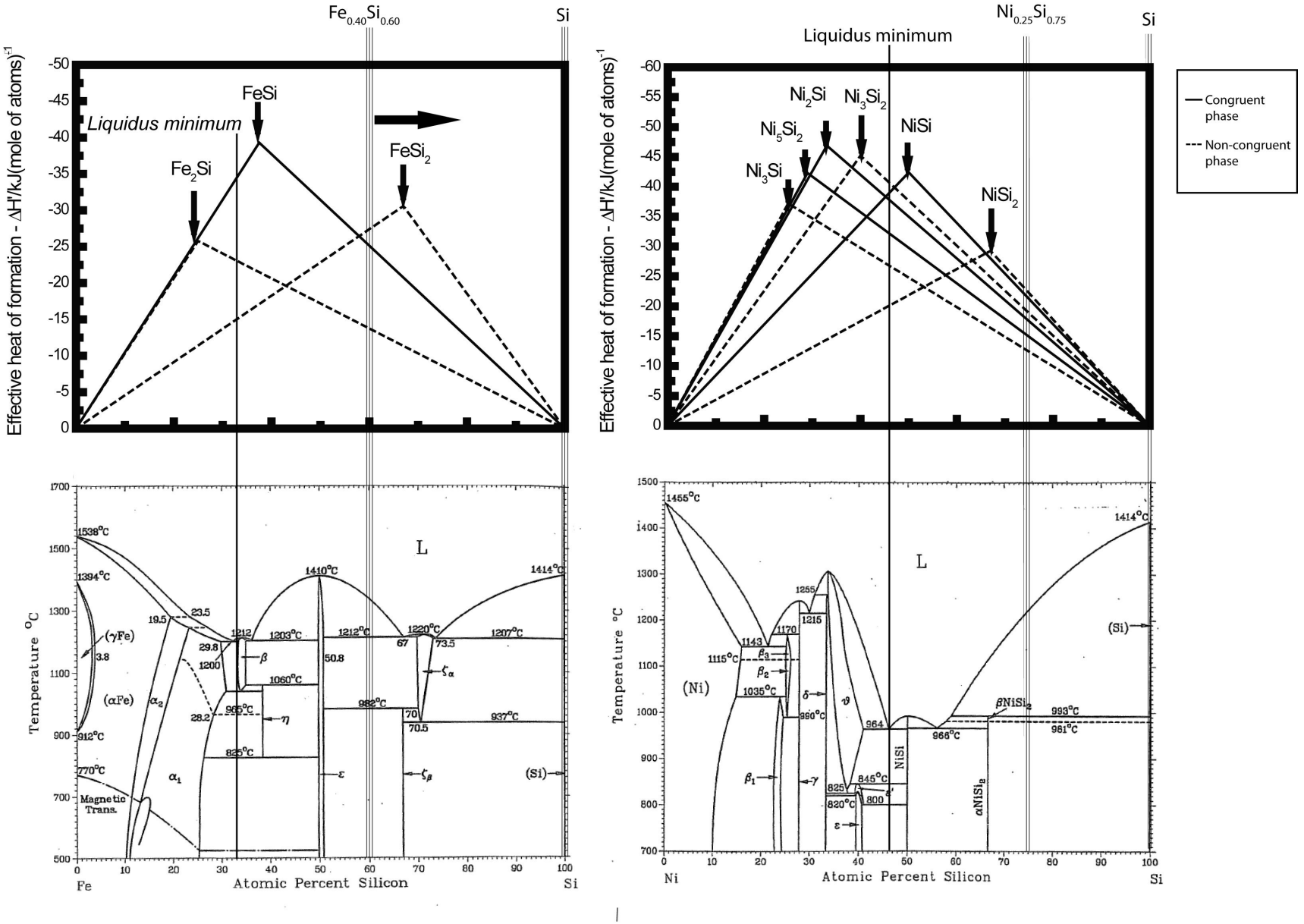

Figure B.2 The EHF diagram (top) and phase diagram (bottom) for the (a) Fe-Si and (b) Ni-Si systems [57,58,138,139].

Appendix C

X-ray Characterisation Instruments: X-ray Photoelectron Spectrometer (XPS) and X-ray Diffractometer (XRD)

Surface sensitive X-ray instruments including X-ray photoelectron spectrometer (XPS) and X-ray diffractometer (XRD) carried the major role in the surface characterisation work in this research. Compositional, chemical as well as structural characteristics of the coated silicides can be analysed by the individual techniques.

X-ray Generation

In principle, the generation of X-ray is the result of high energetic electron bombardments, which is emitted from hot tungsten (W) filaments, on the anode materials under a high tension of voltage in an enclosed high vacuum device [117]. The power of X-ray emission depends on the power applied on the filament. For the X-ray source in the XPS used (PHI 5500), the filament is set operating at 350 W (i.e. 25 mA, 14 kV); while for the X-ray tube equipped with a Cr anode in XRD, the operating power is set at 1400 W (i.e. 40 mA, 35 kV). In XPS, the choice of source depends on the energy level of the X-ray and the energy resolution of the X-ray energy line (i.e. full-width a half maximum – FWHM). Usually, the binding energy ranges from 0 to about 1000 eV and then 1253.6 or 1486.6 eV generated from the most commonly used Mg or Al sources are wide enough to provide sufficient information for most of the elements while the FWHMs are less than 1.0 eV. The choice of anode in XRD is sample dependent, for example, Cr anode is chosen in our laboratory because it can avoid the fluorescing radiation from the Fe-based materials, the most frequently measured type of material, otherwise induced by the commonly used CuKα source. The long wavelength of CrKα radiation (λ = 2.2897 Å), indeed, is useful for large unit cells measurement.

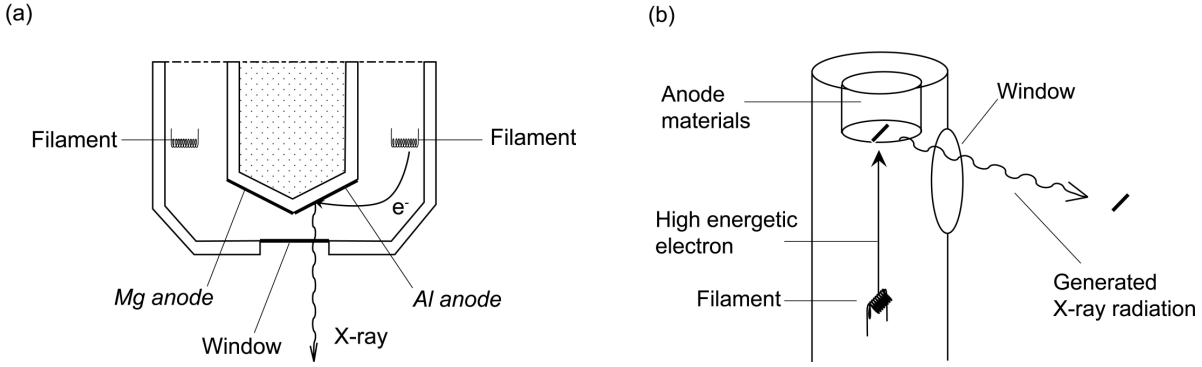

Figure C.1 X-ray generation in (a) X-ray source in XPS (b) X-ray tube in XRD (Author's illustration).

X-ray Photoelectron Spectroscopy (XPS)

The photoelectric effect by X-rays was discovered by Heinrich Hertz in 1887 and was explained by Albert Einstein in 1905 [140]. The usage of this physical phenomenon as a practical analytical instrument was brought up almost a hundred years later by Kai Siegbahn in 1970 [141], right after the golden age of vacuum technology in the 1960s. The *X-ray photoelectron spectroscopy (XPS)*, or the *electron spectroscopy for chemical analysis (ESCA)* coined by Siegbahn, is one of the most important materials characterisation tools in nowadays surface science research. The main parts of an XPS instrument consist of an X-ray source, a sample manipulator, and an electron energy analyser (Figure C.2). When a monochromatic X-ray beam is illuminated on the sample surface, photoionisation occurs as illustrated in Figure C.3 and expressed in the formula:

$E_{b,PE} = h\nu - E_{k,PE} - \varphi_{spec.}$ … (C1)

where hν stands for the energy of the X-ray photons, $E_{b,PE}$ is the binding energy of the photoelectron to the atomic nucleus, $E_{k,PE}$ is the kinetic energy of the emitted photoelectron and φ_{spec} is the work-function of the spectrometer. The work-function (φ) is basically the energy difference between the vacuum and Fermi levels (E_F) for the specific case considered. The medium to low-energy emitted electrons are then collected and counted in the electron energy analyser.

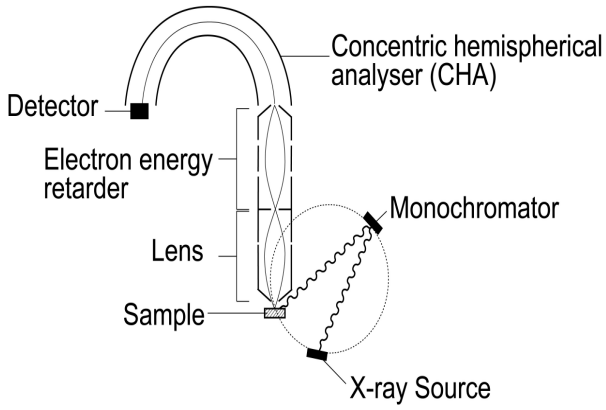

Figure C.2 Illustration of an XPS instrument (From [118]).

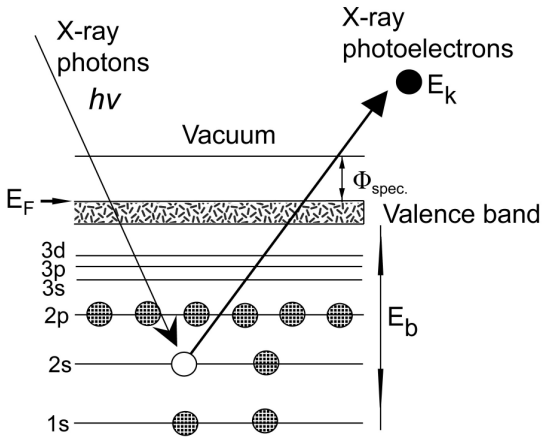

Figure C.3 Schematic diagram of a photoelectron emission process (Drawing based on [117]).

A plot of photoelectron intensity against binding energy that contains both photoelectron and Auger electron peaks is then generated (see Figure 15; Note: Auger electrons that are generated due to the de-excitation process can also be found in an XPS spectrum provided that their kinetic energies are within the possible range of analysis). The XPS spectrum obtained provides the basis for the abundance of surface specific information such as chemical states of elements present, their surface composition, thin film thicknesses and also the spatial distribution of compounds on and different materials on at least micrometre scale in lateral size [118,119,142].

Chemical composition can be characterised by making use of the peak height intensity or peak area measure of the characteristic peaks (I) of the individual composing elements. The atomic composition ($C_{at.}$) of each element can in the simplest approach be evaluated through the calculation of intensity ratio by putting atomic sensitivity factor (S) into consideration [142]. The equation then applied is:

$$C_{at.} = \frac{I/S}{\sum_n (I_n / S_n)} \qquad \text{… (C2)}$$

Provided that the analysed volume of material in the surface is homogeneous, this approach is applicable. Would there, however, be a more complicated morphology of thin surface products so that the analysed material volume covers both bulk and thin products, more advanced quantification approaches must be applied as further discussed below.

The information depth (or sampling depth) (d) is correlated to the photoelectron attenuation length (λ), which in turn depends on the kinetic energy of the emitted photoelectron (E) and the material being analysed (a). Photoelectron attenuation lengths are generally in the range of 1 – 3 nm, and can be expressed in the following semi-empirical equations [117-119]:

For metallic materials: $\lambda_{met} = \frac{538 \cdot a}{E^2} + 0.41 \cdot a^{3/2} \cdot E^{1/2}$ … (C3)

For inorganic materials: $\lambda_{inorg} = \frac{2170 \cdot a}{E^2} + 0.72 \cdot a^{3/2} \cdot E^{1/2}$ … (C4)

in which $a = \left[\frac{1}{D \cdot n_A \cdot N}\right]^{1/3} \cdot 10^7$ and D is the molecular density, $D = \frac{\rho}{M}$ (mol·cm^{-3}), n_A is the number of atoms in the molecule and N is the Avogadro's number. Table C.1 lists the attenuation lengths derived for the materials studied along with their physical data and details about their characteristic XPS peaks.

Table C.1 The summary of attenuation length evaluation of a Ni-Si system

Thin film system	Molar mass (g·mol^{-1})	Density (g·cm^{-3})	Molecular density (mol·cm^{-3})	Binding energy position of Ni2p$_{3/2}$ peak (eV)	Corresponding kinetic energy (eV)	Binding energy position of Si2p peak (eV)	Corresponding kinetic energy (eV)	N	a	λ_{Ni} (nm)	λ_{Si} (nm)
Ni	58.7	8.91	0.152	852.8	633.2			1	0.2219	1.08	
Ni_2Si	145.5	7.30	0.050	853.3	632.7	99.6	1386.4	3	0.2226	1.90	2.82
NiSi	86.8	5.98	0.069	853.8	632.1	99.6	1386.4	2	0.2293	1.99	2.94
$NiSi_2$	114.9	4.80	0.042	854.5	631.5	100.0	1386.0	3	0.2366	2.08	3.09
Si	28.1	2.33	0.083			99.4	1386.6	1	0.2716		3.79
SiO_2	60.1	2.65	0.044			103.8	1382.2	3	0.2324		3.00

* Monochromatic Al Kα source is used in PHI 5500 XPS characterisation ($h\nu$ = 1486.6 eV) [142].

Based on the approximate attenuation length, the information depth of a particular chemical state can be analysed by the Beer-Lambert Law [117]:

$I = I_0 \cdot \exp(-d / \lambda \cdot \sin\theta)$ … (C5)

and the approximate maximum information depth, i.e. a depth from which 95 % of all generated photoelectrons can reach the surface, is expected to be [117,118]:

$d_{\max} = 3 \cdot \lambda \cdot \sin\theta$ … (C6)

By varying the take-off angle (θ), the attenuation length will change and the information depth, of course, will vary. Therefore, through changing the take-off angle, composition at different depth of the top layer can be examined. The analysing technique of such type in XPS is called angle-resolved XPS (ARXPS). Surface composition and depth profile at the uppermost layer can thus be evaluated. For example, consider a silicon oxidation process on a silicon wafer. The only possible phases in the system are Si and SiO_2 only. By analysing the Si 2p peak covering both the elemental state and the oxidised state of silicon at different take-off angle, the thickness of the uppermost silica (SiO_2) layer can be calculated.

Photoelectron from the uppermost SiO_2: $I_{SiO_2} = I^{\infty}_{SiO_2} \cdot \left[1 - \exp\left(-\frac{d_{SiO_2}}{\lambda_{Si} \cdot \sin\theta}\right)\right]$ … (C7)

Photoelectron from the underlying Si: $I_{Si} = I_{Si}^{\infty} \cdot \exp\left(-\frac{d_{SiO_2}}{\lambda_{Si} \cdot \sin\theta} \right)$ … (C8)

Thickness of the oxide layer: $d_{SiO_2} = \lambda_{Si} \cdot \sin\theta \cdot \ln\left[\frac{I_{SiO_2} / I_{Si}}{I_{SiO_2}^{\infty} / I_{Si}^{\infty}} + 1 \right]$ … (C9)

In laboratory used for the present study, there is a PHI 5500 XPS instrument equipped with monochromatic AlKα X-ray source (E = 1486.6 eV) [142,143]. In overall compositional analysis performed, survey spectra were acquired at 93.5 eV pass energy and 0.4 eV/step scan rate. In chemical state analysis, higher resolution core-level spectra for individual element were acquired at 23.5 eV pass energy with 0.1 eV/step scan rate. In Si 2p analysis, even higher resolution can be achieved to distinguish Si $2p_{3/2}$ and $2p_{1/2}$ orbital at 5.85 eV pass energy with 0.05 eV/step. All spectra were acquired at a take-off angle of 45º. This angle corresponds to the sample being horizontally positioned during the analysis. Variation of the take-off angle at 30º, 45º and 60º is possible to generate non-destructive angle-resolved analysis for the uppermost oxide layer formed after polarisation tests.

Chemical State and Chemical Shift

In principle, the binding energy (BE) level in the XPS measurement is an integrated result of the photoelectron emission and X-ray excited Auger electron emission processes and involves the initial-state and final-state effects. The initial-state effects exist after the photoelectron emission but prior to X-ray excited Auger electron emission and they include factors such as ionicity (i.e. charge transfer), valence orbital transformation and valence electron configurations. During the photoelectron emission process, an electron from a specific electronic shell at the core level is emitted out and this leads to the binding energy strengthening between the remaining core-level electrons and the nucleus. Mathematically, these effects can be summarised in the following equation:

$$E_{b,PE} = E_{b,PE}^{0} + k \cdot q + V_M \quad \text{… (C10)}$$

where $E_{b,PE}$ is the binding energy of a core-level photoelectron emitted out from an atom, $E_{b,PE}^{0}$ is the binding energy of that electron before emitted out from the atom (i.e. an energy reference and a physical constant), V_M is the Madelung potential (i.e. the polarisation energy of an atom to the surroundings atoms), q is the valence charge of an atom and k is the change in core potential resulting from a removal of a photoelectron.

The final-state effects occur following the X-ray excited Auger electron emission. The system adjusts its orbital to a lower binding energy level, producing the relaxation of the core holes that are induced during photoelectron emission process. This relaxation energy consists of an intra-atomic contribution (R^{ia}) – the contraction energy of the outer electron change toward the inner core hole – and an extra-atomic contribution (R^{ea}) – the relaxation energy associated with the rest of the system – but it can assume that R^{ea} alone is the dominant factor for the final-state effects.

Then, the "measured" XPS BE level of a specific chemical state ($E_{b(M),PE}$) can thus be interpreted by a semi-quantitative model [144] according to the point-charge potential approximation as:

$$E_{b(M),PE} = E_{b,PE}^{0} + k \cdot q + V - R^{ea} + q \cdot R^{ia} \quad \text{… (C11)}$$

When comparing the BE level of two states of the same element, the chemical shift is thus derived as: $\Delta E_{b(M),PE} = \Delta(V + k \cdot q) - \Delta R^{ea}$ … (C12)

Both initial-state and final-state effects of each chemical state can be graphically presented by means of the Wagner plot (or chemical-state plot) [144,145] in terms of initial-state Auger parameter (β) and final-state Auger parameter (α), which are defined and interpreted, respectively, in equations (C13) and (C14):

$$E_{k,Auger} = \beta - 3 \cdot E_{b,PE} \quad \ldots \text{(C13)}$$

$$E_{k,Auger} = \alpha - E_{b,PE} \quad \ldots \text{(C14)}$$

where $E_{k,Auger}$ is the kinetic energy of the Auger electron.

To extend equation (C13), the initial-state Auger parameter (β) is actually the summation of the kinetic energy of emitted X-ray excited Auger electron and the binding energies of all the electrons involved in the Auger process:

$$\beta = E_{k,Auger} + E_{b,PE} + 2 \cdot E_{b,Auger} \quad \ldots \text{(C15)}$$

Considering the expression for the kinetic energy of an Auger electron:

$$E_{k,Auger} = E_{b,PE} - 2 \cdot E_{b,Auger} \quad \ldots \text{(C16)},$$

the initial-state Auger parameter of a particular state of an element can be rewritten as:

$$\beta = 2 \cdot E_{b,PE} = 2 \cdot (E_b^0 + k \cdot q + V_M) \quad \ldots \text{(C17)}$$

and the change of initial-state effects becomes:

$$\Delta\beta = 2 \cdot \Delta(V + k \cdot q) \quad \ldots \text{(C18)}.$$

The final-state Auger parameter (α) can be defined as:

$$\alpha' = \alpha - h \cdot \nu = E_k - E_{k,PE} \quad \ldots \text{(C19)}$$

in which α′ is the original definition of Auger parameter and h·υ is the energy of the X-ray source. The change of final-state effects, therefore, becomes:

$$\Delta\alpha' = \Delta\alpha = \Delta E_{k,Auger} - \Delta E_{k,PE} \quad \ldots \text{(C20)}$$

where $\Delta E_{k,Auger} = -\Delta\varepsilon + 3 \cdot R^{ea}$, $\Delta E_{k,PE} = -\Delta\varepsilon + R^{ea}$,
and Δε is the change of energy in an electron shell [145]. Then,

$$\Delta\alpha = 2 \cdot \Delta R^{ea} \quad \ldots \text{(C21)}$$

The core-level shift, $\Delta E_{b(M),PE}$ [Equation (3)], with respective to the metal reference depends on both the initial-state and final-state effects and it can thus be deduced easily from equations (C18) and (C21) as:

$$\Delta E_{b(M),PE} = \frac{1}{2}(\Delta\beta - \Delta\alpha) \quad \ldots \text{(C22)}$$

Through these equations, it implies that both physical effects can be roughly estimated via an experimental approach.

X-ray Diffractometry (XRD)

X-ray diffractometer (XRD) is a material characterisation instrument for crystallographic structure and phase identification. A collimated X-ray beam irradiated onto the materials diffracts at different angles according to material crystallographic orientation. The relationship between the wavelength of the X-ray beam, λ, the angle of diffraction, 2θ, the distance between each set of planes of the crystal lattice, d, is given by the Bragg's law (Figure C.4):

$$n \cdot \lambda = 2 \cdot d_{hkl} \cdot \sin\theta_{nhnknl} \quad \ldots \text{(C23)}$$

where n represents the order of diffraction. The significant X-rays penetration depth of the ordinary Bragg Brentano geometry of XRD determined by Beer-Lambert equation between 0.1 – 10 mm (depends on the X-ray irradiation strength and materials density) is too deep for thin layer characterisation. Therefore, the specific geometry of grazing incidence angle (GIXRD) for thin film characterisation was applied, see Figure C.5. In this geometry, the angle of X-ray incidence is fixed at a very low angle at between 0.5 – 3.0º while the detector rotates as in ordinary XRD. Owing to the low angle of incidence, the acquired diffractogram is surface sensitive and the diffracted radiation from the thin film become more significant than the ordinary XRD diffractogram [146,147]. Crystallographic structures and phase identification were carried out for such setup using a Bruker D8 Advance X-ray Diffractometer. The CrKα radiation (λ = 2.2897 Å) at a scan rate of 0.06°/min was employed. An X-ray beam was generated onto the thin film surface at the angle of incidence of 2.0°. Scanning was performed from 40° to 80° at a step size of 0.02°. The diffraction pattern were then analysed with reference to the Powder Diffraction Files (PDF-2) in the International Centre for Diffraction Data (ICDD) for phase identification [148].

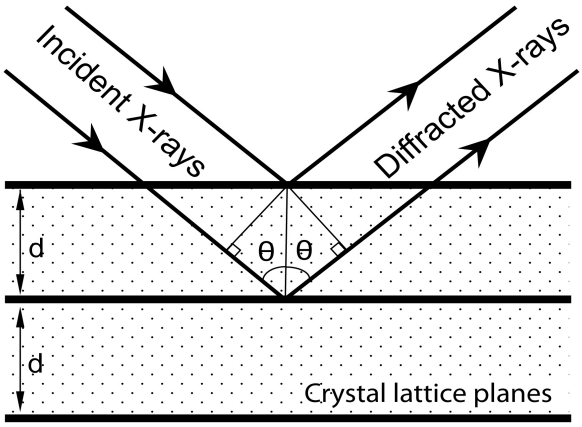

Figure C.4 Illustration of the Bragg's law in an X-ray diffraction process (Author's illustration).

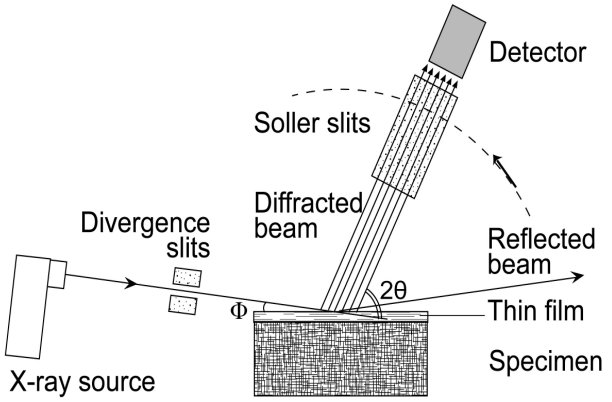

Figure C.5 GIXRD setup in the X-ray diffractometer (Author's illustration).

Crystallite Size Determination

If the characterised structure is crystallised, the size of the crystallite (x) can be calculated through the Scherrer's equation [149]:

$$x = \frac{k \cdot \lambda}{\cos\theta \cdot (FWHM)} \quad \ldots \text{(C24)}$$

where k is a numerical constant, λ is the wavelength of X-ray, θ is the angular position of the characteristic peak and FWHM is the width of the characteristic peak.

Appendix D

Electron Beam Characterisation Instrument: Scanning Electron Microscope (SEM)

Scanning electron microscopy (SEM) is an imaging technique that is commonly used in materials science. It makes use of the electron beam as a medium to form an image. The images produced by this technique can reach high magnification (×100,000 or better) and are found to have much better resolution and larger depth-of-field compared to those captured by the optical microscope. In the current study, the SEM employed was LEO 1550 model (Figure D.1). In the instrument, a Schottky field emission gun equipped with a zirconium oxide-coated tungsten filament is placed at the top of the column. The emitted electrons are accelerated at a uniform direction by the beam booster (or anode) below the gun to form an electron beam. The electron beam follows a vertical path down the column and is guided by the electromagnetic condenser lens without introducing any crossover in between. The beam is finally focused by the objective lens and falls onto the examined sample. The ejected electrons from the sample can be detected either by the in-lens detector inside the objective lens or by the sideway secondary electron (SE) detector. The backscattered electron (BSE) images developed by the high energy electrons can be used to study the elemental distribution on the surface. The SE images, on the other hand, are used for topography examination [150,151]. Images produced by this equipment have a very high resolution as fine as 2 – 5 nm [150]. In the present study, surface morphologies before and after electrochemical measurements of each specimen were examined by means of SE images. The pits formation and surface roughening induced by the electrochemical attack on the potentiodynamically polarised specimens were directly identified.

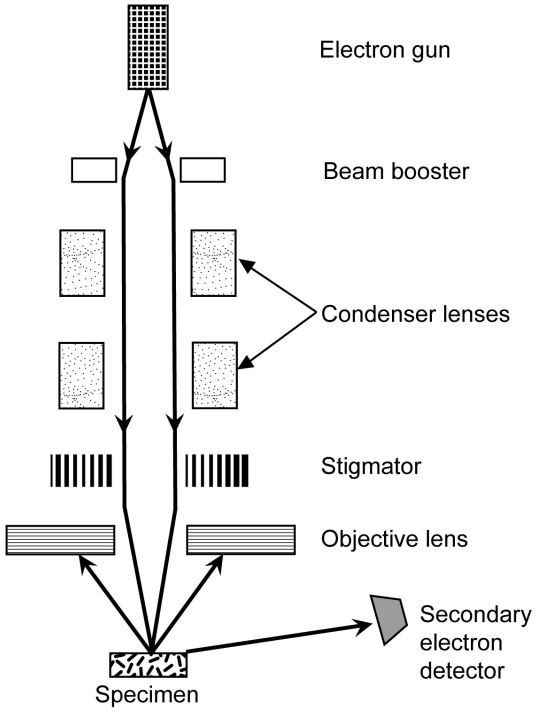

Figure D.1 Cross-section of the LEO 1550 scanning electron microscope column (Author's illustration).

Appendix E

Tribological Testing Instruments: Rockwell Hardness Tester and Sliding Wear Tester

Tribological studies in this research involve Rockwell-C adhesion test and dry sliding wear test in order to investigate the thin film adhesiveness and the wear resistance. In the adhesion test, a standard Rockwell hardness tester modelled Matsuzawa DXT-1 was employed. The indenter was a conical diamond tip, the loading force was set at 150 kg·f and the holding time was about 30 sec. The resulting indentation mark is examined by means of optical microscope. The amount and length of radial crack lines and the delamination and/or buckling features determine the adhesion strength from HF level 1 to 6 according to the VDI 3198 standard [122]. In order to have sufficient coating adhesiveness, the level should be kept as low as possible, see Figure E.1.

The wear resistance of the coated specimen is measured and the wear mechanism is determined by means of dry sliding wear test and SEM examination, respectively. To establish a sliding couple, counter-facing materials have to be chosen and mounted onto a ball holder and the tested specimen is mounted on the stage platform. The sliding counter-face is then moving back and forth against the tested specimen and a wear track is developed (see Figure E.2). After the pre-set of hundreds or thousands of reciprocating sliding cycles, the worn surfaces on both tested specimen and the counter-face will then be dismounted and examined under the optical microscope and SEM [152]. The topography and the volume of the worn region are thereafter measured by means of surface profilometry (read Appendix G) and the wear volume is determined. Thereby, the specific wear rate of individual testing condition can be determined. The wear mechanism can be studied through examining the special worn features remaining on the surface. Some worn features such as scratches, cracks, debris and buckling can be checked up with the aid of SEM. The corresponding chemical composition of each feature can be also analysed by means of energy dispersive X-ray spectroscopy (EDX) [153].

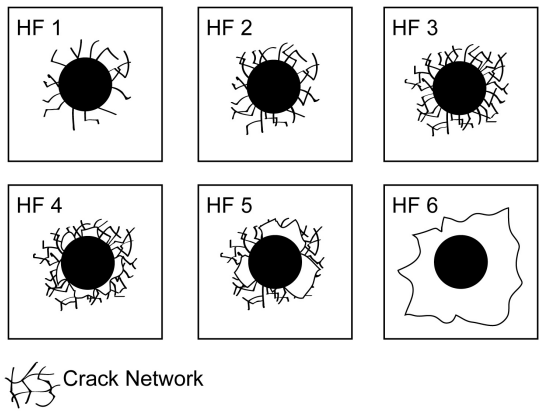

Figure E.1 Classification of the adhesion strength levels in the Rockwell-C adhesion test (Drawing based on [122]).

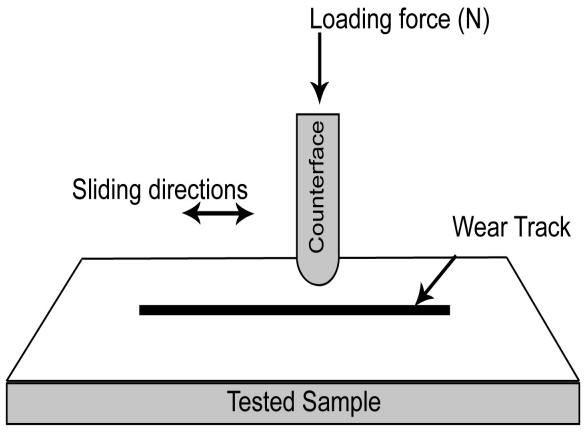

Figure E.2 Sliding wear tester (Author's illustration).

Appendix F

Nanomechanical Testing System: Nanoindenter

Mechanical properties of thin film materials requires highly surface sensitive instrument to determine in order to avoid the substrate contribution. Nanoindentation is one of the most commonly used techniques to depict thin film mechanical properties such as hardness and elastic modulus.

Instrumented indentation testing system of a nanoindenter consists of three basic components: (a) a well-defined geometry indenter, (b) an actuator for applying the force and (c) a sensor for measuring the indenter displacement [127]. For the UBi1® Nanoindenter employed in this work, the instrument is equipped with a three-sided pyramidal shape Berkovich indenter and the three-plate capacitive transducer as shown in Figure F.1. The maximum applied force is up to 30 mN with the resolution of 1 nN and the maximum penetration depth is 20 μm with resolution of 0.04 nm [154].

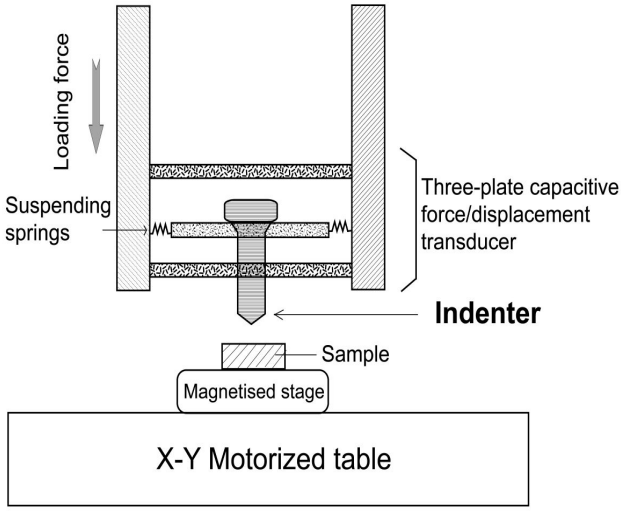

Figure F.1 Schematic drawing showing a nanoindenter (Drawing based on [152]).

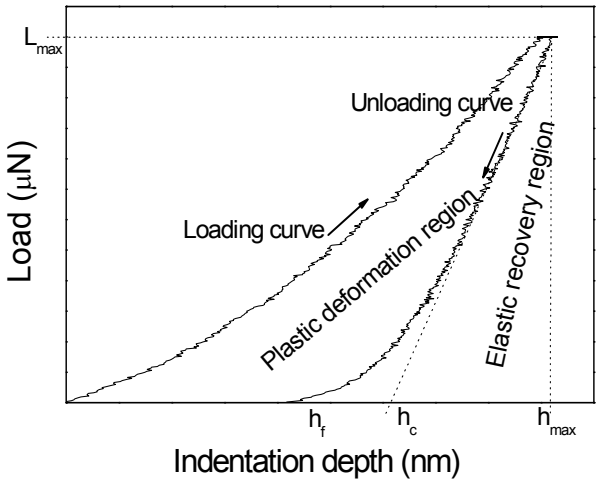

Figure F.2 An illustration of a load-displacement curve (Modified from author's result in Paper 6).

Indentation results of nanoindentation measurement are presented in the form of the load-displacement curve (or loading-unloading curve) as illustrated in Figure F.2. The penetration depth of the indenter increases with the ascending compressive load in micro-Newton scale (μN) applied continuously by the piezoelectric transducer until reaching the maximal load and then the indenter retreats when the load reduces. Three significant depths recorded after the measurements are the maximum penetration depth (h_{max}), the indenter contact depth (h_c) and the depth at which indenter is detached from the tested materials (h_f). The area between loading curve and unloading curve represents the proportion of plastic deformation while the area below the unloading curve represents the proportion of elastic recovery (W_e). Larger proportion of elastic recovery in the tested specimen implies a higher elasticity. In practice, more than 10 indentation measurements should be made on different areas of the sample surface in order to get a better statistics to interpret the characterised materials [155]. In this work, the reported hardness and modulus values are averaged at least from 15 measurements.

Mechanical parameters and properties obtained in nanoindentation test have to be evaluated carefully for the thin film properties since basic indentation evaluation approach is insufficient [124-128]. Traditionally, data obtained in the nanoindenter is primarily characterised by means of Oliver-Pharr method, in which hardness (H) is measured by dividing the maximum loading force (P_{max}) to the contact area (A_c) of the indenter tip, as in equation (F1):

$$H = \frac{P_{\max}}{A_c} \quad \ldots \text{(F1)}$$

where $A_c = const. \cdot h_c^{\,2}$ and *const.* is around 24.5 for Berkovich tip. The reduced modulus (E_r) or indentation modulus (E_{IT}), in fact, is mathematically calculated as a slope of a linear function on 80 % of the unloading curve, and expressed as:

$$E_r = \frac{\sqrt{\pi}}{2\beta} \cdot \frac{S}{\sqrt{A}} \quad \ldots \text{(F2)}$$

where S is the stiffness and β is the indenter dependent constant which is equal to 1.034 for Berkovich.

Furthermore, during an indentation process, two contact bodies are actually involved. They are the indenter (E_i) and the indented materials (tested materials) (E_{sam}). Therefore, the measured indentation, the effective Young's modulus (E*), involve the contribution from both physical bodies and can be interpreted via a reciprocal function as:

$$\frac{1}{E^*} = \frac{1-\nu_i^{\,2}}{E_i} + \frac{1-\nu_{sam}^{\,2}}{E_{sam}} \quad \ldots \text{(F3)}$$

where υ_x is the Possion's ratio of individual materials. For the Berkovich diamond indenter, E_i = 1141 GPa and ν_i = 0.07. Accordingly, E_r for the tested specimen can also be defined physically as:

$$\frac{1}{E_r} = \frac{1-\nu_{sam}^{\,2}}{E_{sam}} = \frac{1}{E^*} - \frac{1-\nu_i^{\,2}}{E_i} \quad \ldots \text{(F4)}$$

The measurement of the coated specimens, E_{sam}, indeed, is a mechanical response from the film-substrate composite. It, therefore, further increases the complexity of the characteristic condition by taking both components into account. So:

$$\frac{1}{E_r} = \frac{1}{E_{sub}} \cdot \phi \cdot \left(\frac{h_c}{t}\right) + \frac{1}{E_{film}} \cdot \left[1 - \phi \cdot \left(\frac{h_c}{t}\right)\right] \quad \ldots \text{(F5)}$$

where $\phi = \frac{2}{\pi} \cdot \arctan\left(\frac{1}{x}\right) + \frac{1}{2\pi \cdot (1-\nu)} \cdot \left[(1-2\cdot\nu) \cdot \frac{1}{x} \cdot \ln(1+x^2) - \frac{x}{1+x^2}\right]$ and $x = \frac{a}{t}$ in which a is the mean radius of grains and t is the thin film thickness [128].

Similar function should be used for film hardness evaluation [125]:

$$H = H_{sub} + \left(H_{film} - H_{sub}\right) \cdot \exp\left[-\left(\frac{\nu_{film}}{\nu_{sub}}\right) \cdot \left(\frac{h_c}{t}\right)^n\right] \quad \ldots \text{(F6)}$$

where the exponent n is either 1 or 2 for a film that is harder or softer than the substrate.

By conducting these series of data analysis, mechanical parameters of uppermost thin coated layer can be determined. More thin film mechanical properties can be further derived and predicted based on these primary parameters. For example, Musil has discussed how to correlate the H^3/E^{*2} to the plastic deformation resistance, H/E to elastic recovery (W_e), and P/S^2 to the tribological properties [129].

Appendix G

Surface Topographical Instruments: Optical Interferometer, Stylus Profilometer, Atomic Force Microscope (AFM)

Surface topographic information such as average roughness (R_a) and three dimensional surface profiles can be obtained by means of non-contact optical interferometry and contact stylus profilometry [156]. In the optical technique, a filtered (PSI mode) or unfiltered (VSI mode) visible light source reflected by a beam splitter illuminates on the sample. The detector at the top of instrument collects a combination of reflected lights from the sample and a 'reference surface' inside the optical instrument forms the interference fringes. Precise measurement can be evaluated through the mathematical calculations based on light intensity on each pixel, 'reference surface' position and applied wavelength of light [157]. In the present study, WYKO RST Plus surface profiling system is employed. This instrument offers two operating modes: phase-shifting interferometry (PSI) and vertical-scanning interferometry (VSI). The PSI mode which allows smooth surface measurements at the angstrom level was used for an overview study about surface condition. The VSI mode which allows rough surfaces and steps measurements at the nanometer level that was used for corroded pits study and thin film thickness evaluation.

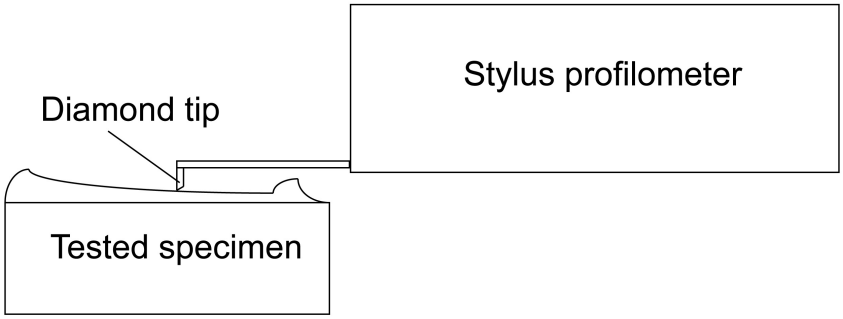

Figure G.1 Stylus profilometer (Author's illustration).

In the contact method, a stylus equipped with a diamond tip of 2.0 μm in radius was equipped in a Taylor-Hobson Form Talysurf-120L profilometer operating in the phase-grating interferometry (PGI) mode for surface mapping (Figure G.1) [158]. Data resolution is about 0.25 μm. Although the data acquisition rate is much slower than the optical technique, this technique takes the advantage of complicated surface profiling on a deep worn surface in which certain part of the surface might be shadowed during the light ray illumination in the above characterisation.

For the fine resolution down to sub-atomic scale, atomic force microscope (AFM) is the choice for surface roughness measurement [159,160]. However, long acquisition time, the demanding testing condition and the nano-scale scanning area are the main disadvantages to apply this measurement as a general practice. AFM mapping was carried out in the Ubi1® Nanoindenter (read Appendix F) after the nanoindentation measurements to check the pile-up and crack initiation (or propagation) phenomena surrounding the indented mark.